CENTRIFUGE MODELLING OF RAILWAY EMBANKMENTS UNDER STATIC AND CYCLIC LOADING

Paul Vorster

A project report submitted in partial fulfilment of the requirements for the degree of

MASTER OF ENGINEERING (GEOTECHNICAL ENGINEERING)

In the

FACULTY OF ENGINEERING

UNIVERSITY OF PRETORIA

July 2016

PROJECT REPORT SUMMARY

CENTRIFUGE MODELLING OF RAILWAY EMBANKMENTS UNDER STATIC AND CYCLIC LOADING

PAUL VORSTER

Supervisors: Professor P.J. Gräbe

Professor S.W. Jacobsz

Department: Civil Engineering

University: University of Pretoria

Degree: Master of Engineering (Geotechnical)

The study comprised the modelling of embankments on a heavy haul coal export railway line between Ermelo and Richards Bay in South Africa. The design of these embankments is usually done with slope stability analysis' method of slices. In the case of railway embankments, a uniformly distributed load is applied over a central ballast width of the embankment to represent the load induced by the train. This however does not take into account the cyclic loading aspect the embankment is subjected to. Physical modelling in a centrifuge is one of the most effective tools available to a geotechnical engineer. Using the typical designed slopes currently used on the coal export line, the failure of these embankments can be modelled in a centrifuge to better understand the mechanism of failure.

The main objective of the study was to investigate the influence of static and cyclic loading on railway embankments by testing models in the geotechnical centrifuge. This was done to determine the failure mechanisms and the difference in settlement between static and cyclic loading. The effect of moisture on the slope stability was also investigated. To achieve these objectives, a suitable loading system was developed that could be used for static and cyclic loading within the centrifuge. Suitable material was sourced that could be used in the centrifuge testing of embankment failures and a procedure was developed to build, compact and instrument a model of an embankment within the centrifuge.

Embankment models representing a standard slope and one material type with varying moisture contents were built and tested in a geotechnical centrifuge. Clayey sand material used for the tests was sampled from one of the sites where a failure occurred on the heavy haul coal export railway line. The loading system simulated the loading created by a heavy haul coal train with a 26 t per axle load along the length of an embankment. A loading block was machined to simulate the load and a pneumatic piston was used to cycle the load on and off the embankment. The results from the centrifuge tests were finally compared to slope stability analyses done with commercial slope stability software.

The results from the tests conducted in the geotechnical centrifuge indicated that cyclic loading significantly increases the magnitude of the vertical settlement which could lead to slope failures. It was observed that the moisture content had a significant effect on the slope stability. A completed slip surface failure was not observed, however significant cracks formed at the crest of the embankment along its length which could induce a failure once water from further precipitation enters those cracks.

The research therefore concluded that cyclic loading on railway embankments has a significant effect on the permanent vertical settlement of the embankment compared to static loading, resulting in the development of cracks and the subsequent increase in moisture content. In the interest of safety and good practise, this should be incorporated into embankment design and slope stability analyses.

DECLARATION

I, the undersigned hereby declare that:

I understand what plagiarism is and I am aware of the University's policy in this regard;

The work contained in this thesis is my own original work;

I did not refer to work of current or previous students, lecture notes, handbooks or any other study material without proper referencing;

Where other people's work has been used this has been properly acknowledged and referenced;

I have not allowed anyone to copy any part of my thesis;

I have not previously in its entirety or in part submitted this thesis at any university for a degree.

_____

Paul Vorster

29221774

July 2016

ACKNOWLEDGEMENTS

This dissertation would not have been possible without the assistance and guidance from several individuals or organisations and I wish to express my appreciation to the following:

a) Firstly, I would like to express my sincere gratitude to my supervisors Prof. PJ Gräbe and SW Jacobsz for the continuous support through this study and related research, for their patience, motivation, and immense knowledge. Their guidance helped me during the research and writing of this dissertation.
b) My brother, Jaco Vorster, for his support and encouragement during times of hardship.
c) My Lord and Saviour for providing me with the strength and wisdom.
d) My family and friends for their support and motivation.
e) The Transnet Freight Rail Chair in Railway Engineering at the University of Pretoria for the financial support.
f) Mr. Jurie van Staden and Henry Jansen for helping to conduct the triaxial tests.
g) Paul Le Roux for conducting the soil water characteristic curve tests.
h) Rudolph du Plooy for his help with the modelling process and for all the motivation and encouragement as a friend during this study.
i) Mr. Rikus Kock for his assistance and operation of the geotechnical centrifuge.
j) My fellow postgraduate students for the stimulating discussions, for the sleepless nights we were working together, and for all the fun we have had during the past two years.
k) The Civil Engineering department at the University of Pretoria for the financial, academic and technical support as well as the use of the laboratory and equipment.

TABLE OF CONTENTS

LIST OF FIGURES

LIST OF TABLES

List of symbols

b	=	Slice width
C_v	=	Coefficient of consolidation (length squared per unit time)
c	=	Cohesive parameter (c = 0 for sand)
c'	=	Effective cohesion
D	=	Length of drainage path
ε_r	=	Resilient strain
g	=	Gravity acceleration (m^2/s)
h	=	Height of the slice measured along the centreline.
N_L	=	Load cycles
N	=	Centrifuge scaling factor
σ'	=	Effective stress (kPa)
$(\sigma - u_a)$	=	Net normal stress
ϕ'	=	Effective angle of internal friction.
ϕ^b	=	Internal friction angle associated with the matric suction that describes the rate of increase in shear strength relative to matric suction.
ψ_m	=	Matric Suction
ψ_o	=	Osmotic Suction
ρ	=	Density (kg/m^3)
q_r	=	Repeated deviator stress or stress pulse
$(\sigma - u_w)$	=	Effective normal stress on the failure plane at failure

σ	=	Total stress (kPa)
S_N	=	Settlement after N load cycles
S_1	=	Settlement from first load cycle
t	=	Time for drainage to occur
τ	=	Shear stress (kPa)
τ_f	=	Shear stress on the failure plane at failure
T	=	Dimensionless time factor
u	=	Pore pressure (kPa)
u_a	=	Air pressure (kPa)
u_w	=	Water Pressure (kPa)
$(u_a - u_w)$	=	Matric suction
χ	=	Effective stress parameter
χ	=	Effective stress parameter

1 INTRODUCTION

This chapter describes the background, purpose and objectives of the study as well as the scope and any limitations. The organisational structure is also described.

1.1 BACKGROUND

The study comprises the modelling of embankments on a heavy haul coal export railway line between Ermelo and Richards Bay in South Africa. As a result of the large demand for coal exports through Richards Bay, the optimisation on the line has resulted in heavy axle loads of 26 t/axle and long trains of 200 wagons per train. The tractive effort available for these long trains is a limiting factor and therefore the grade should be kept to a minimum. In order to do this, large embankments had to be built on the line.

The design of these embankments is usually done with limit equilibrium slope stability analysis' method of slices. The method of slices assumes a circular failure plane. A trial failure plane is divided into vertical planes. The base of the planes is considered straight. The analysis is based on a combined factor of safety (F) defined as the ratio of available shear strength to the shear strength that has to be mobilised to maintain the condition of limit equilibrium. In the case of railway embankments, a uniformly distributed load is applied over a central ballast width of the embankment to represent the load induced by the train.

Physical modelling in a centrifuge is a valuable tool available to a geotechnical engineer. It allows the analysis of complex design problems using geotechnical materials. Small scale models can be accelerated to many times the magnitude of earth's gravity to create a realistic representation of the stresses in the soil. Testing in the centrifuge allows a better understanding of geotechnical events and therefore a better analysis and design can be completed.

Using the typical designed slopes currently used on the coal export line, the failure of some of these embankments can be modelled in a centrifuge to better understand the mechanism of failure.

1.2 OBJECTIVES OF STUDY

The main objective of the study was to investigate the influence of static and cyclic loading on railway embankments by testing models in the geotechnical centrifuge. This was done to determine the failure mechanisms and the difference in the amount of settlement under static and cyclic loading. The effect of moisture on the stability of the slope was also investigated.

1.3 SCOPE OF STUDY

The main focus of the study was to investigate the mechanism of embankment slope failure under static and cyclic loading. Embankment models with one standard slope and one material with varying moisture contents were built and tested in a geotechnical centrifuge. Different test setups and loading methodologies were used and results were recorded (static and cyclic loading). The magnitude of the loading was kept constant. The potential failure mechanisms and settlement were tracked and recorded using PIV (Particle Image Velocimetry) analysis and the settlement was measured with Linear Variable Differential Transformers (LVDTs).

The results from the centrifuge tests were compared to a slope stability analyses done using commercial software. Settlement readings were taken throughout the centrifuge tests in order to compare different loading methodologies and the effect of moisture content on the models. Tests were conducted on the material used for the centrifuge tests and results used in conducting the analyses.

1.4 METHODOLOGY

The objectives of the study were achieved by following the methodology described below:

- A literature study provided information regarding embankment failure mechanisms, slope stability analyses and linking it to railway engineering, material characteristics with the effect of moisture thereon and geotechnical centrifuge modelling. Background information was used to gain understanding of certain terms and situations.
- A loading mechanism was created to replicate the loading induced by a heavy hail train on an embankment. The loading system could be used for static and dynamic loading within the centrifuge.

- A procedure to build, compact and instrument a model of an embankment within the geotechnical centrifuge was developed.
- Embankment models were tested in the geotechnical centrifuge using the loading mechanism created to replicate static and cyclic loading at different moisture contents in the soil. The settlement of the models were measured using LVDTs and the results were compared between loading methodology and moisture contents. PIV analysis was done to track the movement of the soil mass.
- Triaxial tests were conducted on the material used in the centrifuge tests in order to obtain the strength parameters in order to conduct the slope stability analysis.
- The soil water characteristic curve was obtained to evaluate the likely pore water suctions in the embankment material to evaluate the contribution of matric suctions to the strength of the embankment.
- A slope stability analysis was done in GeoStudio to compare the different factor of safety values using the material characteristics obtained from the triaxial tests and the soil water characteristic curve.
- Finally, comparing the different results from the centrifuge models and the slope stability analyses.

1.5 ORGANISATION OF REPORT

The report consists of the following chapters and appendices:

- Chapter 1 serves as introduction of the report; it outlines the objectives, scope and methodology of the study.
- Chapter 2 consists of a literature study on the topic of this report; it gives background information and a better understanding on this topic.
- Chapter 3 explains the experimental setups and preparations of the setups. The procedure followed during all the tests is also discussed in this chapter.
- Chapter 4 contains the data recorded, analysis and a discussion of the data.
- Chapter 5 consists of the conclusions and recommendations of the study.
- The list of references follows at the end of the report.
- Appendix A contains the results and discussion of the preliminary tests (A1-A4).

2 LITERATURE STUDY

There is an ever increasing need to fully understand the failure mechanisms of railway embankments. The failure of a railway embankment can result in large financial losses if the line has to be closed down for remedial measures, rehabilitation or if a derailment occurs. The literature study will cover the following sections applicable to the study:

- The different failure mechanisms of railway embankments that are relevant to this study.
- The different methods of slope stability analysis and the criteria used for the design of railway embankments.
- Soil characteristics such as effective stress, shear strength and soil suction.
- The effect of moisture content on the stability of the embankment.
- Repeated loading and the effect thereof on the subgrade of a railway line.
- Modelling in a geotechnical centrifuge and the relevant scaling laws.
- Railway loading application in a geotechnical centrifuge.

2.1 EMBANKMENT FAILURE MECHANISMS

There are numerous ways in which a railway embankment can fail. The mechanisms that will be discussed are embankment foundation failure also known as massive shear failure, wedge failure and embankment slope failure.

Massive shear failure occurs as a result of unbalanced forces in the substructure of the railway line. The main forces that contribute to this failure mechanism are the weight of the train and the superstructure. These forces are resisted by the substructure layer shear strength. The failure zone moves through the subgrade and therefore the subgrade properties play a large role in resisting the failure (Selig and Waters, 1994). The massive shear failure mechanism and embankment foundation failure can be seen in Figure 2.1 and Figure 2.2 respectively.

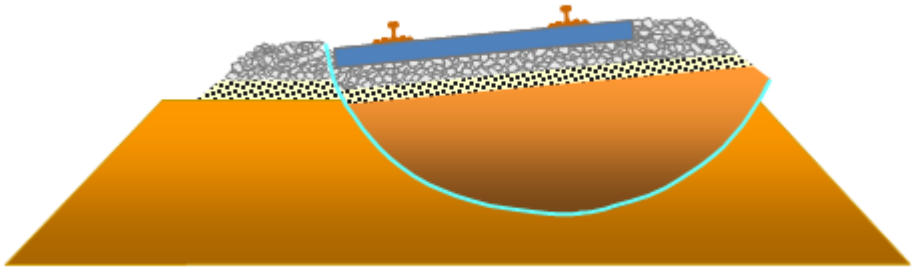

Figure 2.1: Massive shear failure (Selig, 2013)

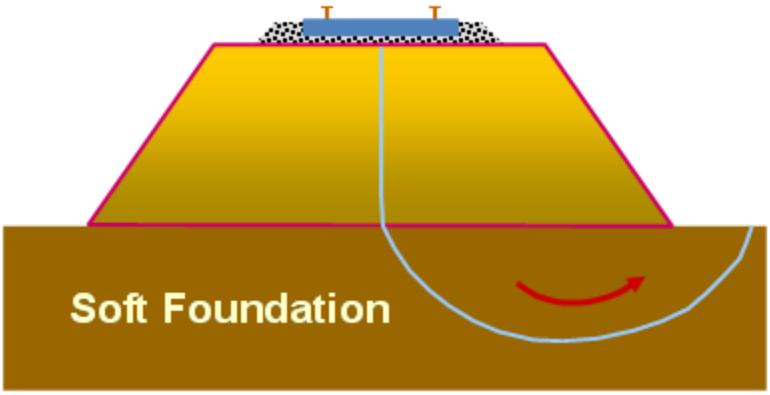

Figure 2.2: Embankment foundation failure (Selig, 2013)

The wedge failure mechanism occurs when a shear occurs between the embankment base and subgrade. There is very low strength in tension in the embankment soil and therefore it can easily separate and slide down the soil foundation surface. A simple illustration of this failure mechanism can be seen in Figure 2.3 (Selig, 2013).

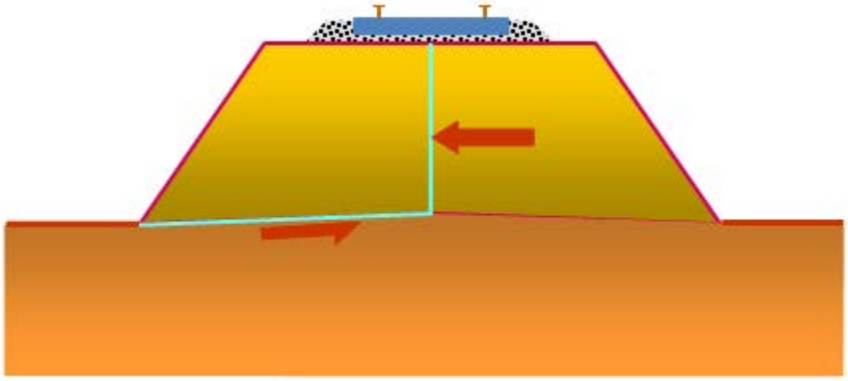

Figure 2.3: Wedge failure mechanism (Selig, 2013)

Embankment slope failure is as the name describes failure of the embankment slope through slip surfaces that are developed within the slope of the embankment. Shallow slip surface or deep seated failures which are the same as massive shear failure mechanisms can be encountered. An illustration of different slip surfaces can be seen in Figure 2.4.

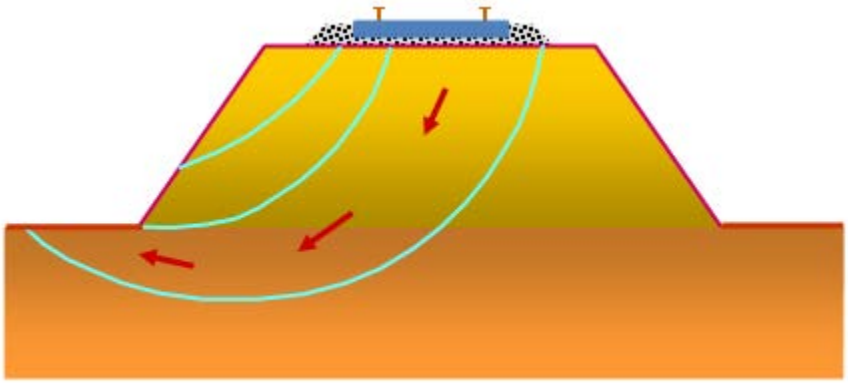

Figure 2.4: Embankment slope failure (Selig, 2013)

Shallow slip surfaces are predominantly associated with the top 1.0-1.5 m layer of soil that experiences major seasonal changes in pore pressure. The seasonal shrink-swell cycle of the soil can cause movement downslope as a result of non-recoverable strain and cracking which could finally result in shallow failures

(Vaughan, 1994). The failure can be attributed to the advance of the wetting front and the reduction of the shear strength of the soil as a result of the decrease in matrix suction in the unsaturated soil (Fredlund and Rahardjo, 1993; Rahardjo et al. 1995).

Rainfall can have a significant effect on the matric suctions in the soil, which are negative pore water pressures found in the soil. Two failure mechanisms are associated with rainfall induced slope failures. The first mechanism results in liquefaction of the soil mass after significant build-up of positive pore water pressures (Collins and Znidarcic, 2004, Wang and Sassa, 2001). The second failure mechanism is due to rainfall infiltration into unsaturated soil and results in the loss in shear strength when soil suctions are decreased or dissipated (Fourie et al., 1999; Fredlund and Rahardjo, 1993). Cracks in the slope decrease the slope's shear strength and increase the hydraulic conductivity of the soil. Once rainfall enters the cracks, the water creates additional driving forces responsible for the development of a slip surface and subsequent failure (Zhang et al., 2010).

2.2 SLOPE FAILURE INVESTIGATIONS

Numerous cases of slope failures were reported by Transnet in 2007 on the Ermelo – Richards Bay line during a season of exceptionally high rainfall. Shallow slip surface failures as well as deep seated failures occurred. One of the concerns was whether the embankments were stable enough after shallow slip surface failures had occurred for the railway line to stay operational. Photos of these failures can be seen in Figure 2.5 and Figure 2.6. These were massive failures that required large scale rehabilitation. The other major concern was determining the cause of these failures and incorporating a solution into the embankment design to prevent such failures in the future.

Figure 2.5: Embankment slope failure on the Ermelo-Richards bay line (Transnet Report, 2007)

Figure 2.6: Embankment slope failure on the Ermelo-Richards bay line (Transnet Report, 2007)

The reports indicate that for some of the failures investigated, a black ash type of material was found in the upper material layer. Material samples were taken at the most severe slope failure to do grading analysis and shear box tests. It was found that the one material sample (Sample 1) could be classified as a silty-sand and the other three samples (Sample 2 to 4) were classified as clayey sands. The grading curves are shown in Figure 2.7. The properties of the material samples can be seen in Table 2.2. The sub layers were reported to be very moist and distinct differences in colour between the layers could be seen. The optimum moisture content was done on a separate sample and was found to be 12.1 % with a maximum dry density of 1928 kg/m^3.

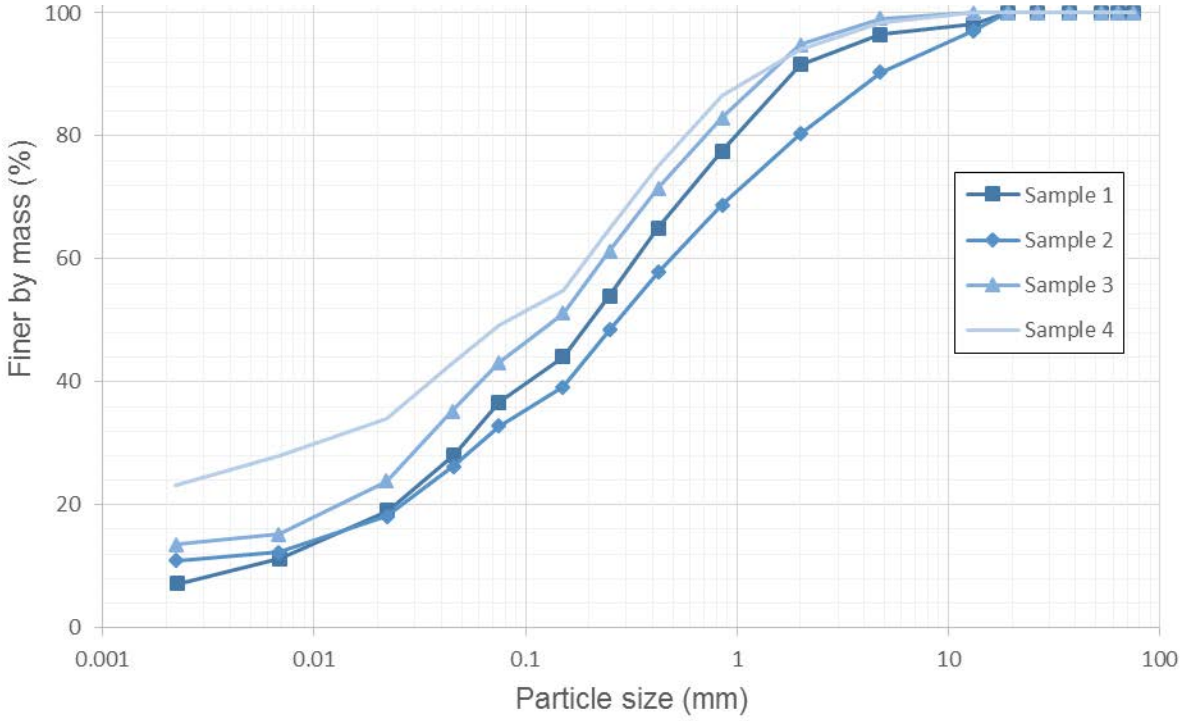

Figure 2.7: Particle size distribution of material sample at slope failure site

Table 2.1: Sample properties of material at slope failure site

	Sample 1	Sample 2	Sample 3	Sample 4
Gravel	8%	20	5	6
Sand	59%	50	55	48
Silt	26%	19	26	24
Clay	7%	11	13	23
Liquid Limit	37	35	43	33
Plasticity Index	13	12	17	11
Linear Shrink.	3.5	3.5	3.5	3.5
Overall P.I.	8	7	12	9
Unified classification	SM	SC	SC	SC

2.3 SLOPE STABILITY ANALYSIS

To determine the stability of a railway embankment it is necessary to do slope stability analysis. The method of slices is discussed in this chapter with the advantages and disadvantages covered at the end of

this section. The method of slices assumes that the failure plane is circular. A trial failure surface is divided into vertical planes. The base of the planes is considered to be straight. The analysis is based on a combined factor of safety F defined as the ratio of available shear strength to the shear strength that has to be mobilised to maintain the condition of limit equilibrium. Figure 2.8 shows the principle behind methods of slices.

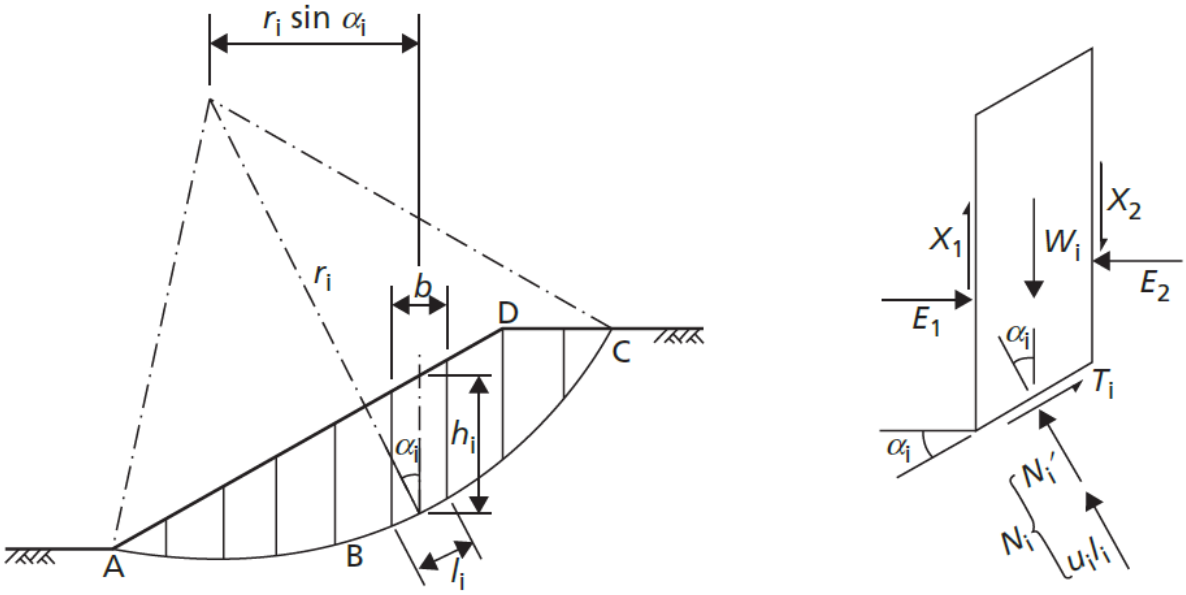

Figure 2.8: Method of slices (Craig , 2004)

The factor of safety is assumed to be the same for each slice, therefore there has to be mutual support between the slices which can therefore be seen as inter-slice forces. All external forces have to be accounted for in the analysis. Using the notation from Figure 2.8, the forces that act on the slice with their relevant formulas are as follows (Craig, 2004):

1. The weight of the slice W.

$$W = \rho b h \qquad \textbf{Eq. 2.1}$$

Where:

ρ = the soil density

b = slice width

h = height of the slice measured along the centreline.

2. The normal force that acts on the base of the slice, N, has two components namely the effective normal force N' and the boundary force U due to the pore pressure.

$$N = \sigma l \qquad \textbf{Eq. 2.2}$$

$$N' = \sigma' l \qquad \textbf{Eq. 2.3}$$

$$U = ul \qquad \textbf{Eq. 2.4}$$

Where:

σ = Stress

σ' = Effective stress

l = length of the slice base

u = Pore pressure at the centre of the base.

3. The shear force T acting on the slice base.

$$T = \tau_m l \qquad \textbf{Eq. 2.5}$$

Where:

τ_m = Shear strength

4. The normal forces acting on the sides of the slice, E_1 and E_2.
5. The shear forces acting on the sides of the slice, X_1 and X_2.

The five main methods of slices are:

- Fellenius (Swedish) Method
- Bishop Simplified Method
- Janbu Simplified Method
- Spencer Method

- Morgenstern-Price Method

These methods differ mostly in terms of the assumptions made with regard to the inter-slice forces and the equilibrium equations used to solve the problem. The advantages and disadvantages of methods of slices are given below.

The main advantages include:

- Yields a single factor of safety
- Suitable for complex problems
- Relatively low calculation effort involved
- Methods well calibrated against field models

The main disadvantages include:

- The same factor of safety is assumed for all slices, i.e. a rigid failure block is assumed.
- Assumptions have to be made regarding the failure shape.
- Non-rigorous methods are not suitable for application of external forces.
- The amount of calculations required increase as the model becomes more advanced.
- Progressive failure cannot be simulated.
- The result is sensitive to inter-slice forces and the equilibrium equations used.
- Strains and displacement compatibilities are not considered.
- The calculated normal stresses on the failure plane are not necessarily realistic.

The main disadvantage for the various slope stability analysis methods in terms of railway engineering is that it is restricted to static loading and therefore cyclic loading is not taken into account. The effects of cyclic loading play a large role in geotechnical engineering and railway engineering. This is discussed in further detail in Section 2.7.2.

2.4 EFFECT OF MOISTURE CONTENT ON SOIL

The structure of a soil is largely controlled by the size, shape and roughness of the particles and the stress effects regarding the particle interlocking. The soil structure or microstructure of fine grained soils is more complex and is influenced by the amount and type of clay in the soil. The clay minerals comprise of plate like particles, which have a net negative surface tension that is neutralised by the adsorption of

positively charged ions (cations) and polarised water molecules. The amount by which this happens is largely based on the clay mineralogy, surface area and the cation-exchange capability. This charge between the cation and water molecules is the attractive force behind cohesion which is significantly affected by the moisture content in the soil. This effect therefore has a large influence on clay based embankments (Gunn et al., 2009)

The Atterberg limits were introduced to describe the moisture content affected plasticity and strength of fine grained soils. A fine grained soil with a moisture content at the Liquid Limit will have a shear strength of 1 kPa and will have the behaviour of a liquid. The Plastic limit is described by the moisture content at which the soil has a shear strength of 100 kPa and will behave like a plastically deformable solid (Gunn et al., 2009). The effect moisture content has on the strength and consistency of fine grained soils is shown in Figure 2.9.

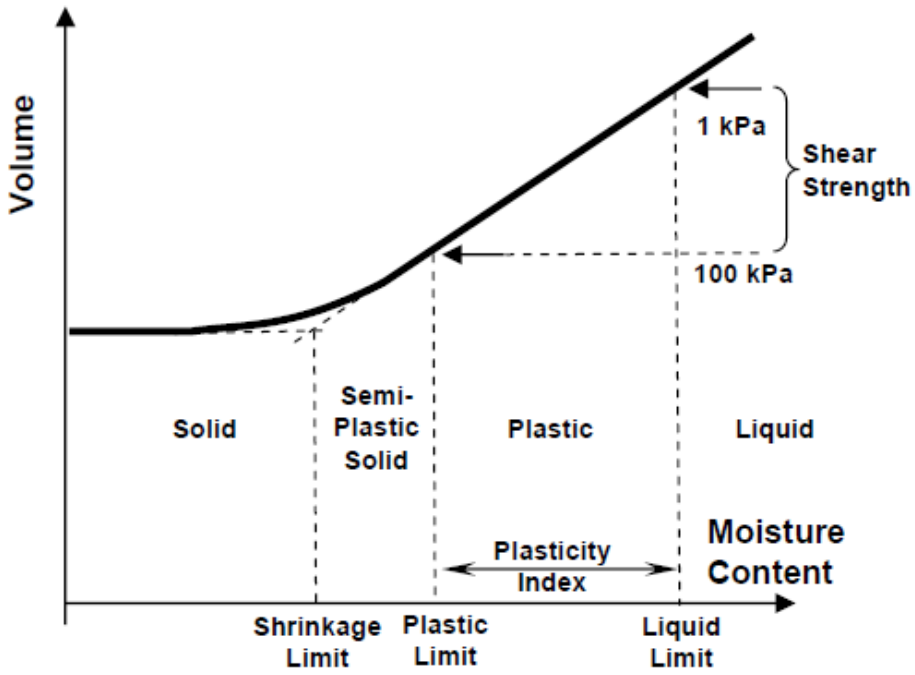

Figure 2.9: The Moisture content effect on the strength and consistency of fine grained soils (Gunn et al., 2009)

With regard to embankments, as the height of the earthworks increases, the soil particles are forced together. With well drained conditions the pore voids will decrease as the material consolidates and the fluid in the voids is expelled. An estimate can be given of the shear strength of the soil by the angle of friction between the soil grains when comparing the shear stresses with the normal stresses. With poor drainage less consolidation will take place. The fluid in the voids will be compressed and thus increasing the pore pressure and reducing the angle of friction. Granular soils do not have any significant cohesion between particles and a change in moisture content will have little effect on the grain friction and thus on the residual strength. A granular soil with no confining stress has little or no unconfined strength and the individual soil particles can be removed from one another as they have no cohesive strength. On the other hand, with no confining stresses on a fine grained soil, it still has cohesive strength which is effected by grain mineralogy and moisture content (Gunn et al., 2009).

2.5 UNSATURATED SOIL MECHANICS

The mechanical stability at any point in the soil depends on the strength parameters of the soil and the stress state at that point. When the soil is saturated the stress state can be described by the total stress and the pore pressure using the concept of effective stress. The effective stress state is the governing factor determining whether a soil is in a state of stability or failure. The soil strength generally depends on the soil mineralogy, particle morphology and inter-particle arrangement. These are the controlling factors which affect the empirical material parameters such as cohesion and the internal friction angle. The work from Lu and Likos (2004) and Fredlund and Rahardjo (1993) is the core material used to describe these parameters.

The total stress found in a soil mass can be considered as an external stress and could either be due to a surcharge load or the self-weight of the soil. The pore pressure in saturated soils is usually compressive and isotropic, whereas the pore pressure in unsaturated soils is generally tensile. The contribution that pore pressure has to the total stress in an unsaturated state depends on the degree of saturation and the pore size distribution (Lu and Likos, 2004).

Lu and Likos (2004) states that unsaturated soils found in the field is characterised by the position of the water table below ground. The soil above the water table can be divided into three regimes:

1. Capillary fringe where the soil remains saturated under negative pore water pressure.

2. Funicular regime where the soil is at an unsaturated state characterised by a continuous water phase.
3. Residual or pendular regime which is characterised by an isolated, discontinuous water phase.

The transitions between the three regimes are mainly controlled by the pore size and pore size distribution of the soil. Figure 2.10 illustrates the degree of saturation profile found in the soil. The point where desaturation starts in the soil located above the water table is referred to as the air-entry point and the hydraulic head associated with this point is called the air-entry head.

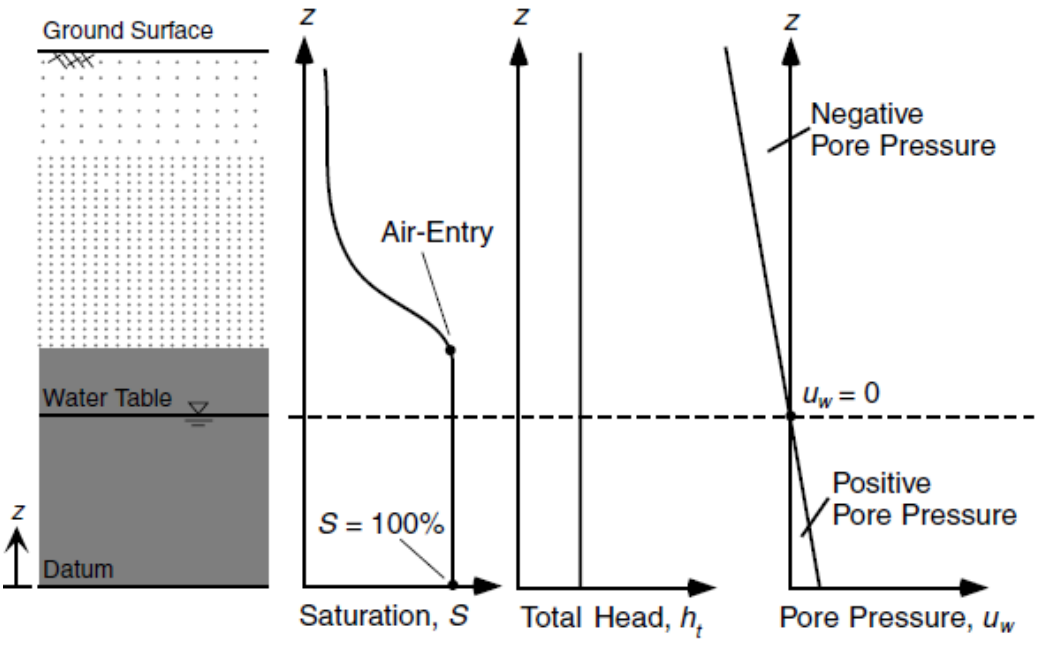

Figure 2.10: Saturation, head and pore pressure profiles (Lu and Likos, 2004)

Unsaturated residual soils tend to experience high matric suction during dry periods which result in an increase in shear strength of the residual soil (Rahardjo et al., 2005). Extended wet periods result in sufficient infiltration into the slope which in turn decreases the matric suction in the soil and therefore the additional shear strength provided by the suction is reduced and a shallow landslide can be triggered (Fredlund and Rahardjo, 1993; Rahardjo et al. 1995).

2.5.1 Effective Stress

Bishop (1959) proposed the meaning of effective stress with regard to unsaturated soils to take two factors in to account: firstly the stress acting through the air phase, i.e. the pore air pressure, u_a. Secondly the difference between the pore air pressure and the pore water pressure, u_w, with the following stress equation (Lu and Likos, 2004):

$$\sigma' = (\sigma - u_a) + \chi(u_a - u_w) \qquad \textbf{Eq. 2.6}$$

Where:

$(\sigma - u_a)$ = Net normal stress

$(u_a - u_w)$ = Matric suction

χ = Effective stress parameter

The effective stress parameter is a material variable that usually varies between zero and unity. With $\chi = 0$ representing a completely dry soil and $\chi = 1$ representing a fully saturated soil and therefore reducing the above equation to Terzaghi's normal effective stress equation describing a fully saturated soil (Lu and Likos, 2004).

Lu, Godt and Wu (2010) proposed that the suction stress characteristic curve represents the effective stress for shear strength behaviour of unsaturated soil. This concept differs from Bishop's effective stress concept largely that it eliminates the need to define the coefficient of effective stress χ , because suction stress is solely a function of soil suction. Lu et al. (2010) describes the working hypothesis where the change in energy of soil from its free water state to be mostly consumed in the suction stress and that experiments conducted show there is a relationship between the soil water characteristic curve (SWCC) and the suction stress characteristic curve (SSCC). The SWCC plots suction against saturation and the SSCC plots tensile stress against saturation. They proposed the closed form equation for effective stress in the entire pore water pressure range as:

$$\sigma' = \sigma - u_a + (u_a - u_w) \qquad (u_a - u_w) \leq 0 \qquad \textbf{Eq. 2.7}$$

$$\sigma' = \sigma - u_a + \frac{(u_a - u_w)}{(1+[\alpha(u_a - u_w)]^n)^{(n-1)/n}} \qquad (u_a - u_w) \geq 0 \qquad \textbf{Eq. 2.8}$$

Where n and α are empirical fitting parameters of unsaturated soil properties:

$n =$ Pore size distribution parameter

$\alpha =$ Inverse of the air entry pressure for saturated soil

2.5.2 Shear Strength

The shear strength of a soil is of great importance when the stability of the soil mass under a load is in question. Slope stability analysis is required for numerous engineering problems where the shear strength of the soil has to be considered. For saturated or unsaturated conditions the shear strength of the soil may be defined as the maximum internal resistance per unit area the soil is capable of sustaining along a failure plane. The shear strength for saturated soil is described by the Mohr-Coulomb failure criterion. This represents the shear strength in terms of the material variables ϕ' and c' as well as the effective stress state variable shown below (Terzaghi, 1943):

$$\tau_f = c' + (\sigma - u_w)\tan\phi' \qquad \textbf{Eq. 2.9}$$

Where:

τ_f = shear stress on the failure plane at failure

c' = effective cohesion

$(\sigma - u_w)$ = effective normal stress on the failure plane at failure

ϕ' = effective angle of internal friction.

Two general trends can be seen for the shear strength of unsaturated soils. Firstly, the shear strength for unsaturated soil generally increases as the net normal stress increases as seen in saturated soil. Secondly there is the trend that comes forth from triaxial and shear test results. The shear strength increases as applied matric suction increases. Fredlund et al. (1978) takes into account another variable ϕ^b that allows the increase in shear strength with the increase in matric suction. An extended Mohr-Coulomb criterion was developed to describe the shear strength of unsaturated soil which can be seen in Figure 2.11. A planar surface describes the failure envelope and can be represented by (Lu and Likos, 2004):

$$\tau_f = c' + (\sigma - u_a)\tan\phi' + (u_a - u_w)\tan\phi^b \qquad \textbf{Eq. 2.10}$$

Where:

$(\sigma - u_a)$ = Net normal stress on the failure plane at failure

ϕ' = Angle of internal friction associated with the net normal stress

$(u_a - u_w)$ = Matric suction at failure

ϕ^b = Internal friction angle associated with the matric suction that describes the rate of increase in shear strength relative to matric suction.

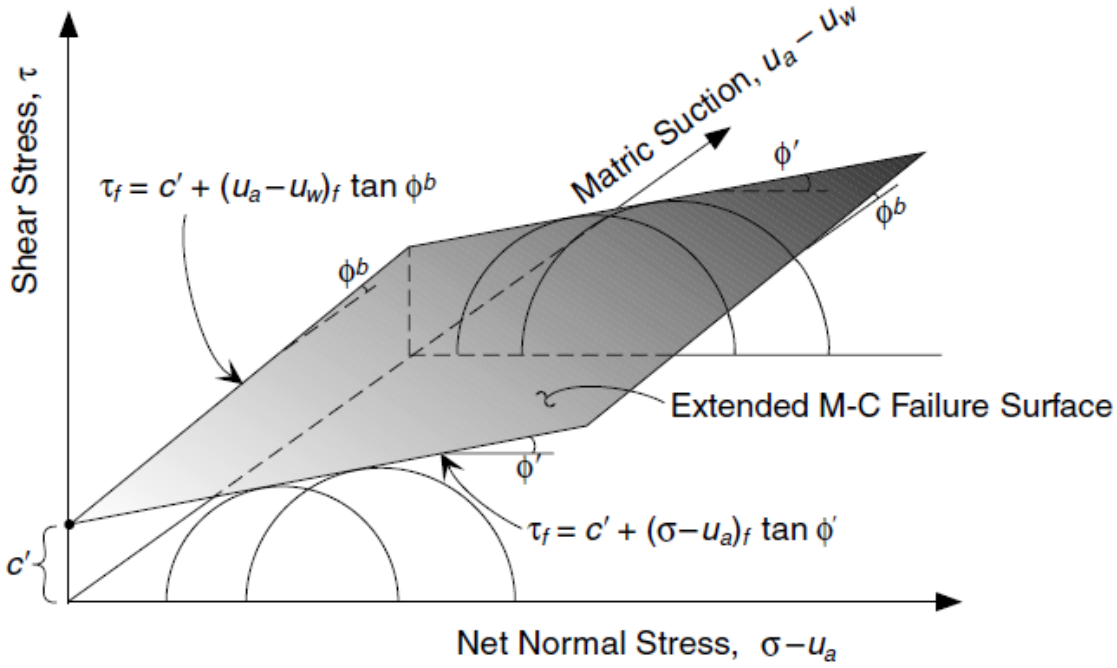

Figure 2.11: Extended Mohr-Coulomb failure criterion for unsaturated soils (Lu and Likos, 2004)

2.5.3 Soil Suction

The total suction in the soil quantifies the thermodynamic potential of the soil pore water relative to a reference potential of free water. Free water is the water containing no dissolved solutes and has no interactions with other phases that could impact the curvature of the air-water interface as well as no external forces acting on it other than gravity. The primary mechanisms, other than temperature, gravity and inertial effects, which affect and decrease the potential of the soil pore water include (Lu and Likos, 2004):

- Capillary effects
- Short range adsorption (particle-pore water interaction)
- Osmotic effects

The suction from capillary effects and short range adsorption is grouped under the general term *matric* suction and the suction as a result from dissolved solids is referred to as *osmotic* suction. The total suction is considered as the sum of matric suction and osmotic suction and can be written as:

$$\psi_t = \psi_m + \psi_o \qquad \textbf{Eq. 2.11}$$

Where:

ψ_m = Matric Suction

ψ_o = Osmotic Suction

The physical and physicochemical mechanisms responsible for the suction in the soil depend on the water content of the unsaturated soil-water-air system. At low water content levels with high values of suction the dominant mechanism contributing to the suction in the soil is the relatively short range adsorption effects governed by the surface properties of the soil solids. At high water levels with low values of suction in the soil the main pore water retention mechanism is capillarity which is governed by the particle pore structure and pore size distribution. The Osmotic suction is present throughout the entire range of water contents and remains constant unless the concentration of dissolved solutes changes (Lu and Likos, 2004).

The transition between the high and low suction regimes and different mechanisms is highly dependent on the soil type. For fine grained materials such as clays a large amount of pore water is required to fulfil the large surface hydration energies associated with the high suction regime. With sands there is a small amount of water adsorbed during the initial surface hydration mechanisms and the capillary effect governs over the majority of the unsaturated water content range. The constitutive relationship between the soil suction and the soil-water content is described by the SWCC.

The shape of the SWCC is influenced by the dominating material properties such as the pore size distribution, grain size distribution, density, organic material content, clay content and mineralogy which affect the pore water retention behaviour. The behaviour of the SWCC is the key to understanding the relationship between the physical properties that describe the critical component of unsaturated soil mechanics. Figure 2.12 shows a description of the general behaviour of a SWCC. It can be simplified to three straight line segments on a semilog plot of suction versus moisture content that ranges from zero to fully saturated.

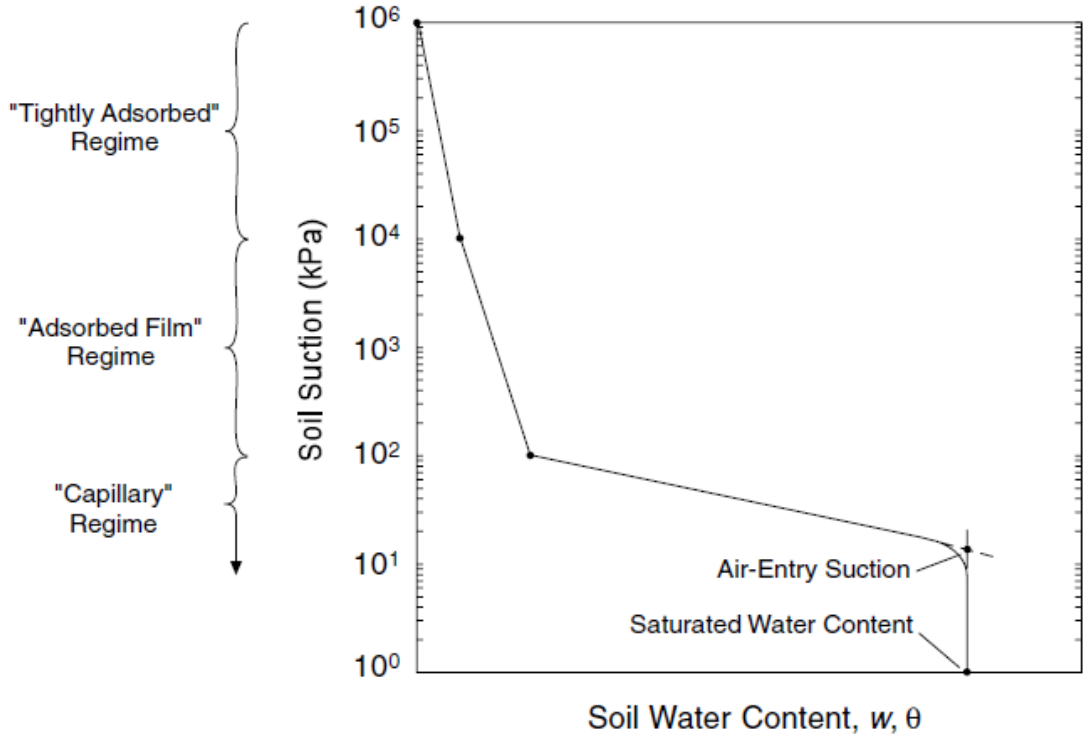

Figure 2.12: McQueen and Miller's (1974) conceptual model for a SWCC

Three typical SWCCs for sand, silt and clay are shown in Figure 2.13. A sandy soil shows the surface adsorption regime in the high suction range to be very limited because the specific surface and surface charge properties are relatively small. The dominant suction mechanism is capillarity over the majority of the unsaturated water content range and then terminating at a relatively low air-entry pressure which is controlled by the relatively large pore sizes between the sand particles. The overall slope of the SWCC in the capillary regime is controlled by the pore size distribution of the material. A soil with a relatively narrow pore size distribution usually has a relatively flat slope in the capillary regime because the bulk of the pores are drained over a relatively narrow range of suction. Silty soil generally adsorbs a much larger amount of water than sand under the short-range adsorption mechanism due to the larger specific surface area of silt compared to sand. The air-entry point of silt is found at a larger point compared to sand due to the relatively small pores. Clay has the greatest capacity to adsorb water under short-range surface interaction as a result of the large specific surface area of clay particles and because of charged surfaces. The SWCC is more meaningful for expansive clays in terms of gravimetric water content as a result of volume change during the moisture absorption process (Lu and Likos, 2004).

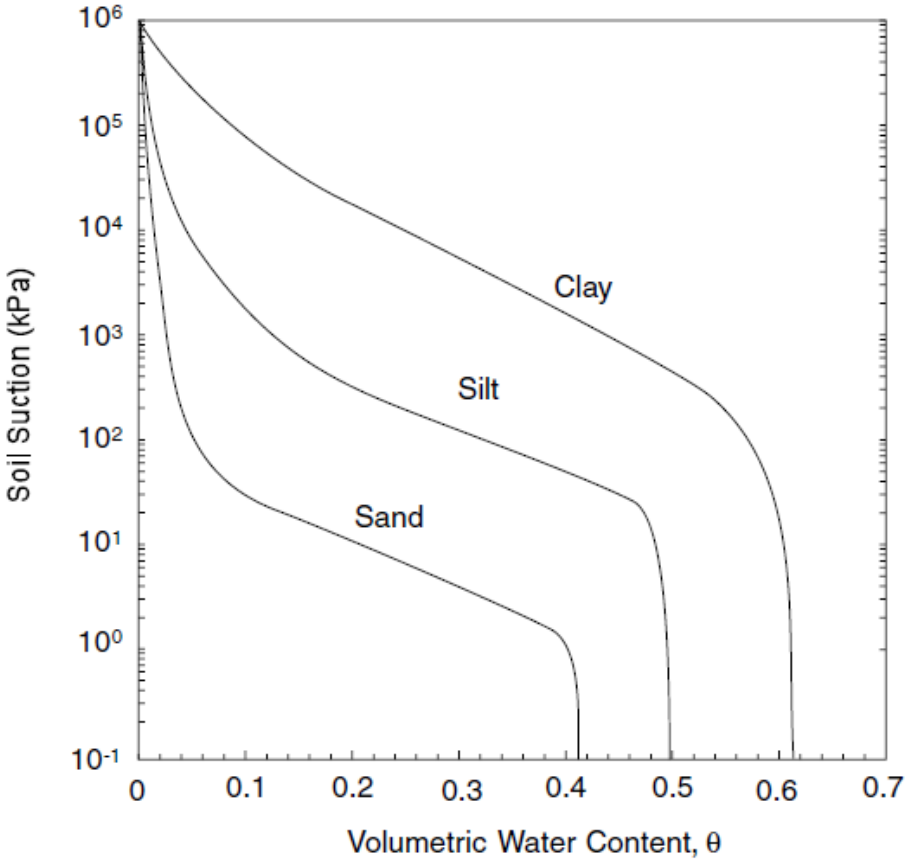

Figure 2.13: Typical SWCCs for sand silt and clay (Lu and Likos, 2004)

The estimation procedures used to characterise unsaturated soil property functions are based on the assumptions that the soil undergoes no volume change as the suction in the soil increases. The assumption is valid for sands and coarse grained materials but cannot be used for fine grained silts and clays. There are two primary reference points on the SWCC, these are the air-entry value and the residual conditions. The slope changes in the SWCC can assist in identifying the air-entry value of the soil. The change in slope is however dependent on how the amount of water in the soil is quantified. In order to interpret the behaviour of unsaturated soils that undergo large volume change, shrinkage curve measurements are needed in conjunction with the SWCC (Fredlund, 1964, Fredlund et al., 2011).

The shrinkage curve shows the behaviour of the soil from an initial high water content to completely dry conditions with regard to its void ratio. Figure 2.14 shows a typical shrinkage curve with its relationship to Atterberg limit classifications. The point where the soil starts to desaturate is close to the plastic limit of the soil. This shows there is a correlation between the air-entry value and the plastic limit of the soil.

As the material dries further it reaches a point where no further volume change occurs. This can be referred to as the true shrinkage limit of the soil and the gravimetric water content appears to approximately correlate with the residual soil conditions. The shrinkage limit is defined as the water content value corresponding to the minimum volume that the soil can attain upon drying to zero water content (Fredlund et al., 2011).

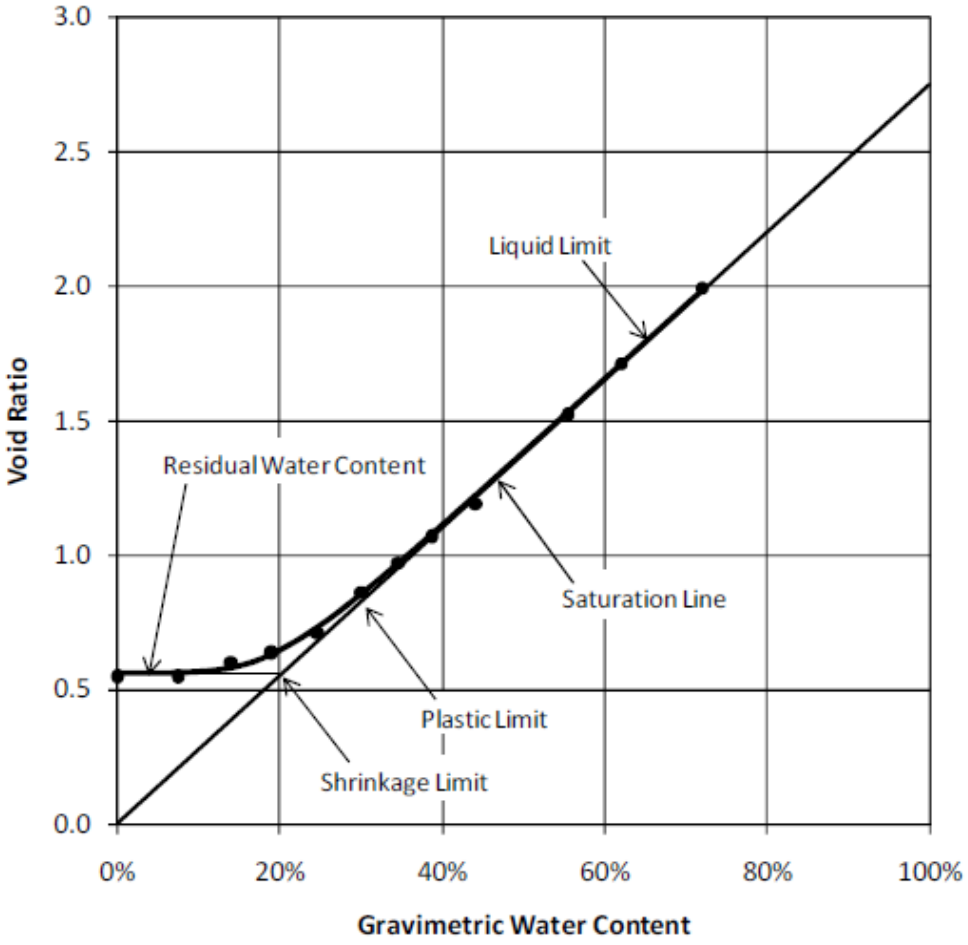

Figure 2.14: Example of a shrinkage curve with reference to the Atterberg Limit classification (Fredlund et al., 2011)

2.6 SLOPE STABILITY ANALYSIS IN RAILWAY EMBANKMENTS

A general solution to slope stability problems is calculated by two-dimensional limit equilibrium methods that incorporate the methods of slices to determine a factor of safety against slope instability. The geometry variables that are considered and are shown in Figure 2.15 are (Selig and Waters 1994):

- Side slope, n, of the subgrade
- Distance, W, of the starting point of the slope from the centre of the loaded area.

The analysis of the two-dimensional embankment representation is simplified by assuming the loaded distance along the track is much greater than the length of the sleepers. This assumption is conservative because end effects such as shearing resistance are neglected which will increase the bearing capacity (Selig and Waters 1994).

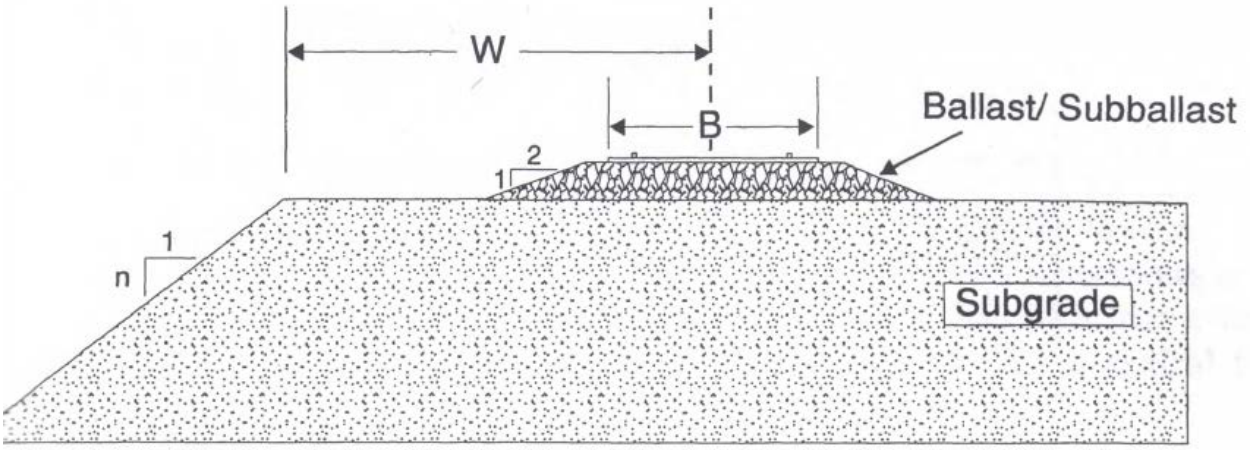

Figure 2.15: Slope stability geometry parameters (Selig and Waters, 1994)

2.6.1 Drained and Undrained Conditions

Embankment failure can occur under drained or undrained conditions. If an embankment consist of a soil with low permeability characteristics and instability is created by either a change in loading at the top of the embankment or the removal of soil at the bottom of the embankment, the material may not have

enough time to drain during the time which the loads are changed. This may cause unequalised pore pressure that could lead to slope failures. In this case it can be assumed that the material is undrained. Materials with high values of permeability have enough time to dissipate excess pore water pressure in cases where load changes occur (Turner and Schuster, 1996).

An important aspect to slope stability analyses is that of the drainage conditions for the different soils in the slope. The method to determine this is by calculating the value for the dimensionless time factor T (Turner and Schuster, 1996):

$$T = \frac{C_v t}{D^2} \qquad \textbf{Eq. 2.12}$$

Where:

T = dimensionless time factor

C_v = coefficient of consolidation (length squared per unit time)

t = time for drainage to occur

D = length of drainage path

The length of the drainage path is the distance the water needs to flow to drain from the area being analysed. The value for D is usually taken as half the thickness of the soil layer being analysed. If drainage occurs from one side only the value is taken as the total thickness of the soil layer.

2.6.2 Total Stress and Effective stress

The analysis for slope stability can be done either by using the total stress or the effective stress. The two methods can be summarised as follows (Turner and Schuster, 1996):

- The effective stress analysis relates the shear strength of the soil to the effective normal stress on the potential slip surface using the effective stress shear strength parameters. To do this the pore pressures within the soil must be known.

- The total stress analysis relates the shear strength of the soil to the normal stress on the potential slip surface by means of the total stress shear strength parameters. In this case the pore pressures in the soil do not need to be known for the analyses.

When conducting the total stress analysis for soils that do not drain during the loading period, the total stresses and effective stresses are obtained from laboratory tests. The principle involves subjecting a soil specimen to the same total stresses as would be experience in the field. The same excess pore water pressures will develop and thus the effective stresses would be the same as well. The soil strength is governed by the effective stresses and therefore the soil strength measured in the laboratory should be the same as the strength of the soil in the field if the pore water pressures and the total stresses are the same. The strength of the soil under undrained conditions can therefore be related to the total stresses. This principle is reasonably simple, however there are several factors that influence pore water pressures that develop under undrained loading (Turner and Schuster, 1996), i.e.:

- Degree of saturation
- Density
- Stress history of the soil
- Rate of loading
- Magnitudes and orientation of applied stresses

The test specimen used to obtain the shear strengths need to resemble conditions in the field closely in order to use the results for the undrained total stress analysis. This is however still the preferred method compared to predicting the undrained excess pore pressures for use in effective stress analysis during undrained conditions.

2.6.3 Shear strengths

The shear strengths that are used in analyses are measured with two methods (Turner and Schuster, 1996):

- In tests conducted in the laboratory or in the field where the loads are applied slowly enough not to create excess pore water pressures and the soil reacts under drained conditions.
- In consolidated undrained triaxial tests conducted in the laboratory during which the pore pressures are measured and the effective stresses at failure can be calculated.

The values for the effective stress strength calculated from these two methods have been found to be the same (Bishop and Bjerrum, 1960). When working with stiff clays, Skempton (1970, 1977, 1985) found that the peak drained strengths are larger than the peak drained strengths that can be mobilised in the field over a long period of time. It was recommended by Skempton that the “fully softened” strengths of stiff clays should be used where sliding has not taken place in the material. This is because once sliding has taken place, the clay particles are reoriented parallel to the slip surface and the strength therefore decreases progressively as the sliding displacement takes place and ultimately reaches a low residual value. This value, which is referred to as the residual shear strength, should be used in clay slopes where a slope failure has occurred. To calculate the fully softened shear strength the clay sample should be remoulded at a moisture content close to the liquid limit and reconsolidated in the laboratory. The strength is then measured in a normally consolidated condition.

Turner and Schuster (1996) suggested that for partially saturated soils such as compacted clays and naturally occurring clayey soils, the undrained strengths should be measured with unconsolidated-undrained tests on samples with the same void ratio and degree of saturation. The unconsolidated-undrained tests are performed on undisturbed samples from the field. The undrained strength measured from these tests represents the strength of the soil at the time and place where the soil was taken, depending on whether the samples taken remain undisturbed. The samples that are called “undisturbed” samples are never truly undisturbed and are never completely free of disturbance effects.

2.6.4 Unit Weights and Water Pressures

The main requirement in slope stability analysis is to satisfy equilibrium with regard to total stresses. This is the case with effective stress analysis as well as with total stress analysis. With effective stress analysis the shear strength is related to the effective stresses and with total stress analysis the strength is related to the total stresses. The total stress is the prime variable in both cases when evaluating the equilibrium conditions in terms of the fundamental mechanics, because the soil and water forces need to be included. The effective stress analysis involves subtracting the pore pressure from the total stress at the base of each slice to determine the values of the effective stress, which the soil strength is related to. This is not necessary for the total stress analysis because the strength is related to the total stresses. To formulate a correct analysis in terms of total stresses, the total unit weights and external boundary water pressures can be used. The total unit weights are the moist unit weights above the water table and the saturated unit weights below the water table. The water pressures that act on submerged boundaries of the slope should

be included for the correct evaluation of the equilibrium conditions as they have an effect on the total stresses (Turner and Schuster, 1996).

2.6.5 The Effect of Moisture Change on Embankments

The pore water pressures within railway embankments which are affected by the amount of moisture found in the slope is influenced by weather patterns and the vegetation found on the slope (Loveridge et al., 2010; O'Brien et al., 2004; Scott et al., 2007). The negative pore pressures described as suctions usually occur during dry periods and the positive pore water pressures occur during wet periods when water infiltrates the soil (Smethurst et al., 2006).

The seasonal change in moisture contents creates progressive slope movements and degrades the soil. Tension cracks are a likely occurrence at the crest of the embankment and shear ruptures at the toe of the embankment (Take and Bolton, 2004). In clay fill embankment the seasonal change in moisture content creates a shrinkage and swelling of the material which can disturb the track geometry and serviceability (Smethurst et al., 2015). Shrinkage of the material during dry periods can result in surface cracking to occur. These cracks can allow water to infiltrate the embankment and accelerate the re-wetting process of the embankment during wet periods and reduce the number of wetting and drying cycles required for failure to occur. The closure of the cracks due to swelling of the material during the wet periods tends to be in a downward direction due to the gravitational forces. This contributes to the downward slope movement of the material which can cause shallow surface failure. This process is called surface creep. If the shrinkage cracks that formed during the dry periods are excessive and deeper the downward movement may penetrate deeper and result in more severe failures (Hughes et al., 2009).

Embankments which are largely saturated with limited water storage capacity are susceptible to pore water pressure increases towards hydrostatic conditions under long periods of heavy rainfall (Briggs et al., 2013). As mentioned before the infiltration of rainfall into slopes can reduce the suction sufficiently to trigger shallow slope failures (Fourie, et al., 1999).

In order to investigate the likelihood of these scenarios as a result of climate change a combination of physical and numerical modelling and testing has to be done. Physical modelling in the form of centrifuge testing has the ability to simulate long time-series events but has limitations in terms of small-scale instrumentation that can be used and to simulate the interactions between the soil and vegetation (Hughes et al., 2009).

2.7 SOIL DEFORMATION UNDER LOADING

2.7.1 Resilient Deformation Behaviour

A well designed rail structure will produce predominantly recoverable (resilient) deformations under a moderate static load. Repeated loads will however cause irrecoverable or permanent strains. Resilient behaviour can be described by the resilient modulus which in turn is used to predict the behaviour of soil layers under cyclic loading (Gräbe and Clayton, 2014).

The resilient modulus E_r is the stiffness calculated from the recoverable strains under repeated loading and unloading of a soil. The resilient modulus is normally calculated from stress and strain values that are obtained from a triaxial test and is equivalent to the Young's modulus (Bishop and Henkel, 1962):

$$E_r = \frac{q_r}{\varepsilon_r} \qquad \textbf{Eq. 2.13}$$

Where:

q_r = Repeated deviator stress or stress pulse

ε_r = Resilient strain

The resilient behaviour of a soil is influenced by a number of factors that are grouped in three categories (Li and Selig 1994; Lekarp et al. 2000).

- Loading condition and stress state including the size of the deviator stress and confining stress, the number of cycles, the sequence and the stress history.
- The type and structure of the soil. This includes the aggregate type, particle shape, fines content and grading. It also includes the compaction method and compaction effort.
- The physical state of the soil which is defined by the moisture content, void ratio and the density all of which are affected by environmental changes.

2.7.2 Cyclic Loading

Cyclic loading can be defined as a system of loading which exhibits a degree of regularity both in magnitude and in its frequency. There are a few aspects that can be identified related to cyclic loading that should be noted (O'Reilly and Brown, 1991):

- The effect of stress intervals
- Rate dependent response of the soil
- Dynamic effects where static analysis becomes inapplicable

Stress reversal in this sense does not mean a change in the sign of the stress but the change in the sign of the rate of stress increase. The rate dependant response of the soil is the influence of the rate of loading or the rate of strain on the strength and stiffness of the soil. This can be attributed to two factors, namely the viscous inter-particle behaviour of the soil as well as the time dependent dissipation of the excess pore pressure generated during the loading in situations where drainage is allowed. This is evident in clays where the shear strength increases when higher strain rates are applied. The dynamic effects are important when the frequency of the load is high. The dynamic effects complicate the analysis as factors such as damping, realistic modelling of boundary conditions and the stiffness of the materials at small strains become very complex (O'Reilly and Brown, 1991).

2.7.3 Permanent Deformation

The effect of long term loading has become more important with the rise in complete costs for railway life spans. This means that the effect of cyclic loading has to be assessed for a new rail track in order to estimate the lifespan of the foundation and replacement thereof (Gräbe and Clayton, 2009).

Vertical deformation from progressive shear strain is one of the results of repeated wheel loads. This is because the vertical stress during the loaded state is greater than the horizontal stress. The progressive volume change under repeated wheel loads that causes this vertical deformation can be summarised as a result of two reasons (Selig and Waters, 1994):

- Particle rearrangement to form a more dense structure
- Particle breakage causing smaller particles to move into voids

Progressive shear failure of the subgrade may have a great effect on embankment failure. The stresses imposed on the subgrade by the axle loads are large enough to cause progressive shear failure. This tends to occur in the top part of the subgrade where the cyclic load induced stresses are the largest. The overstressed soils are compressed and moved sideways from beneath the track and upwards which causes bearing capacity failure (Selig and Waters, 1994). This effect can be seen in Figure 2.16.

To reduce the probability of progressive shear failure to occur, the following can be done (Selig and Waters, 1994):

- Ensuring that there is an adequate load distributing granular material between the sleeper and the subgrade.
- Ensuring that the drainage systems maintain a low water table.

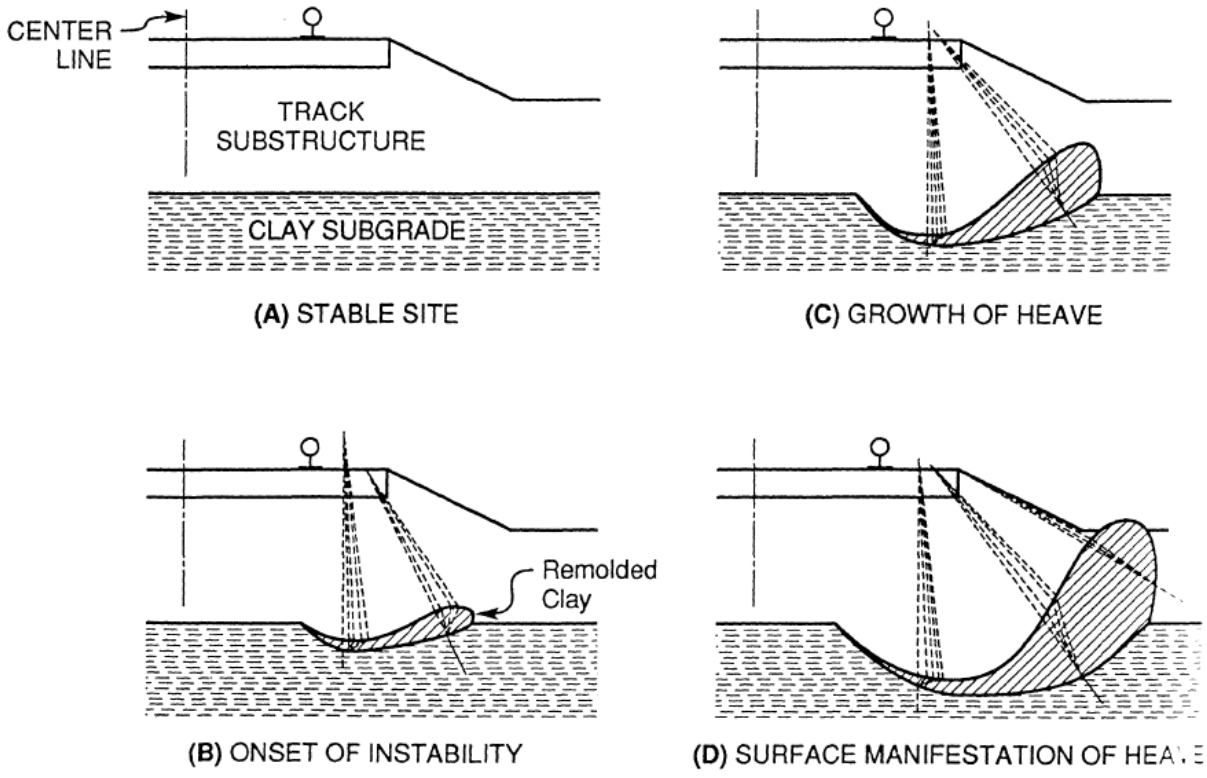

Figure 2.16: Progressive shear failure (Selig and Waters, 1994)

The loadings applied by heavy haul trains on a coal rail line will be the focus in this study. The coal trains consist of typically five traction locomotives with 200 four axle coal wagons. The locomotives are supported on six axles with 22 or 30 tonne loads per axle. The wagons are loaded with a 26 tonne/axle load on the track. The trains travel at 50 km/h -80 km/h which provides frequencies of 1 to 8 Hz (Gräbe and Clayton, 2009).

This study considers the effect of the entire train load on the embankment for the duration that it takes the train to cross the embankment length. This means that a low frequency is considered and that the following effects of high frequency cyclic loading is not applicable:

- Rate dependent response of the soil such as the dissipation of the excess pore pressure generated during the loading in situations where drainage is allowed and viscous inter-particle behaviour of the soil.
- Damping and realistic modelling of boundary conditions.

2.8 CENTRIFUGE MODELLING

2.8.1 Physical Modelling in a centrifuge

Physical modelling in a centrifuge is an effective tool available to a geotechnical engineer. It allows the analysis of complex design problems using geotechnical materials. Small scale models can be accelerated to many times the magnitude of earth's gravity in order to simulate true stresses experienced in the soil for the prototype being modelled (Taylor, 1995).

Physical modelling in the centrifuge allows a better understanding of geotechnical events and therefore a better analysis and design can be completed. There are three categories of objectives when using model testing (Taylor, 1995):

- Studying a complex design problem.
- Studying a general problem.
- A detailed study of stress changes and displacements in accordance with a particular class of problem.

Centrifuge tests have the greatest value for qualitative studies of mechanisms of deformation and failure. This is because the models tested in a geotechnical centrifuge can be constructed so that they simulate the

geometry and stresses in the prototype slopes and therefore they are capable of simulating the modes of deformation and failure expected in the field. Testing in the centrifuge also has the potential to create model case studies which represent years of equivalent full-scale slope behaviour (Take and Bolton, 2004). The limitation of centrifuge experiments is the difficulties in constructing centrifuge models that accurately mimic the important details of the full scale prototype and the loading conditions it will experience (Turner and Schuster, 1996).

2.8.2 Scaling Laws

Using a length scale that is inversely proportional to the gravity scale is very common in centrifuge modelling. A $1/N$ scale model is thus tested at an acceleration of Ng, where N is a gravity acceleration scaling factor. Important scaling relationships for dynamic centrifuge modelling are represented in Table 2.2 (Taylor, 1995).

Table 2.2: Scaling factors for centrifuge model tests (Kutter, 1992)

Quantity	Symbol	Units	Scale Factor
Length	L	L	$1/N$
Volume	v	L^3	$1/N^3$
Mass	m	m	$1/N^3$
Acceleration, Gravity	a, g	L/T^2	N
Force	F	mL/T^2	$1/N^2$
Stress	σ	m/LT^2	1
Moduli	E	m/LT^2	1
Strength	s	m/LT^2	1
Time (dynamic)	t_{dyn}	T	$1/N$
Frequency	F	$1/T$	N
Time (diffusion)	t_{dif}	T	$1/N^2$

2.8.3 Previous Loading Mechanism and Instrumentation

Loading instrumentation used by Vinogradov et al. (2010) to represent a train load will be discussed in this section. The goal of the cyclic loading device used in tests conducted by Vinogradov in the centrifuge was to represent a load as close as possible to the prototype being modelled to ensure the effects are as true as possible. The load should represent a passing train. This type of loading from trains causes vibratory and dynamic influences on subgrade soils. The dynamic loads on the embankment create an impulse of varying bandwidth to be applied from different origins, i.e. from the axle of the wheel pair and from the damping mass. To create such a loading device, electromagnetic power vibrators were used. The power interactions between the ferromagnetic fields were used in the vibratory elements. The loading recreated by this loading device simulated the load at one point on an embankment and created the load of each wheel load of the train passing that point on the embankment at a certain speed. The device is shown in Figure 2.17 (Vinogradov et al. 2010):

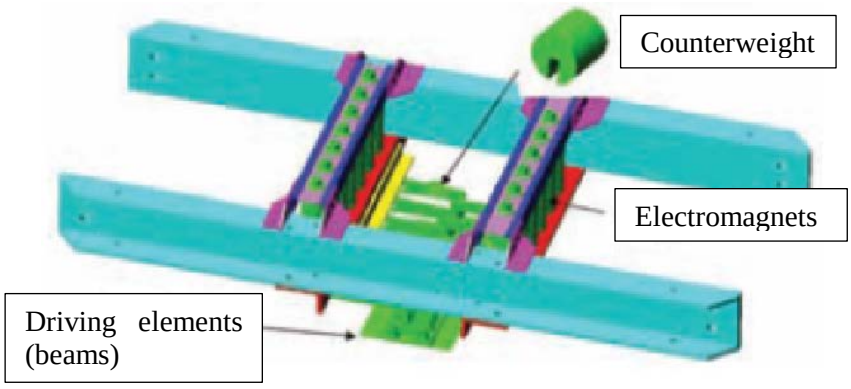

Figure 2.17: Loading device used in MIIT Centrifuge (Vinogradov et al. 2010)

2.9 SUMMARY

To analyse the stability of a railway embankment under cyclic loading a number of factors have to be taken into account. The slope stability analysis can be done using the various limit equilibrium methods of slices developed for this purpose. This will normally be done using computer aided analysis. The effective stress and shear strength of the soil is governed by whether the soil is fully saturated or unsaturated. The moisture content and the suctions present in the soil therefore play an important role in the strength and stability of the embankment. Atterberg limits can describe the moisture related characteristics of soils and the soil water characteristic curve describes the behaviour of the soil as a result of suctions at different moisture contents. The effects of cyclic loading play an important role in the behaviour of the subgrade of the rail structure. Progressive shear failure is largely affected by cyclic loading and through progressive shear failure, embankment failure can occur. Permanent settlement is as a result of particle rearrangement and breakage. Testing in the geotechnical centrifuge will incorporate instrumentation to represent the total load created by a passing train on a stretch of embankment for a number of cycles.

The study is based on embankment failures that have occurred on the Ermelo-Richards Bay heavy haul line in South Africa. These failures consist of shallow slip surfaces and deep seated failures. When using the method of slices, only a static load is used in the analysis. The effects of cyclic loading on the embankments are therefore neglected in the design. Fatigue analysis and the effects thereof on the failure mechanisms are therefore not taken into account. Centrifuge modelling provides an ideal opportunity to find a more realistic way to model railway embankments and investigate the effects of cyclic loading. It is believed that the cause of these slope failures is as a result of cyclic loading in conjunction with an increase in moisture content.

3 EXPERIMENTAL SETUP

To investigate the influence of static and dynamic loading on the failure of railway embankments, different centrifuge models were built and instrumented. This chapter describes equipment used, testing methodologies considered, processes followed as well as methods used for data acquisition.

3.1 LOADING INSTRUMENTATION DEVELOPMENT

Two methodologies were considered for the simulation of the train loading. The initial loading methodology that was considered was similar to the loading created by Vinogradov et al. (2010) as discussed in Section 2.8.3 which simulates the loading at one point on the embankment and uses an electromagnetic shaker. The second loading methodology simulates the complete loading of the train over a section of embankment using a loading block. These two loading methodologies are discussed below.

3.1.1 Electromagnetic Shaker

The loading recreated by this loading device simulates the load at one point on an embankment and creates the load of each wheel of the train passing that point on the embankment. The speed at which the train travels plays a significant role in the loading characteristics that have to be simulated. This combined with the wheel spacing and loading curve created by the train passing a point on the embankment, is used in the design of the loading device.

The speed at which the train travels and the wheel spacing between the four wheel load configurations of the wagons are used to determine the frequency between the loading increments. The four wheel load configuration is the loading created by the set of four wheels shown in Figure 3.2. The scaling factor for dynamic time variables or frequencies for centrifuge testing plays a significant role in the design process of the loading device. These scaling factors can be seen in Table 2.2. Various train speeds and g-forces were considered to determine the scaling capabilities of the electromagnetic shakers. The spacing between the four wheel load configurations for the wagons are 12.07 m. This was calculated using the dimensions of the jumbo wagons as shown in Figure 3.1 and is shown in Figure 3.2.

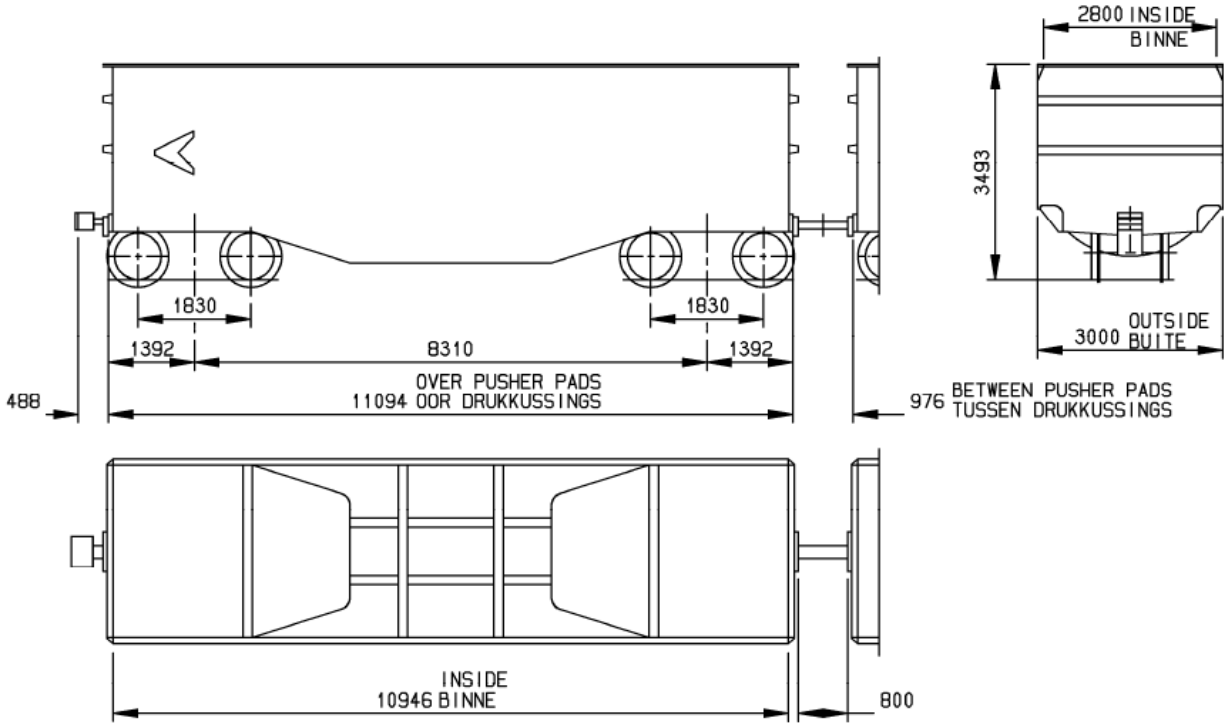

Figure 3.1: Jumbo wagon dimensions

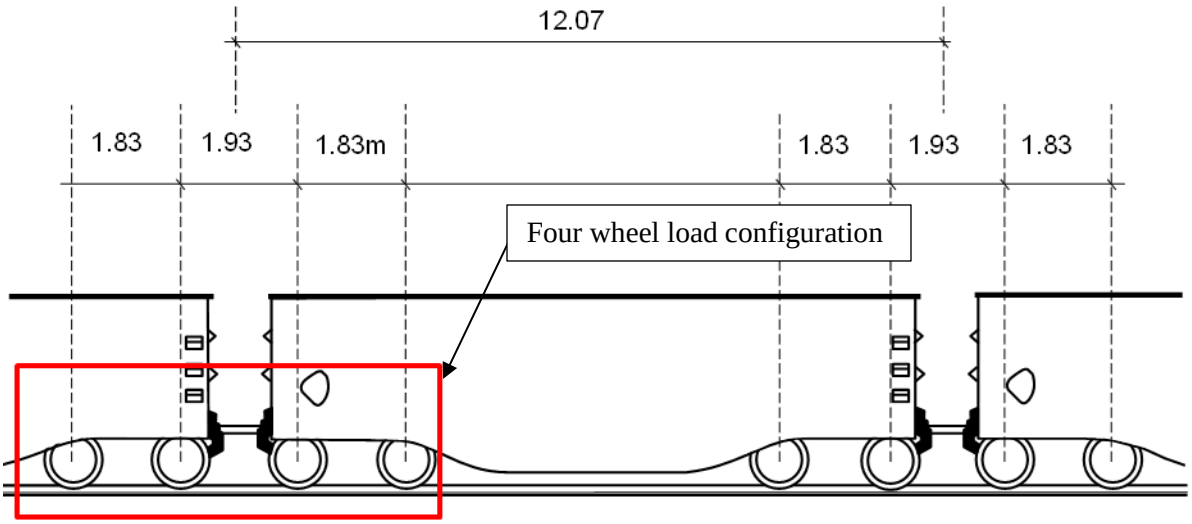

Figure 3.2: Jumbo wagon wheel spacing (Dimensions shown in meters)

A back calculation was done from the model frequency at different g-forces to calculate the train speed which would be simulated shown in Figure 3.3. Using the values in Figure 3.3, a suitable electromagnetic shaker could be chosen. The desired prototype speed of the train to be modelled is 80 km/h. The calculation process followed to convert this to a prototype and model frequency is shown below using 50 g-force as an example:

Speed: $80\ km/h \div 3.6 = \ 22.22\ m/s$

Time taken per cycle: $12.07\ m\ \div 22.22\ m/s = 0.543\ s$

$1\ Hz = 1/s$

$\frac{1}{s} = \frac{1}{0.543} = 1.84\ Hz\ (Prototype)$

$1.84 \times N\ = 1.84\ Hz\ \times 50\ g = 92.02\ Hz\ (Model)$

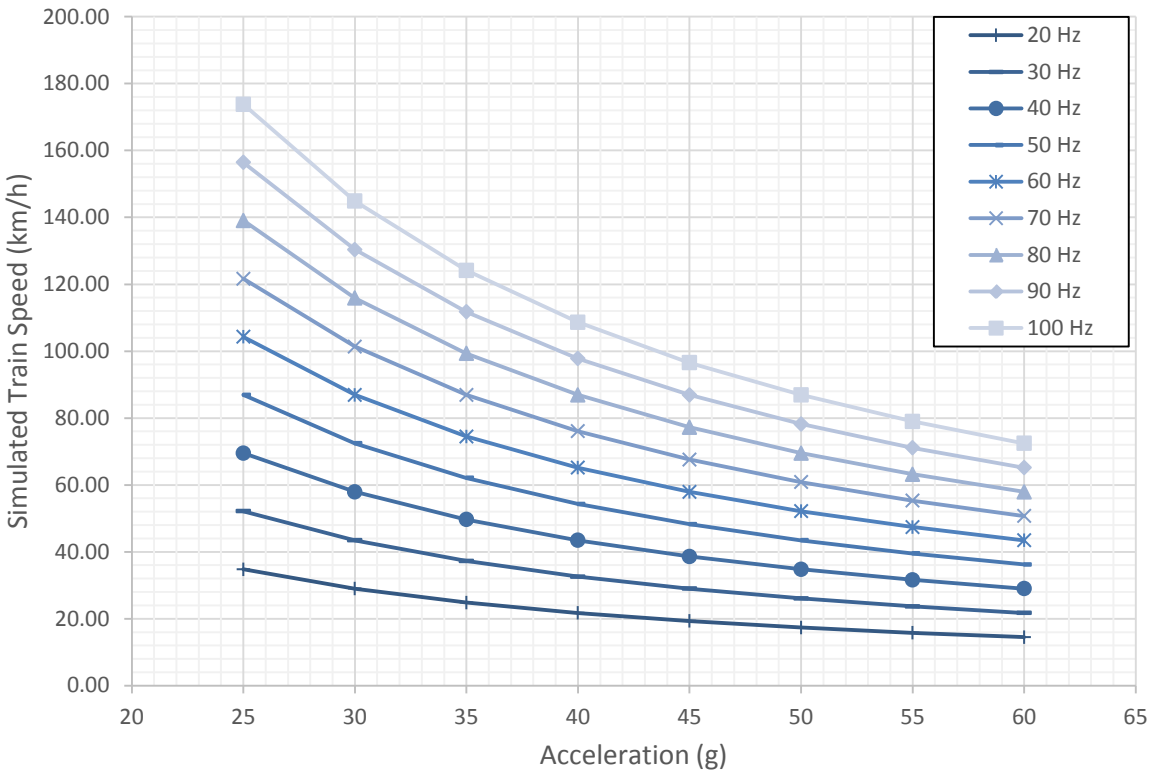

Figure 3.3: Model frequencies compared at different train speeds and g-forces

For the electromagnetic shaker to reproduce a specific loading cycle curve, the correct loading amplitude has to be recreated. This means the electromagnetic shaker has to be programmable to reproduce the right frequency and be capable of withstanding the g-force created by the geotechnical centrifuge. The loading amplitude is dependent on the weight of the shaker combined with the weight added to the shaker or removed with a counter weight to obtain the correct scaled weight for the model.

Various difficulties arose when attempting to reproduce the loading curve created by a train passing a certain point on an embankment with an electromagnetic shaker in the geotechnical centrifuge. These are listed below:

- Procuring or developing an appropriate shaker that can create the desired amplitude and frequency.
- Procuring or developing a shaker that can withstand the high g-forces in the geotechnical centrifuge.
- The high cost of a shaker that can fulfil these requirements.
- Building the necessary mechanism and instrumentation attached to the shaker to recreate the desired loading amplitude.
- Boundary effects created from the wave generation through the soil from the high frequency loading.

Taking all of these factors into account, it was decided to use a loading block and pneumatic piston to create the train loading on the embankment as described in the following section.

3.1.2 Loading Block and Pneumatic Piston

This loading methodology simulated the complete loading of the train over a section of embankment using a dead weight. The loading block represented the loading created by a 26 $tonne/axle$ wagon loading with a complete wagon load of 104 $tonne$. The load was calculated and represented per meter in order to create the same loading along the entire length of the embankment. The loading increment was controlled by a pneumatic piston lifting and lowering the loading block on the embankment at a specific loading cycle. To attach the loading block and piston to each other a u-channel was used. The loading block and piston can be seen in Figure 3.4.

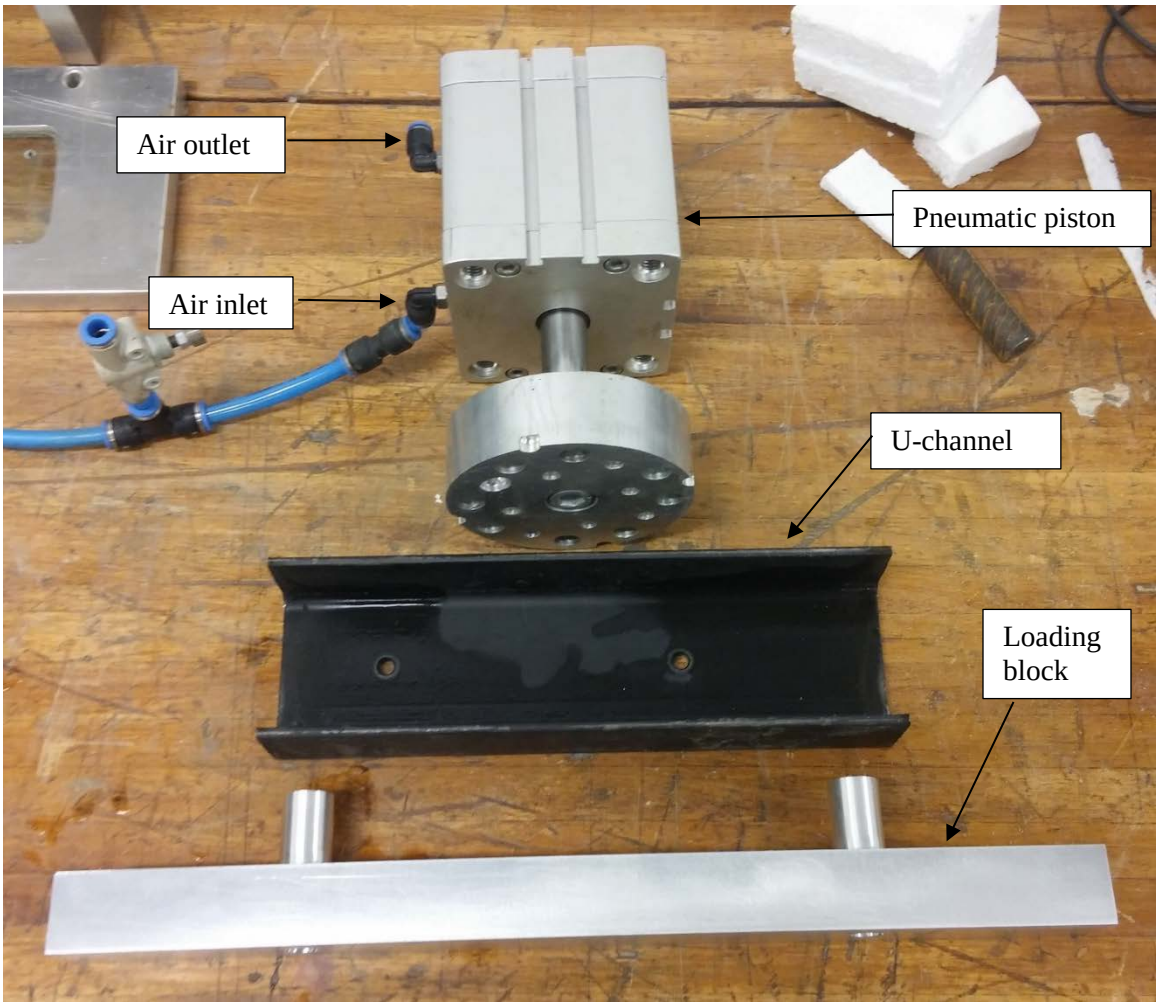

Figure 3.4: Loading block and pneumatic piston

The loading block was machined to have the exact mass and width to represent the loading created by a train on the track structure on an embankment. The loading block was machined from a solid piece of aluminium. A schematic of the loading block design can be seen in Figure 3.5.

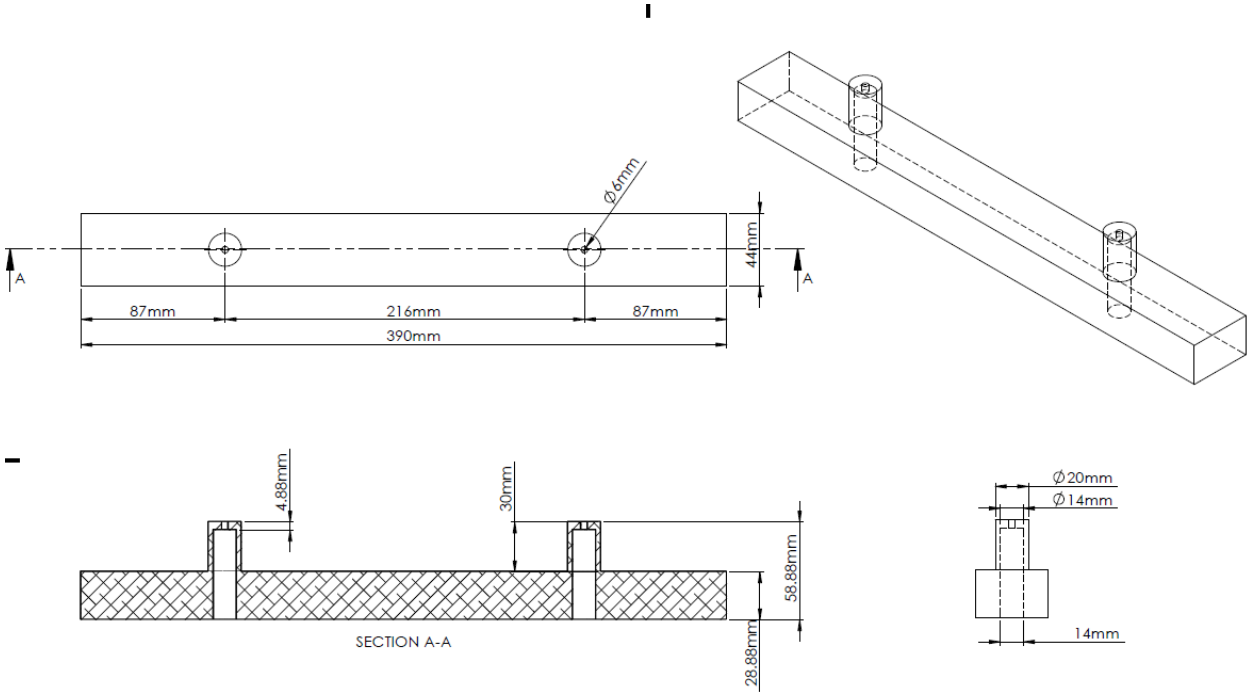

Figure 3.5: Schematic of train loading block

The block had two support fixtures where the lifting supports from the pneumatic piston were positioned. These extended above the main body of the block in order to incorporate any large settlement which may be experienced during the test. The lifting supports were not attached to the loading block to have no effect on the loading created by the self-weight of the loading block on the embankment. The position of the lifting supports can be seen in a side cross section of the loading block in Figure 3.6. The spacing of the lifting support on the loading block was calculated so that the maximum deflection that could be experienced at the ends and middle of the block would be the same.

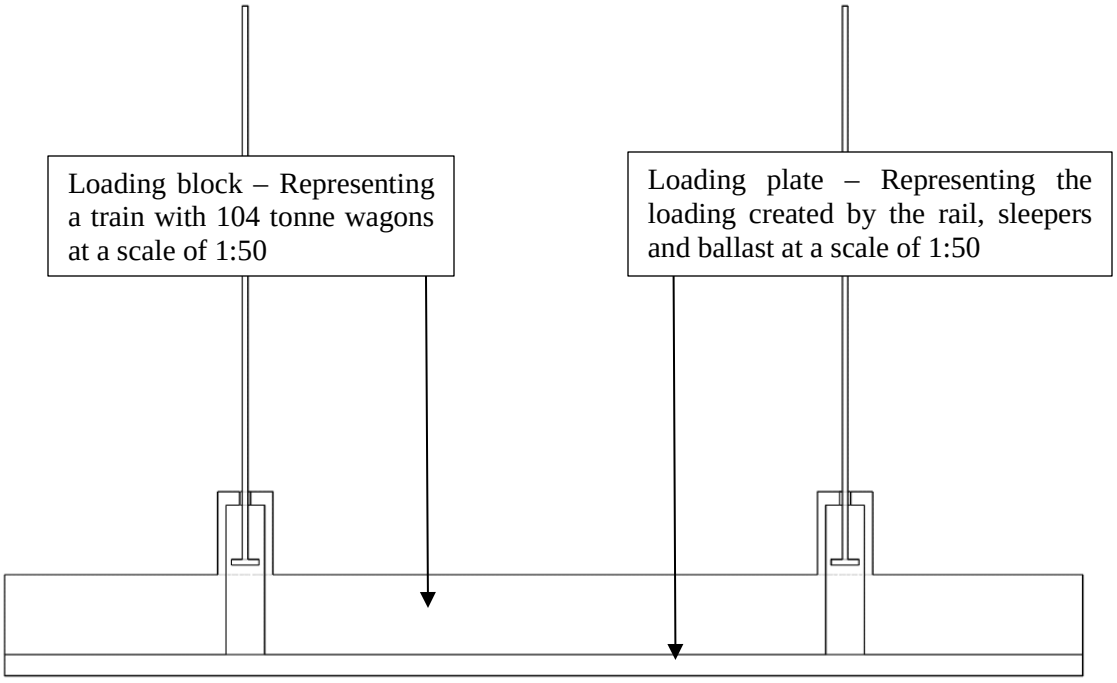

Figure 3.6: Cross section of loading block showing the position of the lifting supports.

A separate loading plate was machined to replicate the loading created by the track structure on the embankment. The track structure taken into account was the rail, sleeper and ballast. The weight from PY-sleepers (282 $kg/sleeper$) and 60 kg/m rail were used with a conservative ballast density of 2000 kg/m^3. The plate dimensions were:

- Height: 7.65 mm
- Length: 390 mm
- Width: 100 mm

A photo of the final machined loading block and plate can be seen in Figure 3.7.

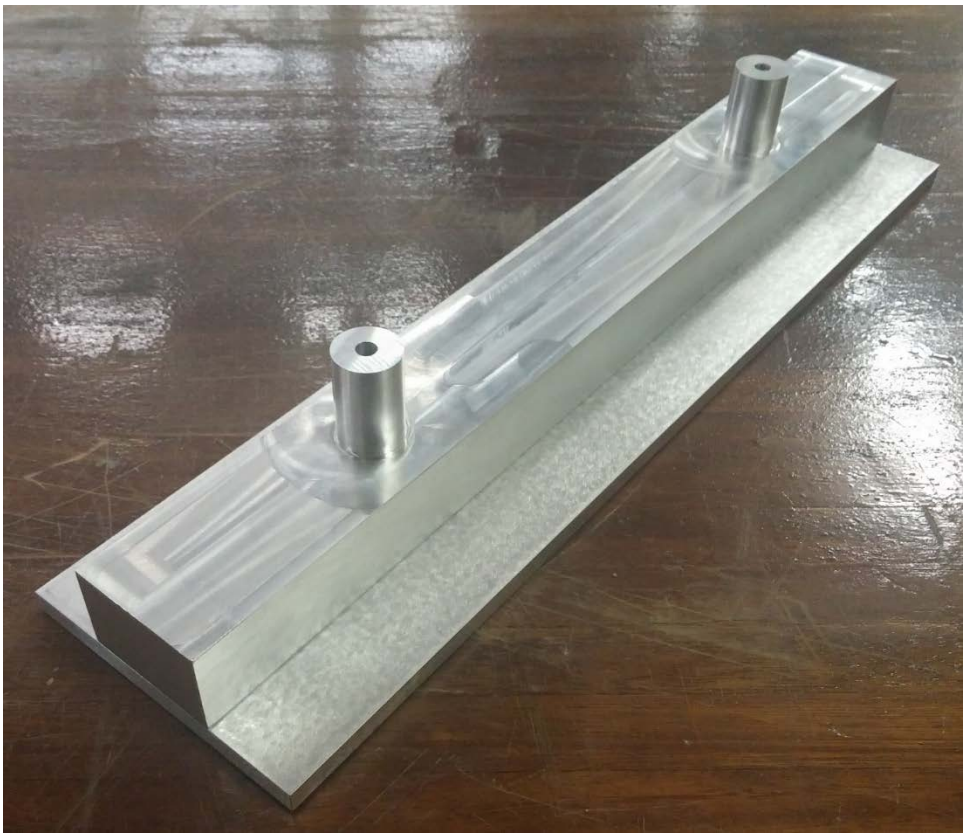

Figure 3.7: Final loading block and plate

3.2 CENTRIFUGE INSTRUMENTATION AND EQUIPMENT

The geotechnical centrifuge that was used for the tests at the University of Pretoria is an Actidyn C67-4, 150 g-ton centrifuge. The centrifuge has a radius of 3 m and the model platform is 0.8 m x 1.0m. The centrifuge can be seen in Figure 3.8 with the plan and elevation view of the centrifuge in Figure 3.9 (Jacobsz et al., 2014)

Figure 3.8: Geotechnical centrifuge at the University of Pretoria

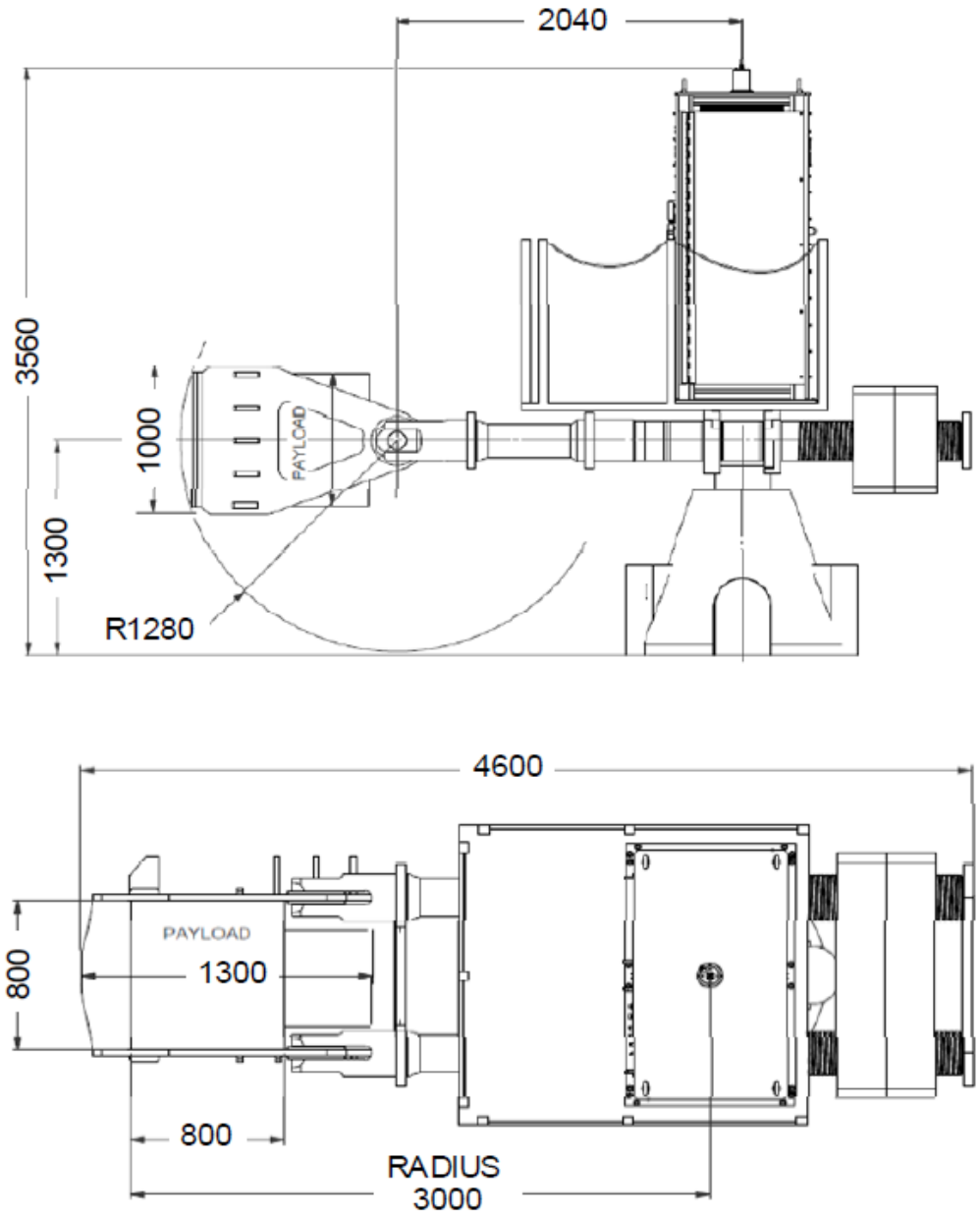

Figure 3.9: Elevation and plan view of geotechnical centrifuge (Jacobsz et al., 2014)

The centrifuge is capable of carrying a payload of 1500 kg to 100 g or 950 kg to 130 g with a maximum operating speed of 208 RPM (Jacobsz et al., 2014). The layout of the test and the major components used in the tests can be seen in Figure 3.10. These components are discussed in more detail below.

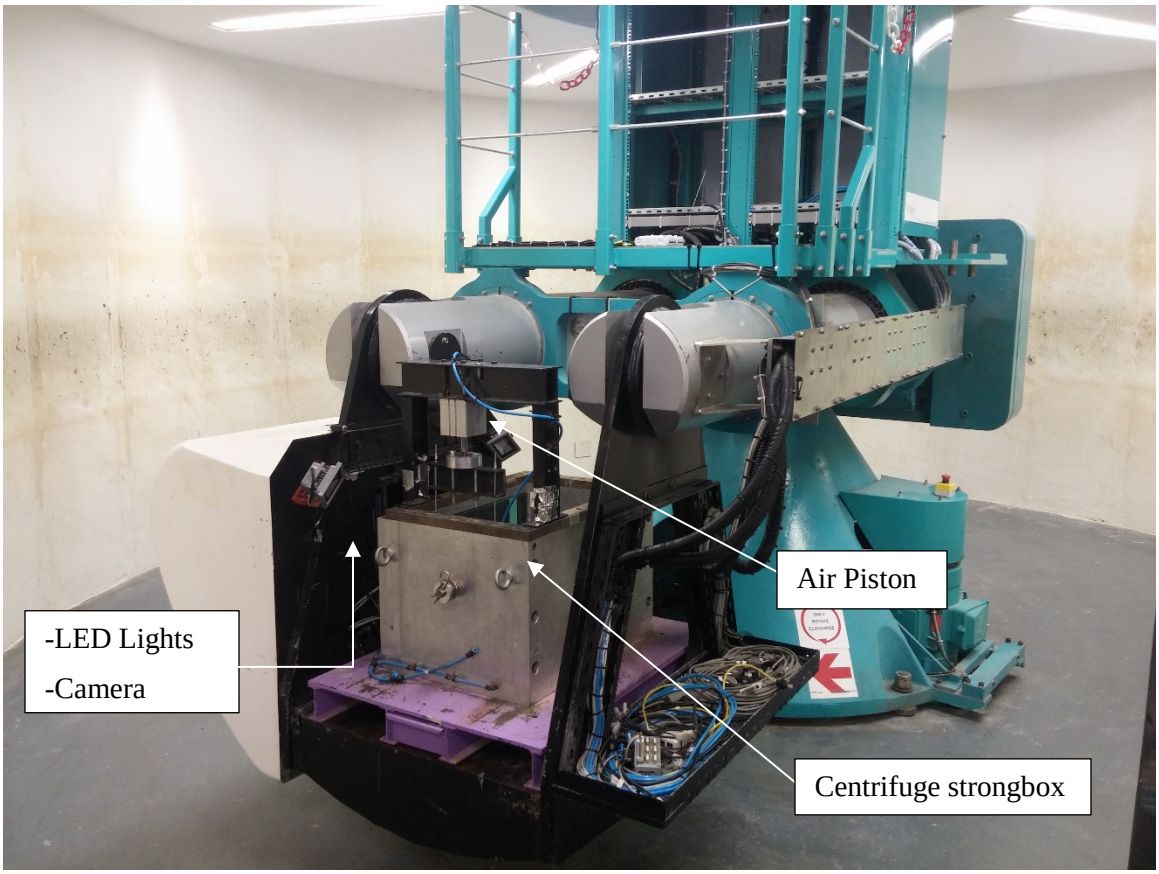

Figure 3.10: Test setup on the geotechnical centrifuge

3.2.1 Centrifuge Strongbox

The strongbox is used to house the models which will be tested in the geotechnical centrifuge. The strongbox is made of an aluminium alloy and has an 80 mm glass window as shown in Figure 3.11. It is designed to withstand accelerations up to 130 g during testing in the geotechnical centrifuge.

The dimensions of the strongbox are as follows:

- Outside length = 700 mm
- Outside height = 468 mm
- Outside depth = 530 mm
- Inside length = 600 mm

- Inside height = 400 mm
- Inside width = 400 mm

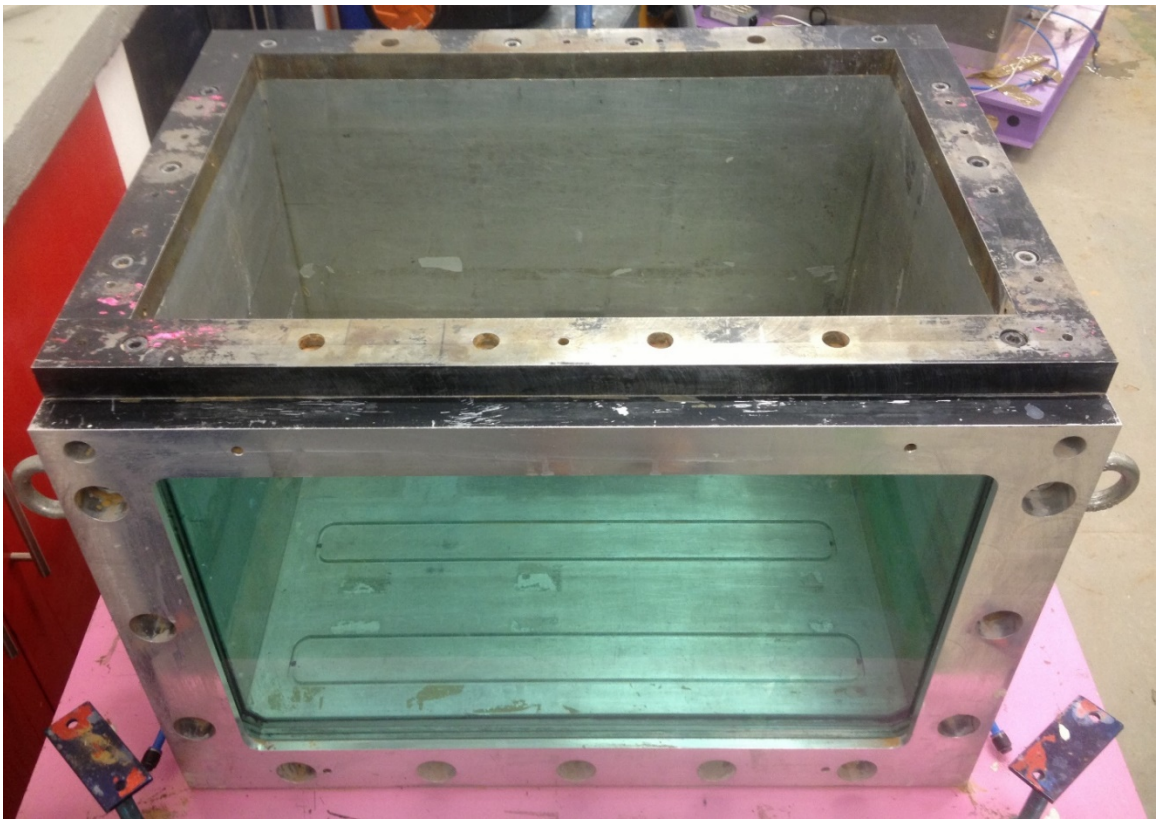

Figure 3.11: Geotechnical centrifuge strongbox with window

3.2.2 Strongbox Divider

The strongbox divider is used when smaller models are to be tested in the geotechnical centrifuge. It decreases the strongbox inside dimensions to:

- Inside length = 600 mm
- Inside height = 400 mm
- Inside width = 300 mm

A photo of the strongbox divider can be seen in Figure 3.12. The use for the strongbox divider is discussed in Section 3.4

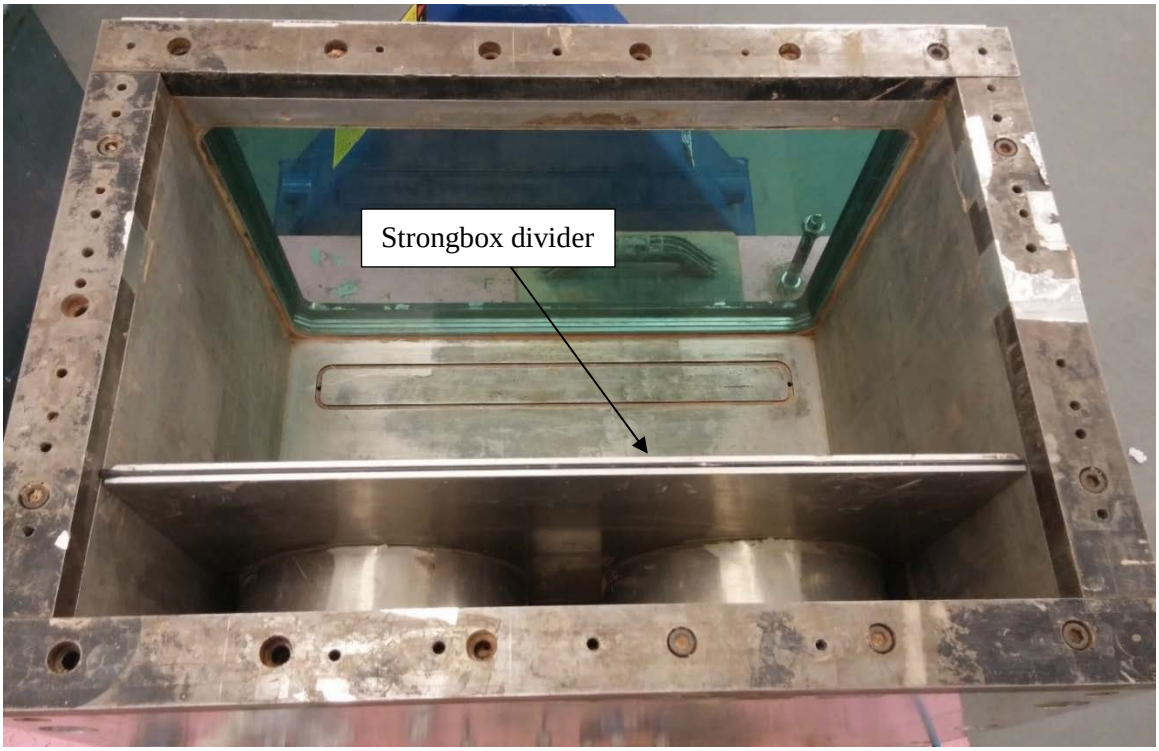

Figure 3.12: Strongbox divider

3.2.3 Pneumatic Piston

The Piston is a Festo ADN-80-50-I-P-A with a diameter of 80 mm and a stroke length of 50 mm. A photo of the piston can be seen in Figure 3.13. As mentioned in Section 3.1.2 the pneumatic piston is used to lift and lower the loading block onto and off the embankment. The loading methodology is discussed in further detail in Section 3.5.

Figure 3.13: Pneumatic piston for load application

3.2.4 Solenoid Valves

A solenoid valve is a valve controlled by electricity. When a current is applied, the valve is opened and when no current is applied the valve is closed. The solenoid valve was used to control air flow to the Pneumatic Piston discussed in the previous section. The solenoid valve can be seen in Figure 3.14.

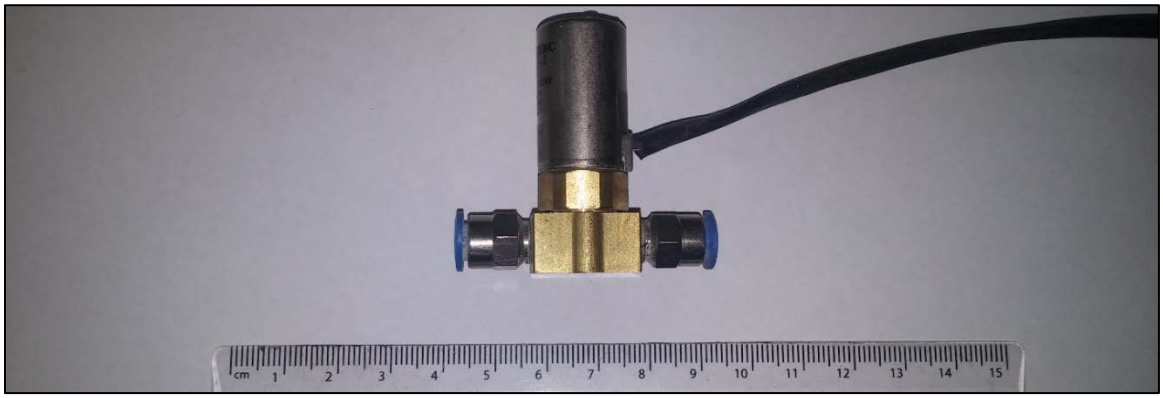

Figure 3.14: Solenoid valve connected to the pneumatic piston

3.2.5 Regulator valves

The regulator valve controls flow rate of air or water through a system. The regulator valve was used to control rate of air flow in and out of the Pneumatic Piston. The regulator valve can be seen in Figure 3.15.

Figure 3.15: Regulator valve

3.2.6 Linear Variable Differential Transformer (LVDT)

The LVDTs used were Solartron Metrology AS/15 S series with 30 mm displacement sensors. The specifications for the LVDTs are given in Table 3.1 with the calibration curve given in Figure 3.16 (Archer, 2014). The data acquisition from the LVDTs is described in Section 3.6. A photo of the LVDT can be seen in Figure 3.17.

Table 3.1: LVDT AS/15 S Specifications (Archer, 2014)

Description	Value
Range	30 mm
Excitation voltage	1-10V
Sensitivity	60 mV/V/mm
Type	Guided core
Body diameter	19 mm
Calibration factor	3 mm/V

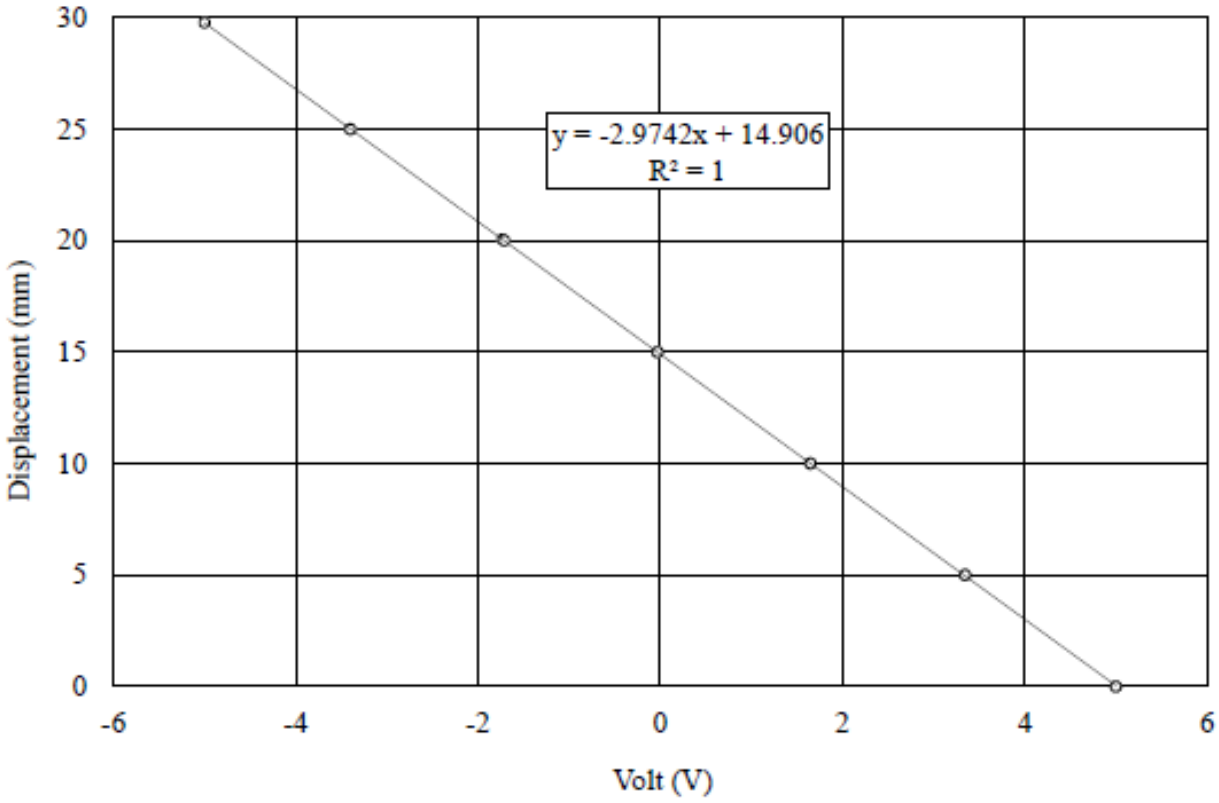

Figure 3.16: Calibration curve for LVDT (Archer, 2014)

Figure 3.17: LVDT AS/15 S

3.3 MODEL DEVELOPMENT

The material and design of the embankment chosen for the testing in the geotechnical centrifuge were based on the embankment slope failures that occurred on the Ermelo - Richards Bay coal line as discussed in Section 2.2. The material and preparation thereof, as well as the embankment design for the model development are discussed below.

3.3.1 Material

It was decided to conduct the tests on material found at sites where slope failures have occurred. The site chosen is at kilometre 117 MP 14 on Line 2 close to Piet Retief. This is the site known as the Moolman slope failure site. The location of the site can be seen in Figure 3.18.

Approximately 400 kg of material was collected from the site to conduct the tests and obtain the foundation indicators from. The foundation indicator tests were done by a commercial laboratory. Two samples from the 400 kg bulk sample were tested to gain a representation of the material. A summary of the material properties can be seen in Table 3.2 with the particle distribution of the samples in Figure 3.19.

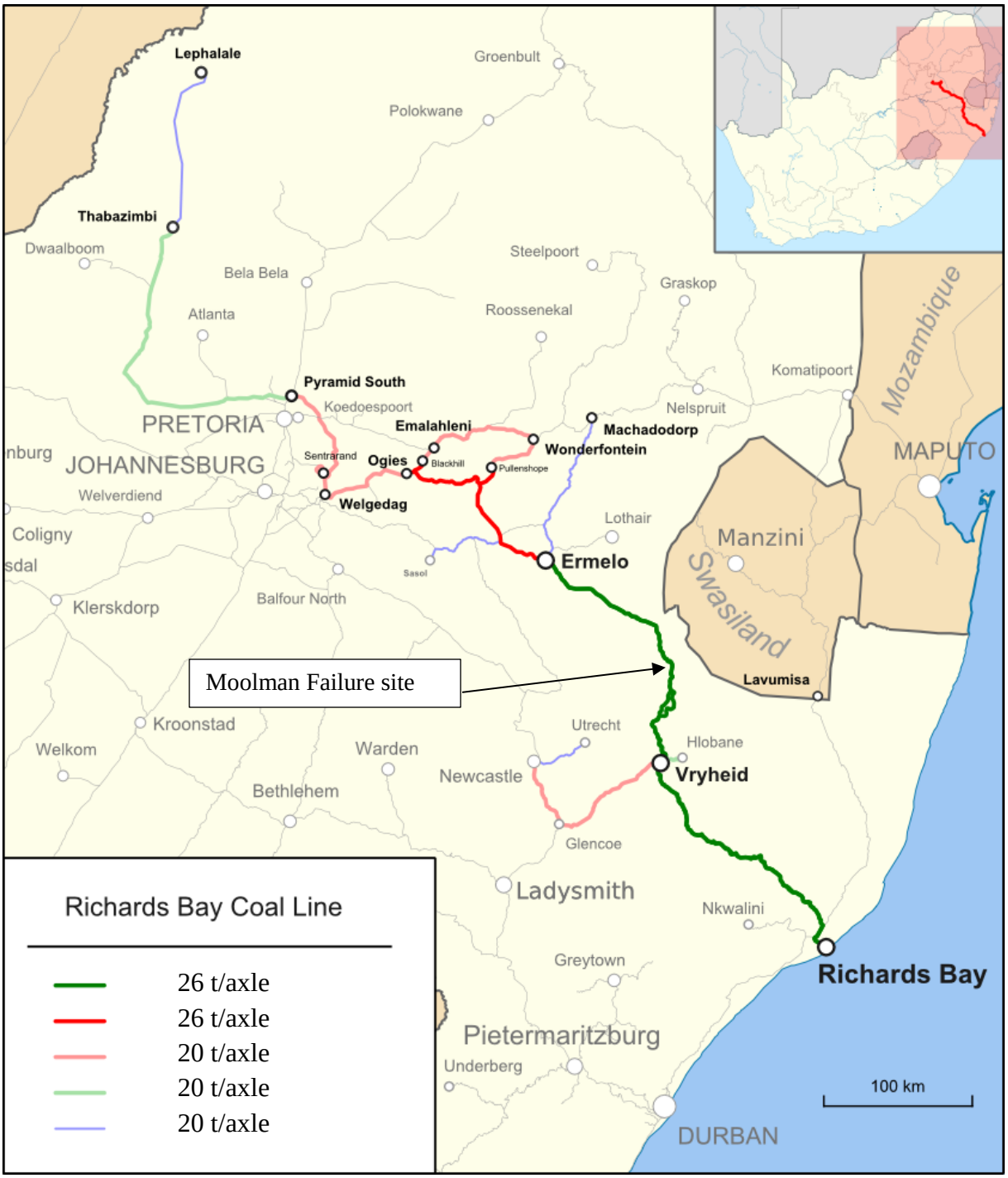

Figure 3.18: Moolman slope failure site (Wikiwand, 2015)

Table 3.2: Material Properties

Foundation Indicators		
Property Description	**Sample 1**	**Sample 2**
Maximum Dry Density (kg/m^3)	1880	1782
Optimum Moisture Content (%)	9.2	11.5
Specific Gravity (g/cm^3)	2.703	2.693
Atterberg Limits		
Liquid Limit (%)	40	43
Plastic Limit (%)	23	26
Plasticity Index (%)	17	17
Weighted PI (%)	12	12
Linear Shrinkage (%)	3	4
Grading Modulus	0.97	0.93
Soil Classification		
% Gravel	6	7
% Sand	62	52
% Silt	24	32
% Clay	8	9
Unified Classification	SC	SC
TBR Classification	A - 6	A - 7 -6
CBR (Modified AASHTO) TMH1 A8		
% Swell	1.3	4.1
90%	1.7	0.8
93%	1.9	0.8
95%	2.1	0.9
97%	2.2	1.2
98%	2.3	1.3
100%	2.4	1.6

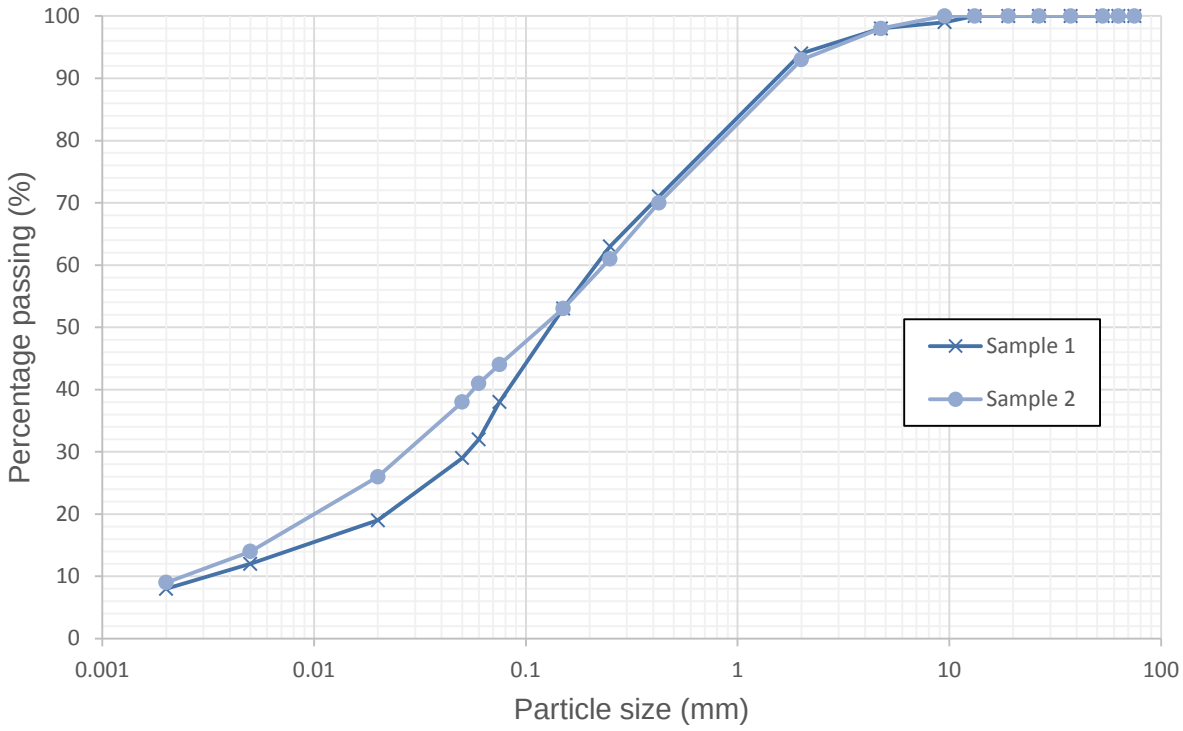

Figure 3.19: Particle size distribution of soil samples from site

The preparation of the material for the centrifuge tests involved sieving out all particles greater than 2 mm size as well as any organic and foreign matter. The material had to be dried and crushed thereafter in order to sieve the material. The material was dried at 60 ℃ to prevent damaging the clay particles in the soil.

After the sieving process the material was graded using a Mastersizer. The Mastersizer is an apparatus that uses laser diffraction to determine particle sizes. The machine sends a laser beam through the particles being examined and then takes readings of the intensity of the laser beam as it is scattered through the particles (Malvern, 2005). The results from the Mastersizer are given in Section 4.1.

The Mastersizer has a size range from 0.02 µm to 2000 µm. The result for each particle size is given as a percentage of the total volume. The D_{10}, D_{50} and D_{90} particle sizes are calculated. The particle size where 10% of the material is smaller than that size is called the D_{10} size of the sample. The same applies for D_{50} and D_{90}.

Consolidated-Undrained triaxial tests were done on three samples of the sieved material to obtain the friction angle of the material. The preparation of the samples was done at a specified compacted density and moisture content. This as well as the results from the triaxial tests are discussed in more detail in Section 4.1.

Drying tests were conducted on the material used for the centrifuge and triaxial tests to obtain the soil water characteristic curves in order to investigate the approximate soil suctions in the slope at different moisture contents and correlating it with the slope stability. The results from the drying tests are discussed in Section 4.1.

3.3.2 Embankment Model Design

The design of the embankment model was based on the standard design specifications used for embankments on the heavy haul coal line and on the slopes from the case studies where slope failures occurred on that line. The standard embankment slope was designed at a 1:1.5 ratio (33.7^{o}). The top of the embankment allowed for a 5 m wide ballast section with 0.5 m shoulder on either side as well as a 6 m wide service road. A schematic of the embankment cross section is shown in Figure 3.20. The failures that occurred in the case studies were all on the upper 12m of the embankments and therefore it was decided to scale the embankment model accordingly.

The bulk earthworks of the embankments were designed to be compacted at 93% Mod. AASHTO. This compaction is however rarely achieved and the material often has a compaction of maximum 90% Mod. AASHTO. The specified compaction for the embankment model was selected as 90% Mod. AASHTO to replicate the failures from the case studies described in Section 2.2.

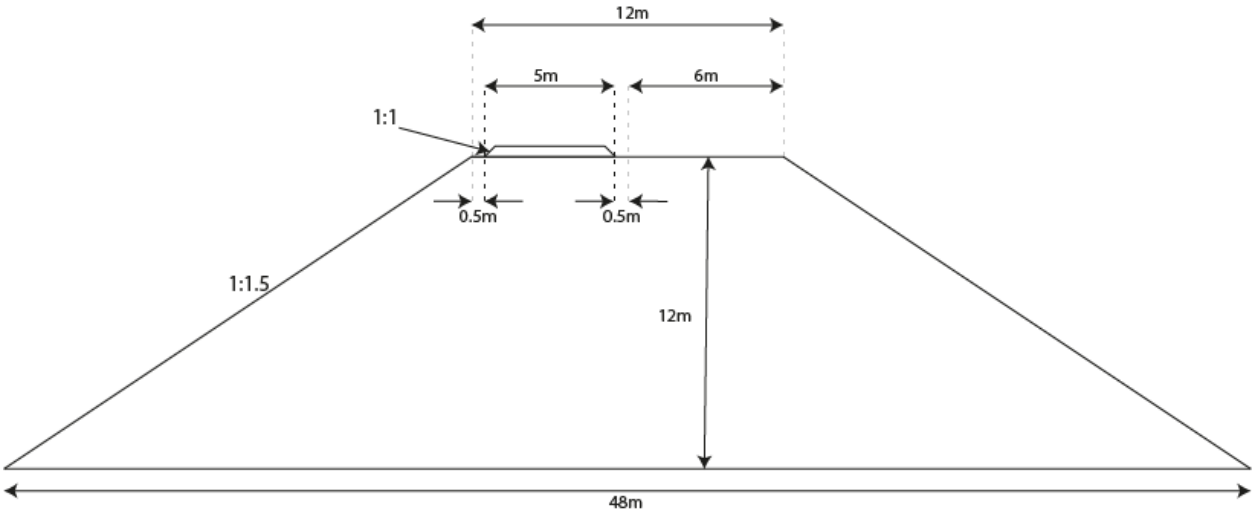

Figure 3.20: Standard embankment design cross section

Due to the size restrictions of the strongbox that would be used for the tests, the embankment model had to be simplified to one side of the embankment cross section as shown in Figure 3.20. The final cross section used for the tests can be seen in Figure 3.21 with the simplified setup layout with the loading block and piston in place in Figure 3.22. The model is scaled to a ratio of 1:50 and would therefore need to be tested at an acceleration of 50 *g* in the geotechnical centrifuge to recreate the embankment prototype and the true stresses that would be experienced at full scale.

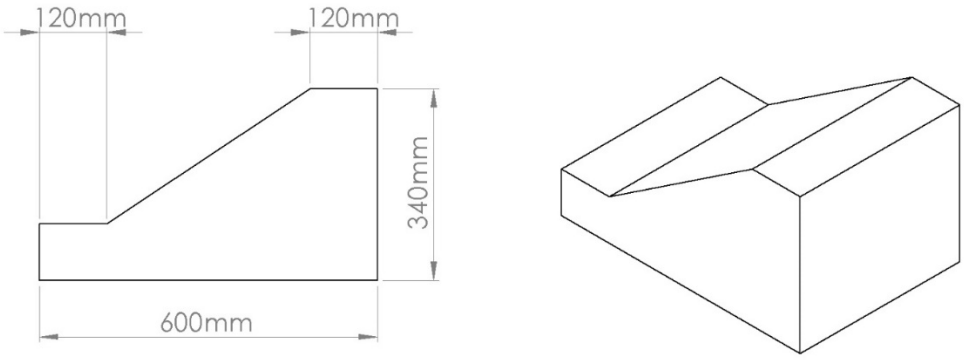

Figure 3.21: Final embankment model schematic (scale 1:50)

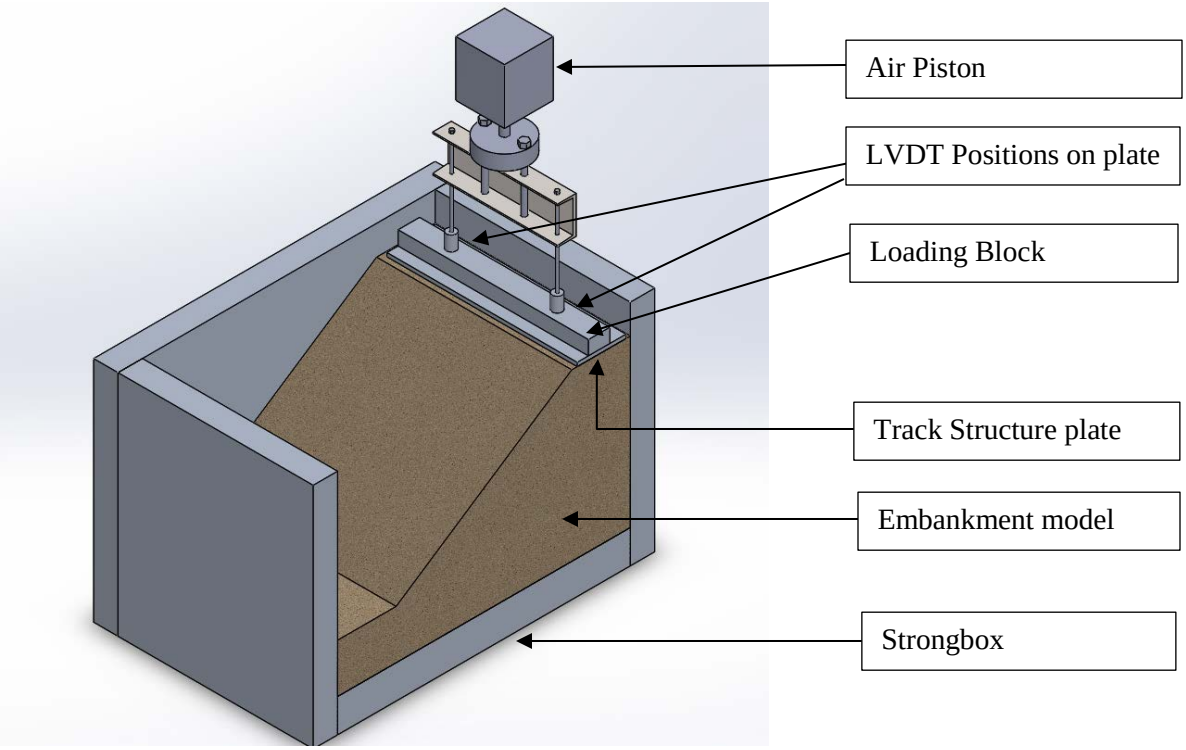

Figure 3.22: Final assembly in strongbox

3.4 MODELLING PROCESS AND PROGRESSION

This section describes the progression of the modelling process. Two modelling methodologies were followed for the different tests. The first was where the compaction process was done outside the strongbox in a separate box after which the model was placed in the strongbox and the other, where the compaction was done inside the strongbox.

Both modelling processes involved compacting the soil in the box to the final height of the embankment and thereafter carving out the required embankment cross section. This was done to ensure the correct dry density was achieved throughout the model embankment. The compaction was done in ten layers to obtain a uniform compaction throughout the embankment model.

3.4.1 Compaction and modelling process outside strongbox

The initial methodology involved compacting the model in a separate box which could be dismantled to carve out the required embankment cross section. The reason for compacting the soil in a separate box was to remove the risk of scratching the centrifuge strongbox window during the compaction process. The separate wooden box used for the compaction process can be seen in Figure 3.23.

Figure 3.23: Separate wooden box for the compaction process.

After the compaction process was completed in the wooden box, the sides were removed to expose the model in order to carve out the cross section. Due to the excessive force and pressure created as a result of the compaction, the sides of the wooden box deformed and kicked out. The result of this can be seen in the curved side of the compacted model in Figure 3.24. This problem was addressed by adding steel angle profile reinforcing around the sides on two levels as seen in Figure 3.25

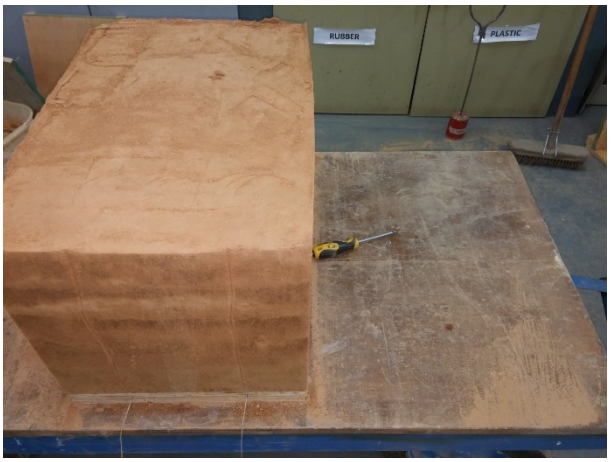

Figure 3.24: Deformation experienced during compaction in the wooden box

Figure 3.25: Angle profile steel reinforcing to address deformation

In the tests where higher moisture contents were used, the model embankment's sides stuck to the side panels of the wooden box due to the suctions created. The result thereof is shown in Figure 3.26. This was addressed by adding galvanised steel sheeting to the insides of the panels and coating it with a thin layer of shutter oil. The galvanised steel sheeting can be seen in Figure 3.27.

Figure 3.26: Model sides sticking to wooden box panels

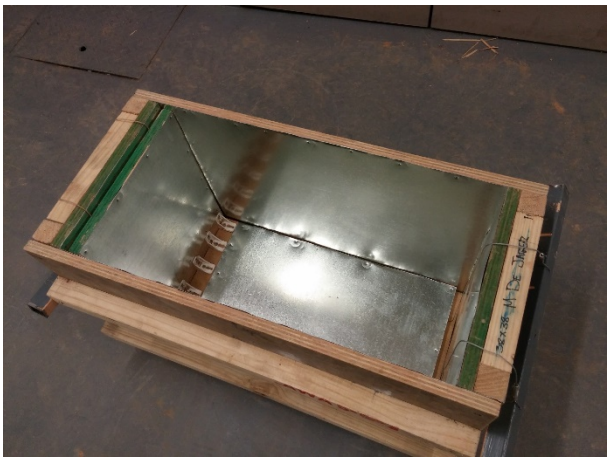

Figure 3.27: Galvanised steel sheeting added to insides of the wooden box

The carving process and the finished embankment model can be seen in Figure 3.28 and Figure 3.29 respectively. It was observed that the higher moisture content models swelled once the panels were removed and during the carving process.

Moisture loss was also a challenge during the carving process. Once the carving process was completed the embankment model was moved and placed in the strongbox using a forklift and steel cables as shown in Figure 3.30 and Figure 3.31.

Figure 3.28: Embankment carving process

Figure 3.29: Finished embankment model

Figure 3.30: Moving embankment with the forklift

Figure 3.31: Placing embankment in strongbox

To minimise disturbing or damaging the embankment model, during placing in the strongbox, the dimensions of the wooden box were decreased. The strongbox divider was then placed behind the embankment to keep it in place during the test. The smaller embankment model in the strongbox can be seen in Figure 3.32 and the strongbox divider in Figure 3.33. The final model setup can be seen in Figure 3.34.

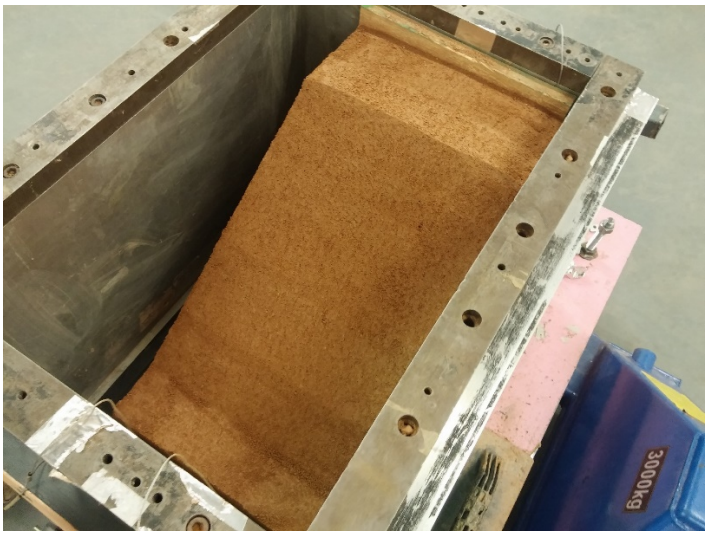

Figure 3.32: Decreased size of embankment model

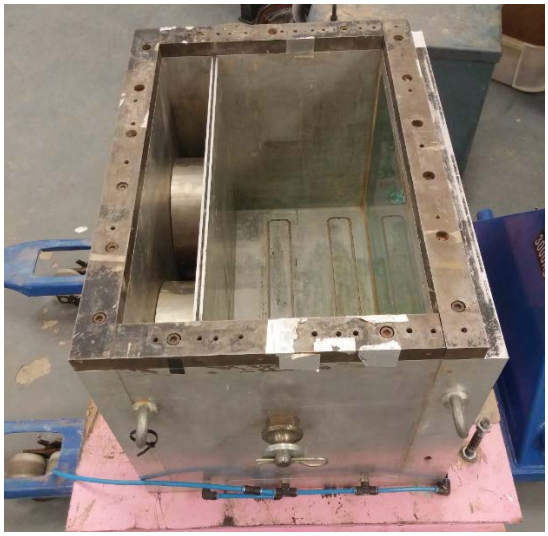

Figure 3.33: Centrifuge strongbox divider

Figure 3.34: Final model setup after compaction outside strongbox

The main disadvantages when the modelling and compaction was done outside the strongbox are summarised below:

- Swelling of the material once the wooden box panels were removed.
- Soil sticking to panels and being pulled off.
- Moisture loss during the carving process.
- Deformation and disturbance of model during placement in the strongbox.
- Small spaces and gaps between the model and strongbox after placement.

3.4.2 Compaction and modelling inside strongbox

To overcome the disadvantages from the modelling process that arose when the compaction and modelling was done outside the strongbox, it was decided to place a 1 mm polycarbonate panel inside the

strongbox against the window to avoid any risk of scratching the strongbox glass. A new polycarbonate panel was used for each test as it scratched heavily during the carving process and the removal of the model after testing.

To carve out an exact embankment model for each test inside the strongbox, the cross section and compaction layers were drawn on the strongbox divider as seen in Figure 3.35 to assist with the compaction and carving process.

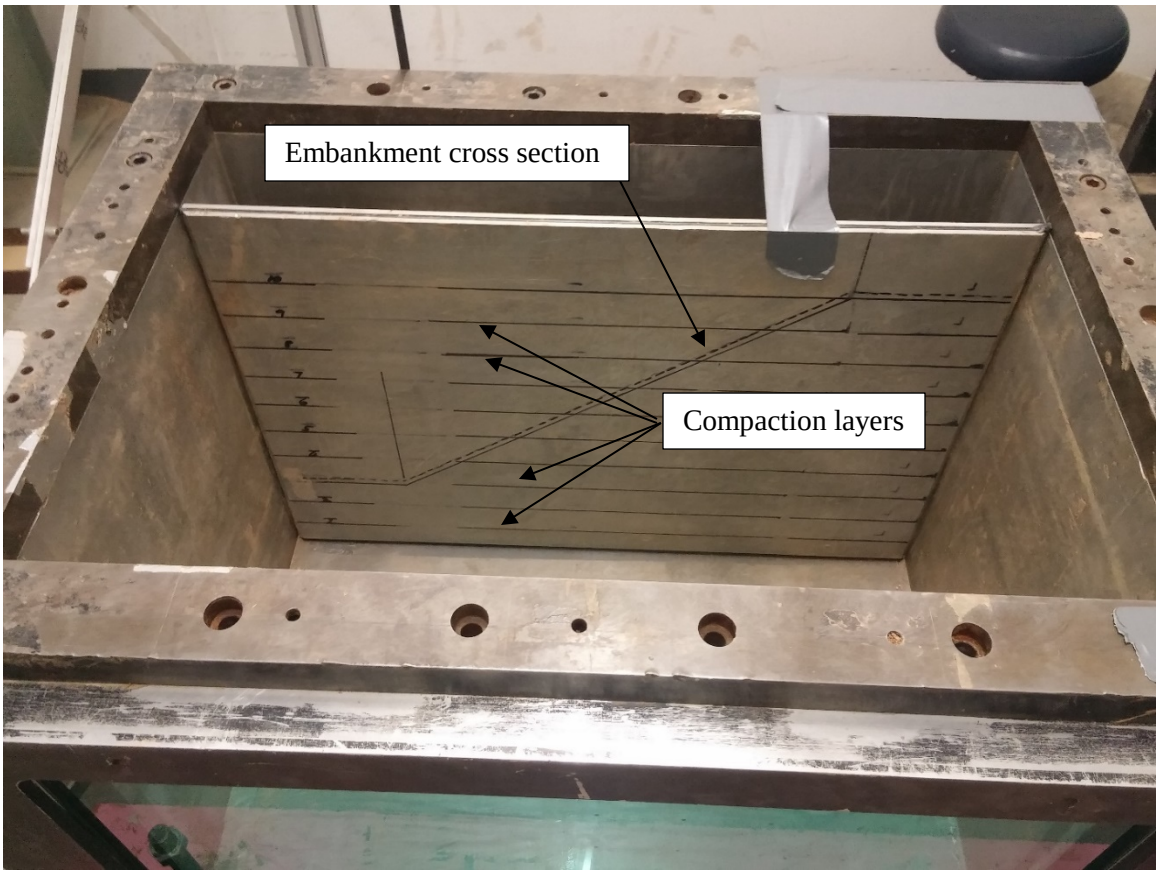

Figure 3.35: Cross section and compaction layers on strongbox divider

The compaction of the material was done using a Modified AASHTO test hammer and a wooden block to distribute the compaction force. Between each compacted layer, the material was scarified to create a better bond between the layers due to the smooth surface created by the compaction process. The

compaction process, scarified soil and the smooth surface can be seen in Figure 3.36, Figure 3.37 and Figure 3.38 respectively.

Figure 3.36: Compaction of material

Figure 3.37: Etching of material

Figure 3.38: Compacted surface

The disadvantages of modelling inside of the strongbox were mainly the carving process and the risk of damaging the glass of the strongbox when compacting. This was however overcome or mitigated and proved to be the preferred model preparation method.

3.5 LOADING METHODOLOGY

The embankment model was built to a scale of 1:50 and therefore the centrifuge was accelerated to 50 g acceleration in order to replicate the stresses in the desired prototype embankment. The loading should therefore be scaled accordingly to simulate the correct loading, pressures and loading cycles that would be experienced by the prototype embankment.

Two loading methodologies were followed during the tests conducted, namely static and cyclic loading. Both loads were applied using the loading block created as mentioned in Section 3.1.2. Before any loading was applied to the model, a stabilisation period of one hour was allowed once the centrifuge reached 50g acceleration. This was done to reduce the effect of settlement due to the self-weight of the embankment during the test. The loading block was kept elevated throughout the stabilisation period with the pneumatic piston. The loading process followed thereafter for the two loading stages are described below.

3.5.1 Static Loading

The static loading was applied for three hours after the one hour stabilisation period. The three hour period was chosen to allow enough time for settlement to occur in order to draw conclusions from the settlement curve.

3.5.2 Cyclic Loading

The cyclic loading was controlled using the pneumatic piston. The air flow to the piston was opened and closed using a solenoid valve. The Advantech Adam/Apax Utility program was used to control the cycles at which the air was opened and closed to the piston. The Advantech Adam/Apax Utility program allowed rules to be created for when the solenoid valve was opened and closed at a specific cycle rate.

The time per loading cycle was calculated using the time taken for a train to pass a certain section on the embankment. This was calculated using the train speed of 80 km/h and the train length of approximately 2.5 km. In order to calculate the loading time the dynamic time scaling factor, t_{dyn}, was used. The calculation and scale conversion is shown below:

$$\frac{Train\ Length}{Speed} = \frac{2.5\ km}{80\ km/h} = 0.03\ hours$$

$$Hours\ \times 60\ \text{min} = 0.03\ hours * 60\ min = 1.8\ min$$

Adjusting for the 50 g scale gives:

$$\frac{Time}{N} = \frac{1.8\ min}{50} = 0.036\ min$$

$$Min\ \times 60\ \text{sec} = 0.036\ min * 60\ sec = 2.16\ sec$$

This shows that approximate time taken for a train to pass over a section on an embankment at 80 km/h is 1.8 minutes. Tests were done to obtain the cycle time for the pneumatic piston to open and lift the loading block and to lower when the air is closed. Taking this and the time required for the loading to be applied on the embankment a cycle time of 10 seconds was chosen for the Advantech Adam/Apax Utility cycle rules which meant the solenoid valve was open for 10 seconds and closed for 10 seconds creating a complete cycle time of 20 seconds.

In order to compare the results to the static loading, the total time the cyclic loading is applied to the embankment during the tests was calculated by taking the loading time the block is on the embankment surface into account. During cyclic loading the time the load was on the embankment was approximately 2.5 to 3.5 seconds per 20 second cycle.

$$\frac{Cycle\ time}{Loaded\ time} = \frac{20\ sec}{2.5\ sec} = 8$$

Therefore, to compare the settlement during cyclic loading to the settlement during static settlement, the time the cyclic loading was applied was eight times longer than the static loading. The cycle and loading

time was governed by practical considerations and therefore the loading time could not be exactly the same as the loading time required as calculated above.

3.6 DATA RECORDING

The settlement of the embankment during the test needed to be measured as well as possible failure planes and the movement of the material during settlement. Any visual changes to the embankment model had to be noted such as shrinkage cracks that formed during the test or cracks created by material settlement. The effect of drying for the duration of the test on the embankment model also had to be taken into account. Data accumulation for this was done using the following methods:

- LVDT Data acquisition to measure the settlement.
- Particle Image Velocimetry (PIV) analysis using photos taken during the test to measure the displacement of material during failure or normal settlement.
- Visual inspections before and after the tests to analyse cracks that formed.
- Samples taken to measure moisture content after the test has finished.

The data acquisitioning system on the centrifuge was used to record data from the LVDTs. The LVDTs were connected to a DAQ module where data was recorded at a sampling rate of 1 Hz to capture the settlement of the embankment during the test. Two LVDTs were used for the tests that were placed on the plate representing the track structure. The movement of this plate represents the settlement of the embankment model. The positions of the LVDTs can be seen in Figure 3.39.

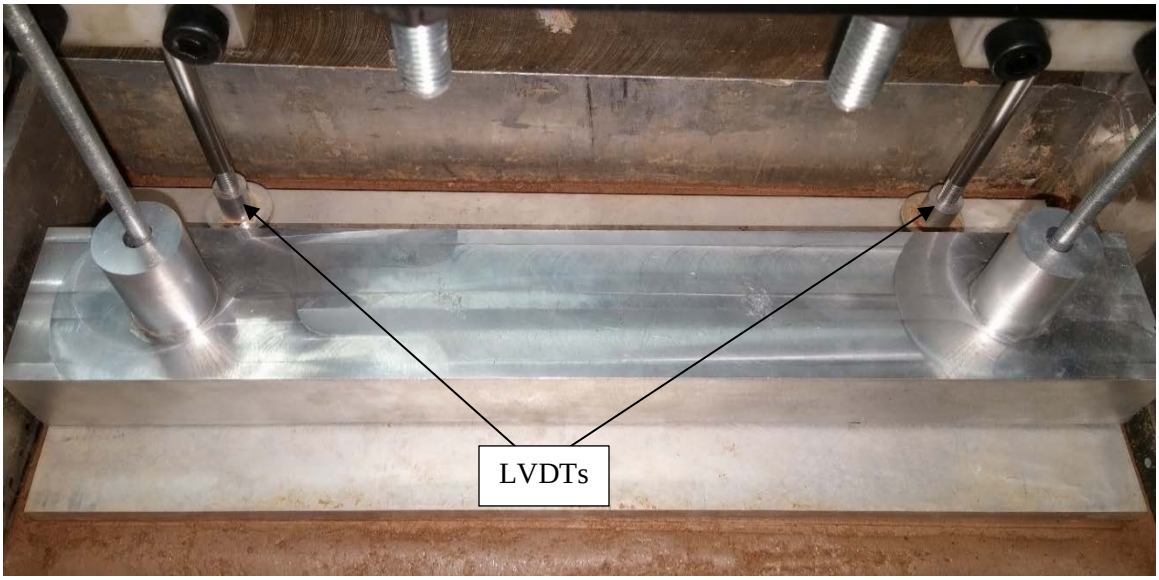

Figure 3.39: LVDT positioning for tests

The PIV method is an image processing tool that measures displacement and velocity instantaneously. PIV analysis is based on the principle of dividing an image into small patches and calculating the locations of individual patches in consecutive image frames with the help of cross correlation functions (Cilingir and Madabhushi, 2010).

Calibration is required for external deformation of parts during centrifuge modelling. Calibration software is used to take into account the negative effects of lens distortion, refraction and inclination between the image plane and the object plane. The performance of the PIV analysis strongly depends on the resolution of the recording device and images produced. This is because the amount of texture data per unit area increases with the increase in resolution. This is very important especially when working with soil particles. For example, if a sand grain with a diameter of 0.2 mm is to be captured as a pixel on the image device of 1 Megapixel resolution, the field of view has to be approximately 200 mm by 200 mm. For this study the PIV analysis was used to track the soil particle movement during embankment collapse and to track the soil movement once failure occurred.

The photos for the PIV analysis were taken using a Canon EOS 100D with a 40 mm Marco 0.3 m lens. A photo time lapse was used to take photos at certain time intervals. During the centrifuge acceleration period photos were taken every 6 seconds. Thereafter, during the stabilisation and loading periods of the tests, a photo was taken every 10 seconds. The PIV calibration points were initially printed on transparency and fixed to the strongbox window with adhesive transparent plastic. This worked for the

test with lower moisture contents but the adhesive transparent plastic lost its adhesion during the tests with higher moisture contents and resulted in the calibration points moving with the soil from the model during settlement. When the modelling process changed to the compaction process inside the strongbox, the transparency could be fixed between the polycarbonate panel (mentioned in Section 3.4.2) and the strongbox window. The calibration points can be seen in Figure 3.40.

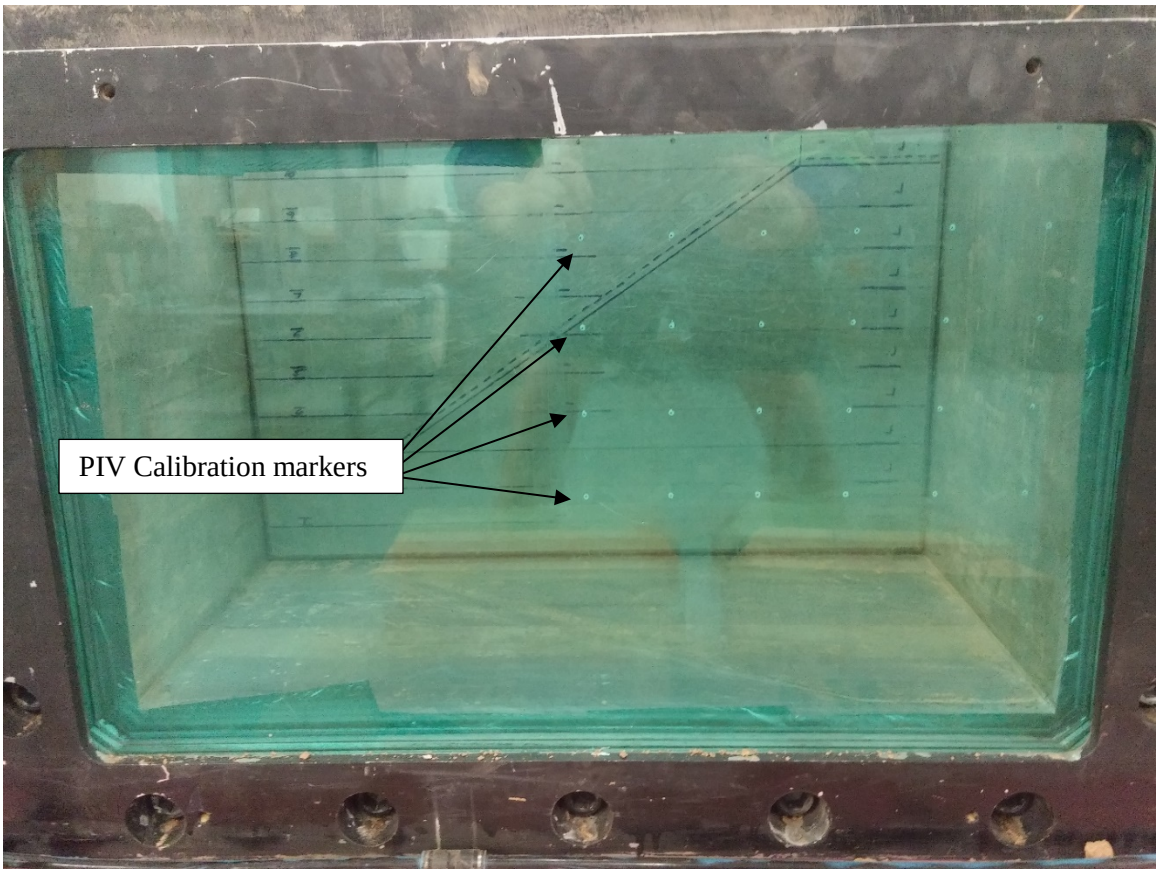

Figure 3.40: PIV calibration point between strongbox window and polycarbonate panel

After the test was completed, samples were taken at different height levels in the model embankment to measure the moisture content of the soil and the amount the soil has dried during the test. This was necessary to analyse the cracks that formed during the test to have a better understanding of whether the cracks were related to material shrinkage, settlement or slip planes. Examples of the samples taken at different height levels can be seen in Figure 3.41. Samples were generally taken at the top and bottom of the model and three levels in between.

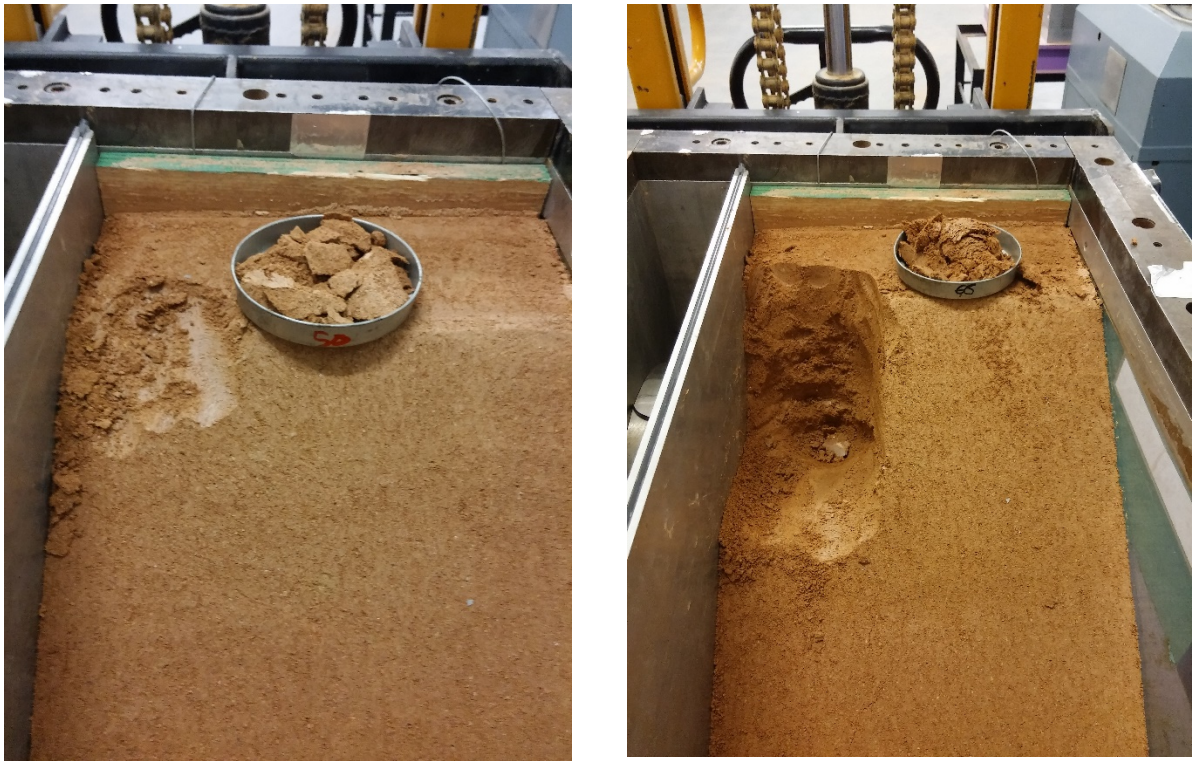

Figure 3.41: Example of sample taken at different levels for moisture content readings

3.7 CENTRIFUGE TESTS CONDUCTED

The tests conducted in the study served as an iterative process to find the moisture content at which a stable embankment model becomes unstable. The first four test served as trial runs to identify any problems with the testing methodology. These tests are labelled A1 to A4 in Table 3.3. The test setup and results for Tests A1 to A4 are given in Appendix A. The final six tests were conducted at three moisture contents (two tests per moisture content) to draw conclusions for the study. These tests are labelled B1 to B6 in Table 3.3. All the tests conducted in the centrifuge during the study are described below:

- An initial test was conducted at the optimum moisture content which was 10.4 %. For all the tests 1.0 % extra moisture was added to compensate for moisture loss during model preparation. This test served as a trial run to test the stability of the material under 50 g and to test the loading mechanism and loading cycle.

- The second test was done at 20.0 % moisture content. Cyclic and static loading were conducted in the same test. The test consisted of a 1 hour stabilisation period, 2 hours of static loading and 8 hours of cyclic loading.
- The third test was conducted at a moisture content of 28.5 %. This test was done at a large moisture content value to ensure an unstable embankment model was created.
- The fourth test was conducted at a 24.0 % moisture content. This is moisture content between 20.0 % and 28.5 %.
- The fifth to tenth tests were conducted at moisture contents of 21.0 %, 22.0 % and 23.0 %. At each moisture content, a static loading and a cyclic loading test was conducted.

A summary of the tests conducted with the different stages can be seen in Table 3.3

Table 3.3: Summary of tests conducted in the geotechnical centrifuge

Test	Moisture Content	% of OMC	Stabilisation period	Static Loading	Cyclic loading	Comments
A1	11.4 %	109.6%	None	None	1 hour 45 min	Water added to induce failure
A2	20.0 %	192.3%	1 hour	2 hours	8 hours	-
A3	28.5 %	274.0%	None	None	None	Embankment collapsed during centrifuge acceleration
A4	24.0 %	230.8%	None	None	None	Embankment collapsed during centrifuge acceleration
B1	21.0 %	201.9%	1 hour	3 hours	None	
B2	21.0 %	201.9%	1 hour	None	12 hours	
B3	22.0 %	211.5%	1 hour	3 hours	None	
B4	22.0 %	211.5%	1 hour	None	12 hours	
B5	23.0 %	221.2%	1 hour	3 hours	None	
B6	23.0 %	221.2%	1 hour	None	12 hours	

4 DATA ANALYSIS AND DISCUSSION OF RESULTS

This chapter discusses the tests conducted in the geotechnical centrifuge and compares the results to the slope stability analysis conducted in GeoStudio and the soil water characteristic curve. The material properties and characteristics obtained from the triaxial test, Mastersizer and soil water characteristic curve tests are presented and discussed and are compared to the specifications required for bulk earthworks.

4.1 MATERIAL PROPERTIES

The current specification for railway earthworks used in South Africa is the S410. Comparing the parameters of the material obtained from site to the parameters required by the S410 railway earthworks specification shows that the material is found lacking in some aspects. The comparison can be seen in Table 4.1. The plasticity index of the material is adequate for bulk earthworks. The CBR results of the two samples taken on site are well below the required value. This could be due to the significant amount of mica observed in the material. Tobey and Bulman (1964) showed that the content of mica in the soil significantly affects the engineering properties such as the plasticity index, compacted density and strength. Weinert (1980) also described micas as highly elastic minerals that influence the Atterberg limits, density and the ability to compact the material.

Table 4.1: Material parameter comparison to the S410 specifications for bulk earthworks

Property Description	Sample 1	Sample 2	S410
Plasticity Index (%)	17	17	25
CBR (Modified AASHTO) TMH1 A8			
% Swell	1.3	4.1	Max 2%
90%	1.7	0.8	Minimum strength after compaction (CBR) = 5
93%	1.9	0.8	
95%	2.1	0.9	
97%	2.2	1.2	
98%	2.3	1.3	
100%	2.4	1.6	

4.1.1 Particle Grading and Classification

The particle grading for the material used for all the tests conducted was analysed using the Mastersizer as discussed in Section 3.3.1. The D_{10}, D_{50} and D_{90} particle sizes that were calculated are:

- $D_{10} =$ 5.3 µm
- $D_{50} =$ 49.1 µm
- $D_{90} =$ 441.4 µm

The particle size distribution and sieve analysis obtained from the Mastersizer can be seen in Figure 4.1 and Figure 4.2 respectively. Figure 4.2 provides the particle size distribution from the samples obtained from site. It can be seen that there is a small percentage of clay in the material and a large amount of silt. The soil can be classified as a clayey sand (SC –Unified classification). The percentage soil particles and foreign matter greater than 2 mm sizes that were sieved out was small. Therefore, the behaviour of the soil in the centrifuge will still be dominated by the ruling soil matrix through which the stresses would be distributed. The results given by the Mastersizer confirms the results discussed in Section 3.3.1 where the average percentage clay, silt, sand and gravel is given as:

- Clay = 8.5 %
- Silt =28.0 %
- Sand = 57.0 %
- Gravel = 6.5 %

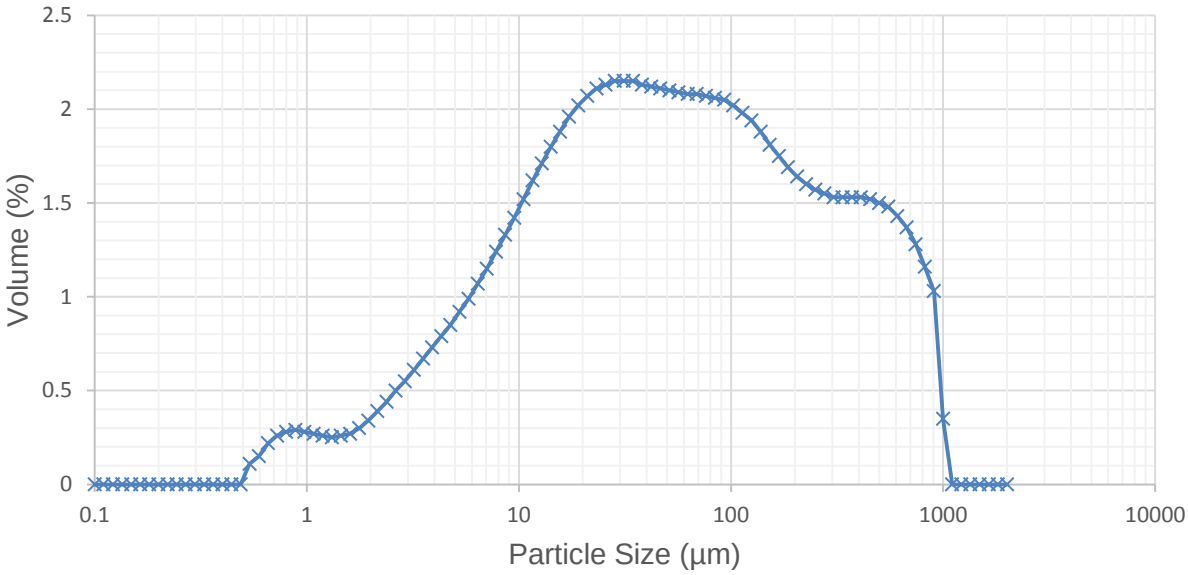

Figure 4.1: Particle size distribution as a volume percentage of the soil

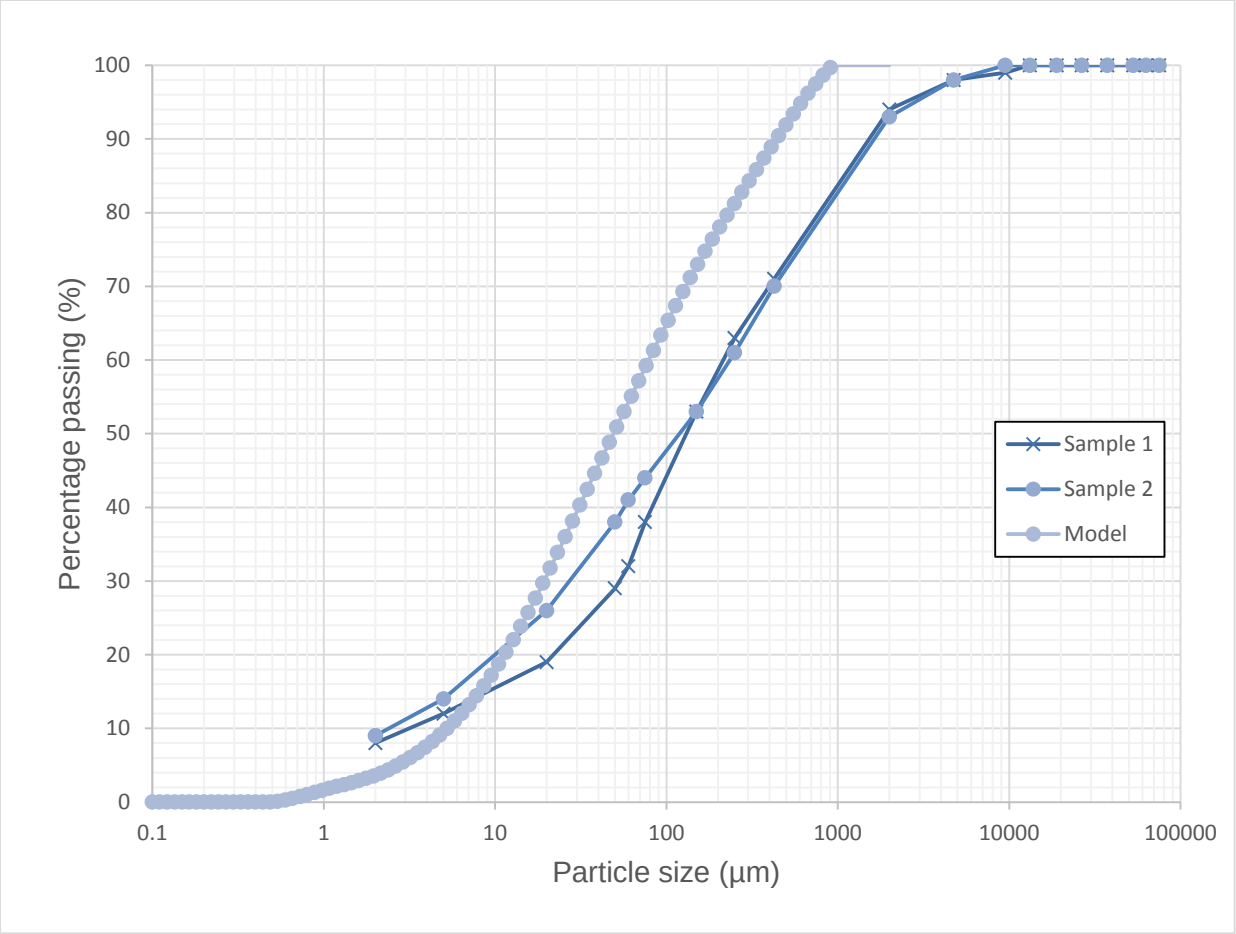

Figure 4.2: Sieve analysis of soil used in the tests from Mastersizer compared to site samples

4.1.2 Shear strength

Consolidated undrained triaxial tests were done to obtain the strength parameters of the material. Three samples were tested at effective stresses of 75 kPa, 150 kPa and 250 kPa respectively. These values were chosen using the density of the compacted material and the height of the embankment to approximate the maximum amount of stress anticipated in the embankment.

The triaxial samples had dimensions of approximately 50 mm diameter and 100 mm height. The samples were prepared at a moisture content of 22 % and a 90 % Modified AASHTO dry density of 1648 kg/m^3. The samples were compacted in five layers. A thin layer of petroleum jelly was applied to the inside of the moulds to assist with the demoulding process. One of the triaxial samples can be seen in Figure 4.3.

Due to the small particle sizes and possibility of a very low permeability of the soil, it was decided to use side drains for the three triaxial tests. The side drains and final triaxial setup can be seen in Figure 4.4 and Figure 4.5.

Figure 4.3: Triaxial sample

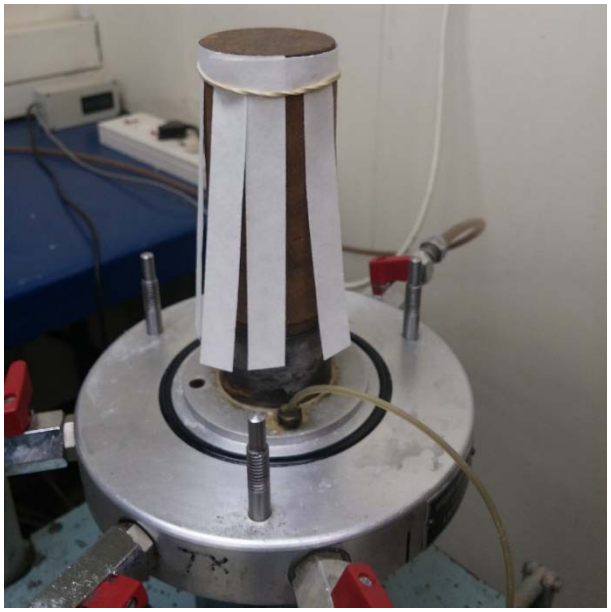

Figure 4.4: Side drains used for the triaxial tests

Figure 4.5: Final triaxial setup

The shear strength parameters (angle of friction (ϕ') and cohesion (c')) were obtained from the shear stage of the consolidated undrained test. The stress paths were drawn in t' - s' space which represents the maximum shear and normal effective stress values respectively. The critical state line or failure line is used to calculate the angle of friction and cohesion values. The stress paths calculated for the three triaxial samples can be seen in Figure 4.6. The failure envelope is drawn on the same graph. The friction angle and cohesion intercept obtained from this line was:

- $\phi' = 34°$
- $c' = 0\ kPa$

The stress paths for the three samples initially followed the drainage path gradient of 1 to 3, as indicated on Figure 4.6. The stress paths then moved away from the drained path indicating contractive behaviour, thereafter the stress paths indicate the material dilating and increasing in strength towards failure. The test at 250 kPa effective stress showed an unexpected turn in the stress path which could indicate a minor yield during the test. This could be as a result of minor slippage between soil particles.

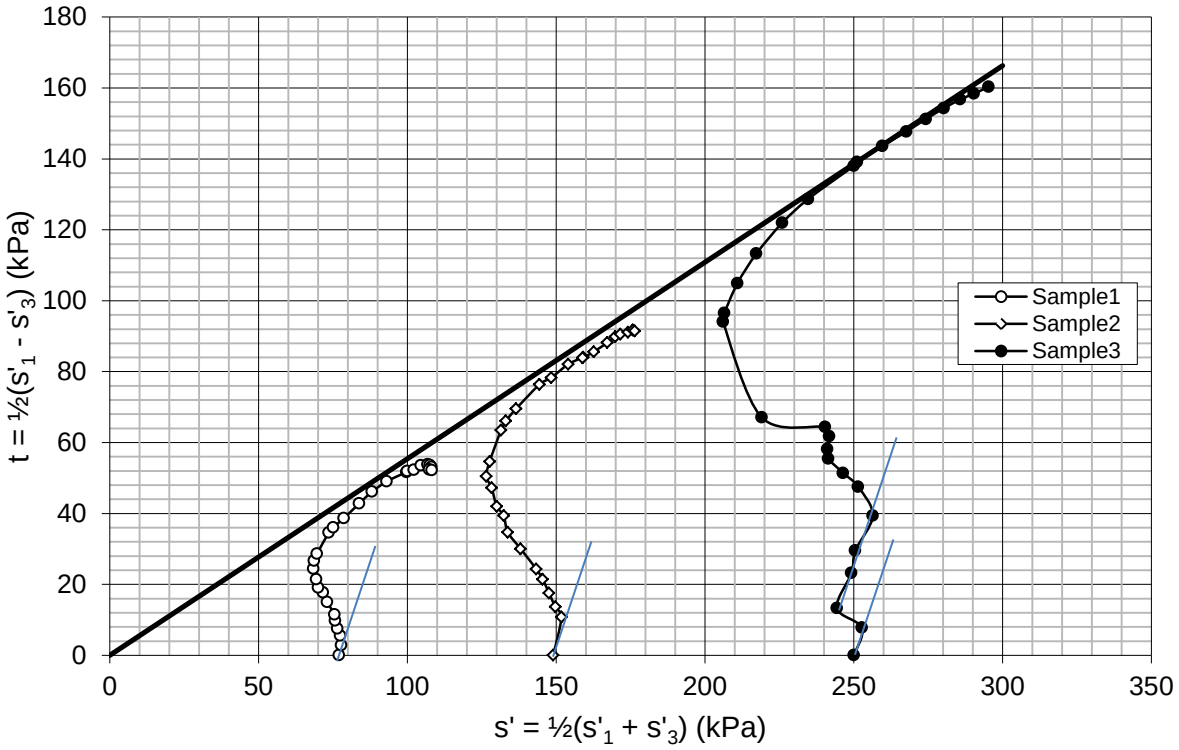

Figure 4.6: Stress paths for triaxial samples plotted in s-t space.

4.1.3 Soil Water Characteristic Curve

Drying tests were conducted on the material used for the centrifuge and triaxial tests to obtain the soil water characteristic curves. The graph of matric suction against gravimetric moisture content can be seen in Figure 4.7. Comparing the graph to the one in Figure 4.8 it can be seen that the turning point in matric suction in Figure 4.8 is at the point where a change in gradient can be seen in Figure 4.7. This point corresponds to a moisture content value of approximately 26 % and a degree of saturation of 93 % for this test. This can be identified as the air entry suction point. The bulk density of the material at this point is 1938 kg/m^3. The corresponding 90 % modified AASHTO bulk density at 93 % degree of saturation is 2009kg/m^3 with a moisture content of 22 %. This moisture content can therefore be taken as the starting point where there is a significant increase in suctions and therefore strength. The void ratio vs. gravimetric moisture content curve obtained from the same test is shown in Figure 4.9. Digital imaging was used to calculate the volume from which the void ratio was calculated for the sample. The minimum void ratio obtained was 75 %. This can be seen as the true shrinkage limit and the minimum volume the soil can attain during drying to zero water content.

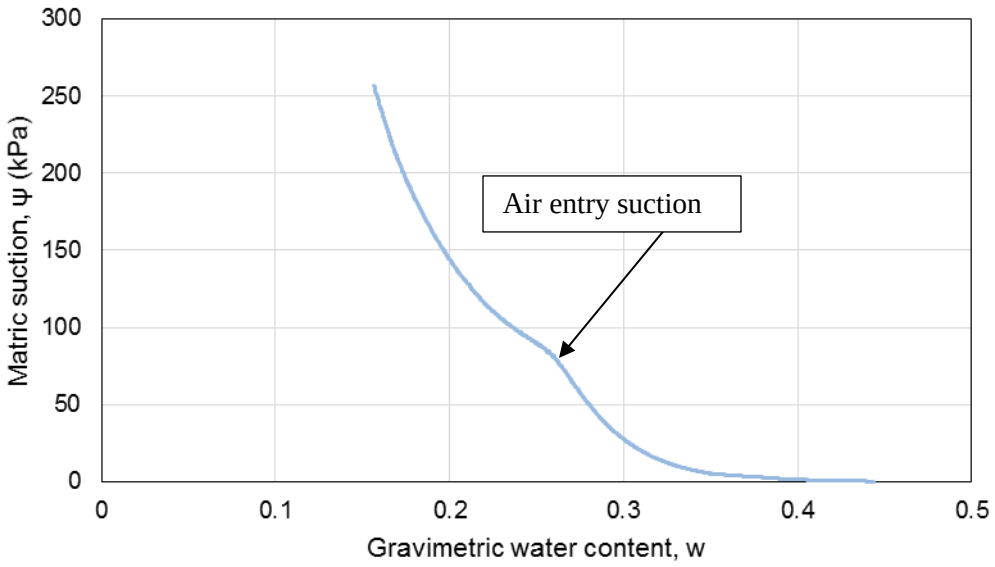

Figure 4.7: Matric suction vs. gravimetric water content

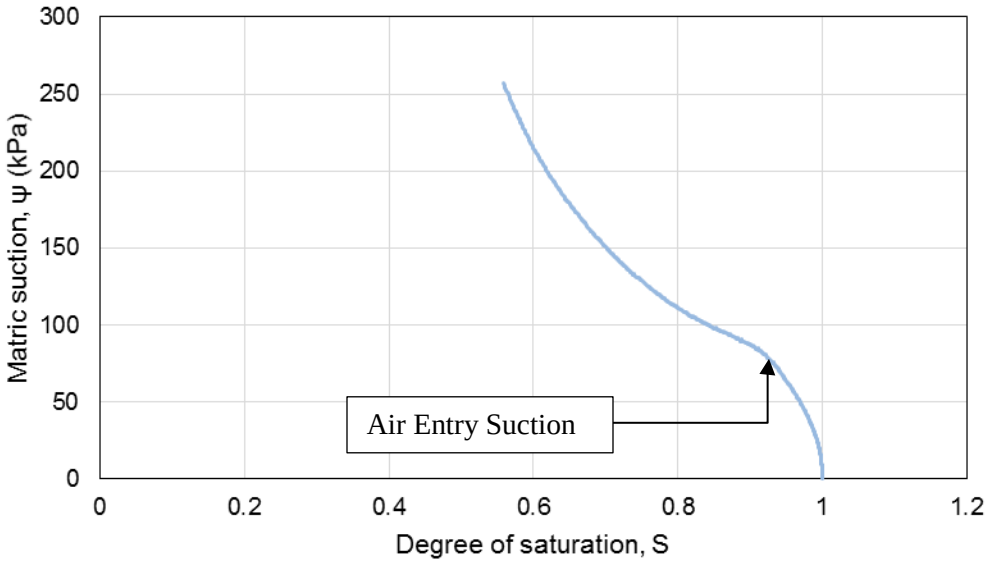

Figure 4.8: Matric Suction vs. degree of Saturation

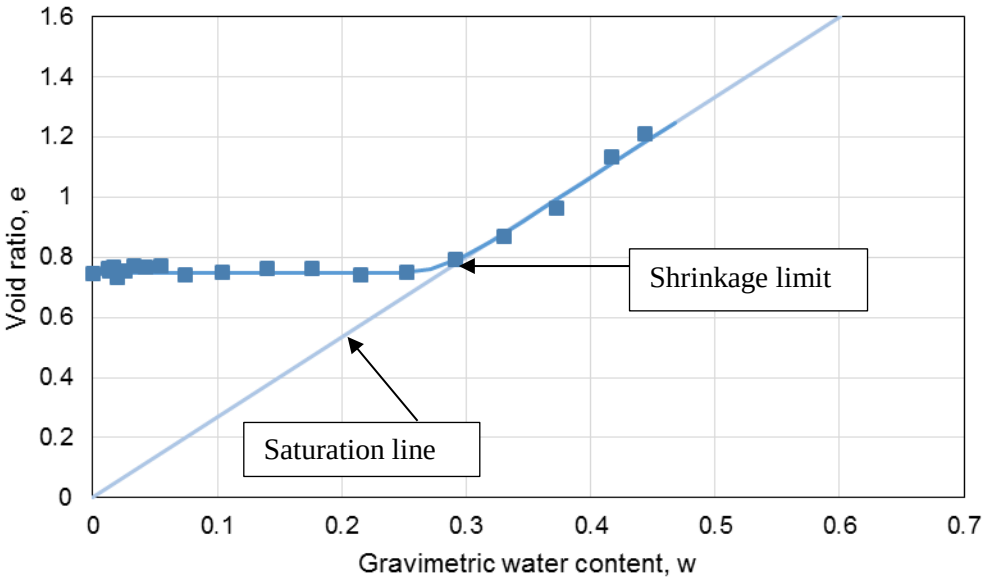

Figure 4.9: Void ratio vs. gravimetric water content

4.2 CENTRIFUGE TESTS

The tests conducted in the geotechnical centrifuge are summarised in Section 3.7. This section concentrates on the final six tests (B1 to B6). Tests A1 to A4 served as the iterative process to find the moisture content range between a stable and unstable embankment. The testing procedure and results for Tests A1 to A4 are given in Appendix A.

The embankment models prepared at optimum moisture content (10.4 % + 1 %) and 20 % moisture contents for Tests A1 and A2 respectively produced stable embankments. Tests A2 and A4 at 28 % and 24 % moisture contents produced embankments which collapsed under their own weight during the centrifuge acceleration period. As a result it was chosen to conduct the remainder of the centrifuge tests at 21 %, 22 % and 23 % moisture contents. Tests A1 to A4 provided the opportunity to rectify problems with the experimental setup and methodology.

Tests B1 to B6 are discussed in detail below, presenting the settlement data and visual results. Moisture content readings were taken at the end of the tests in order to show the effect of moisture loss during testing.

4.2.1 Test B1: Moisture content at 21.0% (Static Loading)

Test B1 was the first to be conducted using the updated loading methodology with a stabilisation period of 1 hour and a static loading period of 3 hours. Small amounts of white powder were added to the front of the embankment to add texture to the material for the PIV analysis (see Figure 4.10 showing the front of the embankment in the strongbox). No major collapse, slope failure planes or large settlements were observed during the test.

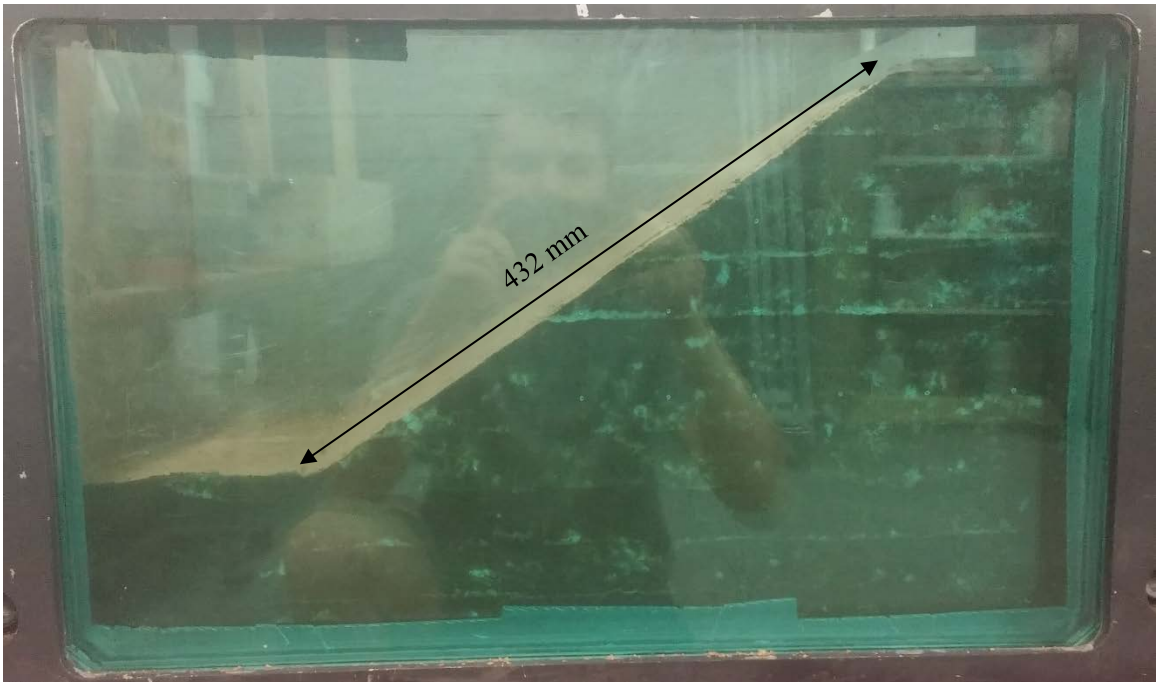

Figure 4.10: Front of embankment for Test B1 (21.0 % MC)

The visual observations at the end of the test showed significant cracking along the face of the embankment. The largest of the cracks ran vertically along the face of the embankment which can be seen in Figure 4.11. This is taken to be a shrinkage crack that formed due to drying of the material during the duration of the test. Smaller cracks that run horizontally along the face of the embankment are also visible in Figure 4.11. These cracks, together with a smaller crack visible in Figure 4.12 that runs along the length of the embankment on top, indicate that there might have been a minimal shift of material along the slope of the embankment. This is however not conclusive and dominant source of the cracks that formed could be shrinkage cracks as a result of the material drying.

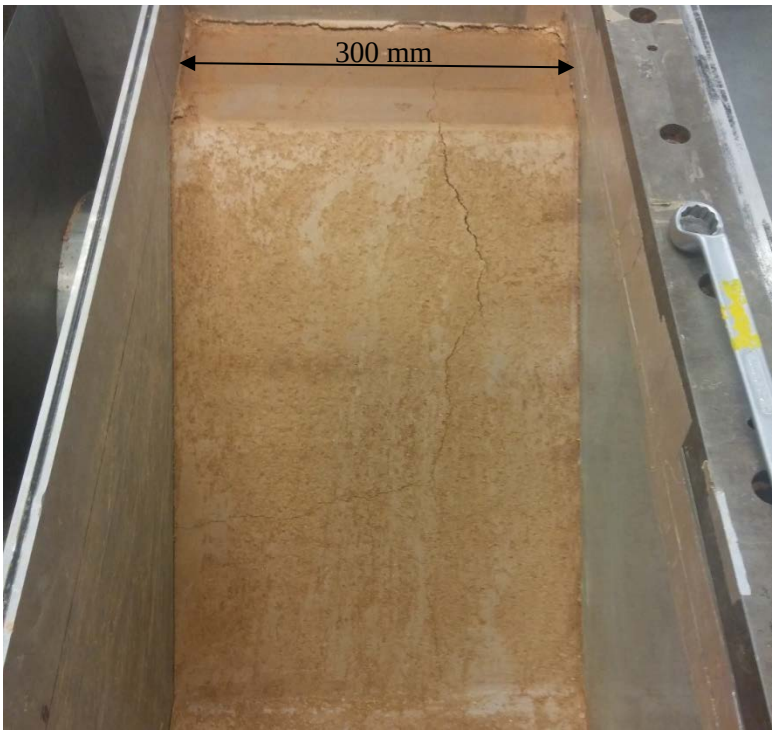

Figure 4.11: Cracks that formed during Test B1 (21.0 % MC)

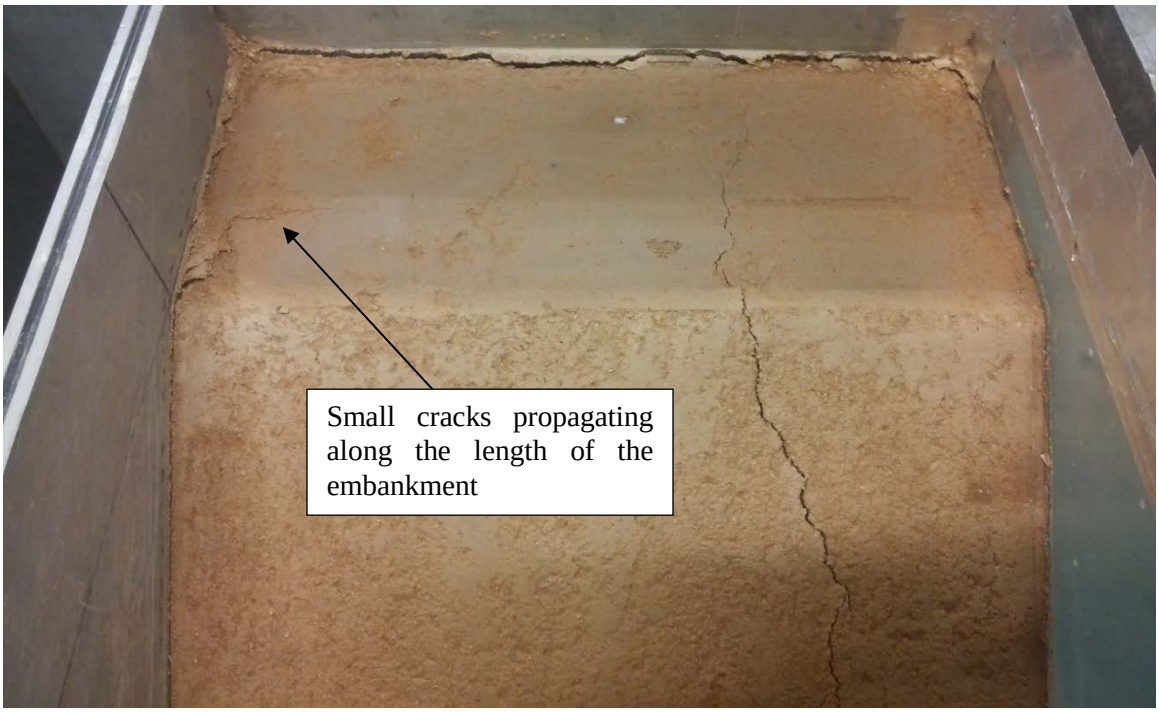

Figure 4.12: Smaller cracks along the length of the embankment during Test B1 (21.0 % MC)

4.2.2 Test B2: Moisture content at 21.0% (Cyclic Loading)

This test at 21.0 % moisture content consisted of a stabilisation period of 1 hour and cyclic loading period of 12 hours. During the compaction process some material moved in between the polycarbonate panel and the glass window of the strongbox which obstructed the view of the embankment. The particles between the panel and glass window moved during the test which prevented the PIV analysis. The movement of these particles can be seen in Figure 4.13.

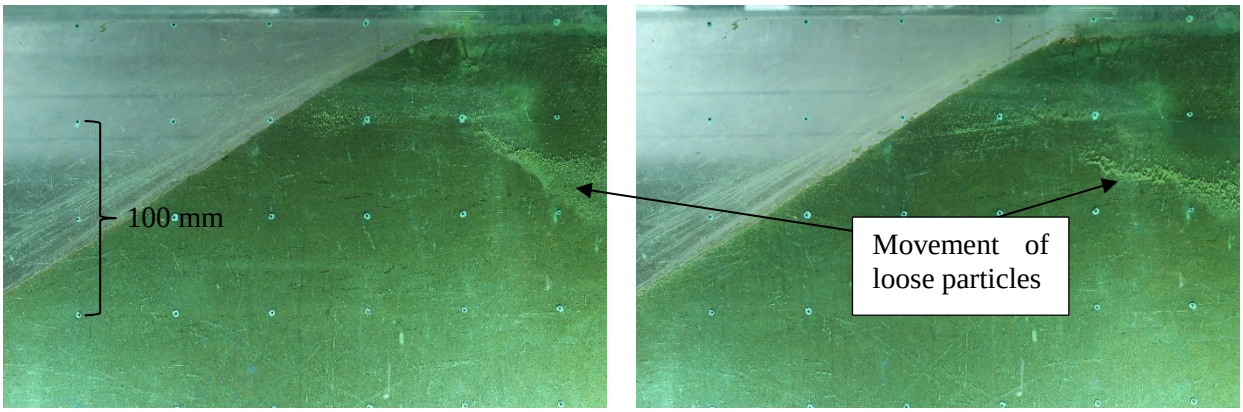

Figure 4.13: Movement of loose particles between polycarbonate panel and glass window for Test B2 (21.0 % MC)

No cracks of the embankment were observed through the front of the strongbox. However, there was a crack that formed vertically down the face of the embankment model throughout the test. The crack was observed from the top to the bottom of the embankment model as shown in Figure 4.14. This was once again an irregular crack regarding slope failures and hence points towards it being a shrinkage crack due to the drying of the material during the test. This is likely as this test was scheduled to run for close to 14 hours in the centrifuge. The duration of the test was extended due to problems encountered during the test where the centrifuge had to be stopped and started twice.

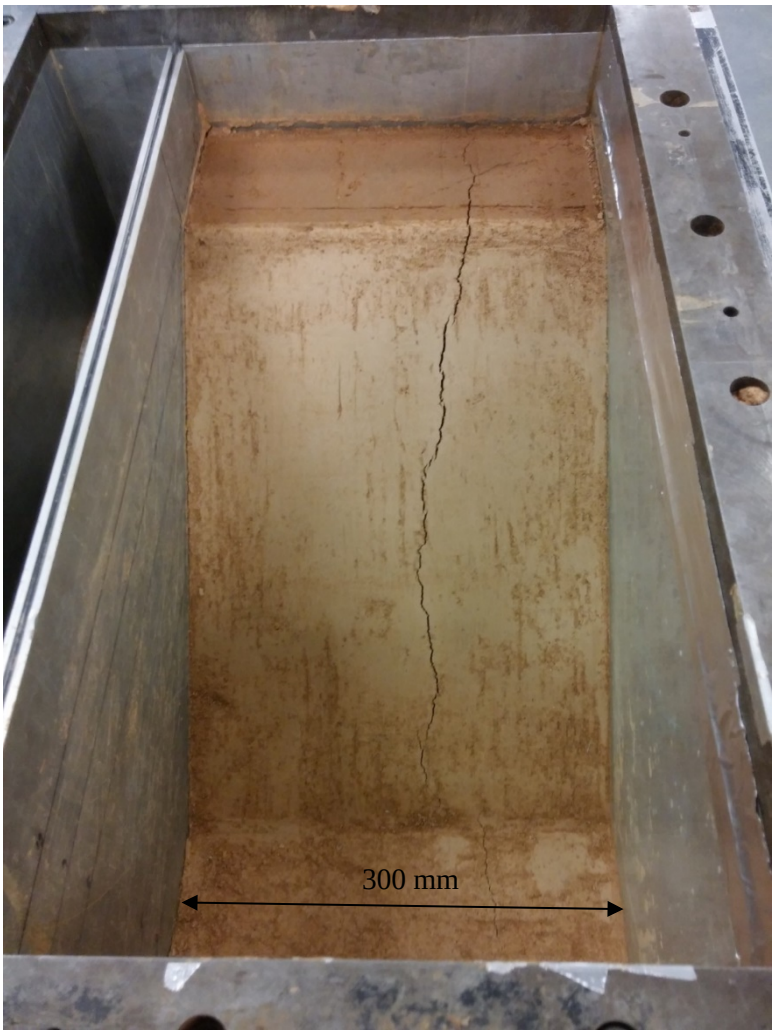

Figure 4.14: Cracks that formed during Test B2 (21.0 % MC)

4.2.3 Test B3: Moisture content at 22.0% (Static Loading)

This test at 22% moisture content comprised of a stabilisation period of 1 hour and static loading period of 3 hours. Figure 4.15 shows the embankment at the start of the test and Figure 4.16 shows the embankment with the cracks that formed during the test.

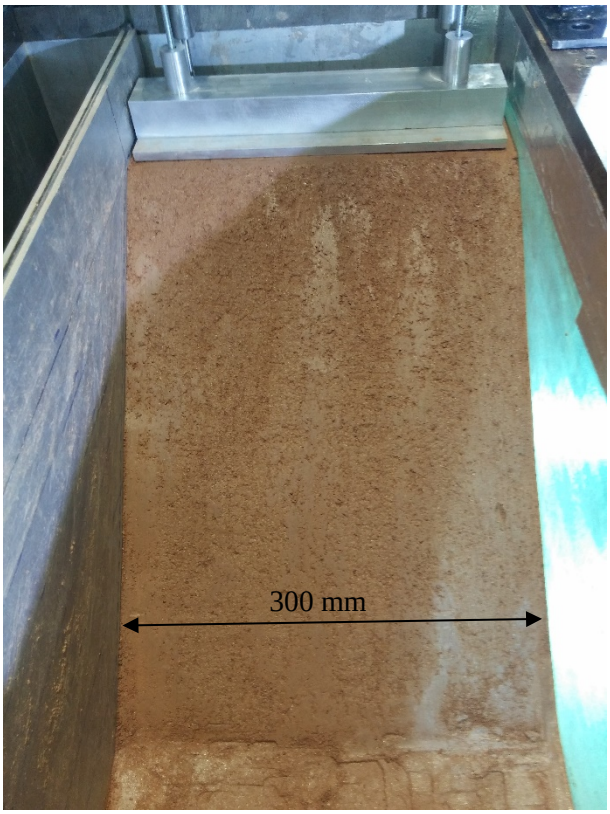

Figure 4.15: Embankment face at the start of Test B3

Figure 4.16: Cracks formed during Test B3.

A large crack was visible across the face of the embankment. There were small cracks visible at the top of the embankment which, in conjunction with the large crack across the face of the embankment, might indicate a shift of material along the side of the embankment. These small cracks are shown in Figure 4.17. There was, however, no major embankment collapse or cracks visible during the test through the strongbox window. Once the test stopped and the centrifuge had decelerated to 1g, a crack, as a result from material uplift, started forming which was visible through the strongbox window. This crack connected to the large horizontal crack across the face of the embankment. This substantiates the statement that a shift in material along the embankment face occurred. The crack that formed once the test stopped can be seen in Figure 4.18. A photo taken during the test is shown in Figure 4.19 to show the position of a small line where the crack had formed.

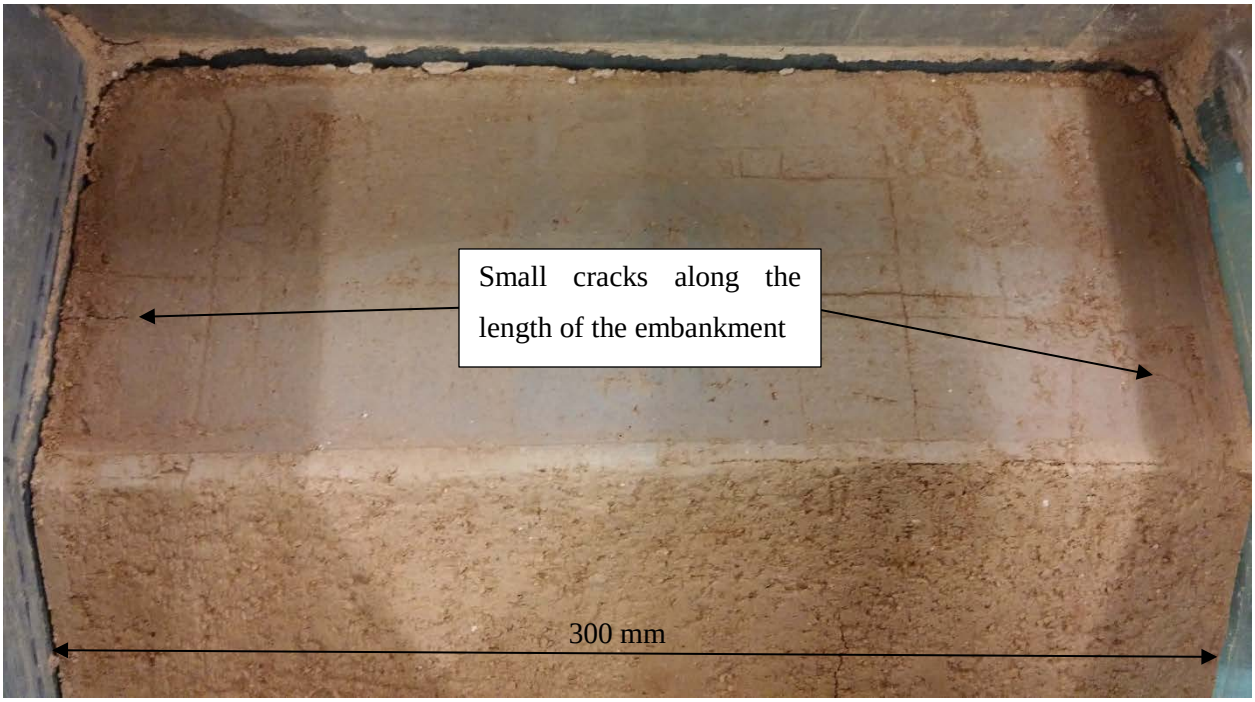

Figure 4.17: Small cracks that formed at the top of the embankment during Test B3 (22.0 % MC)

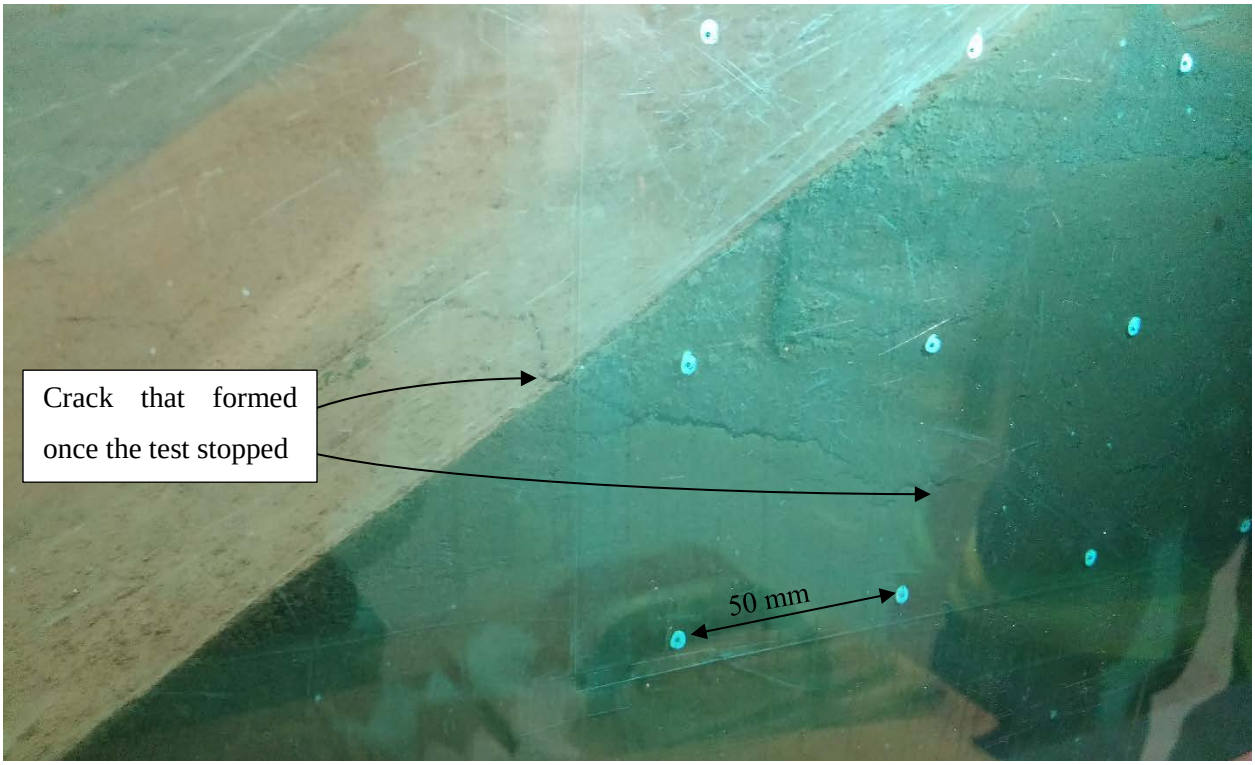

Figure 4.18: Crack that formed at the end of Test B3 (22.0 % MC)

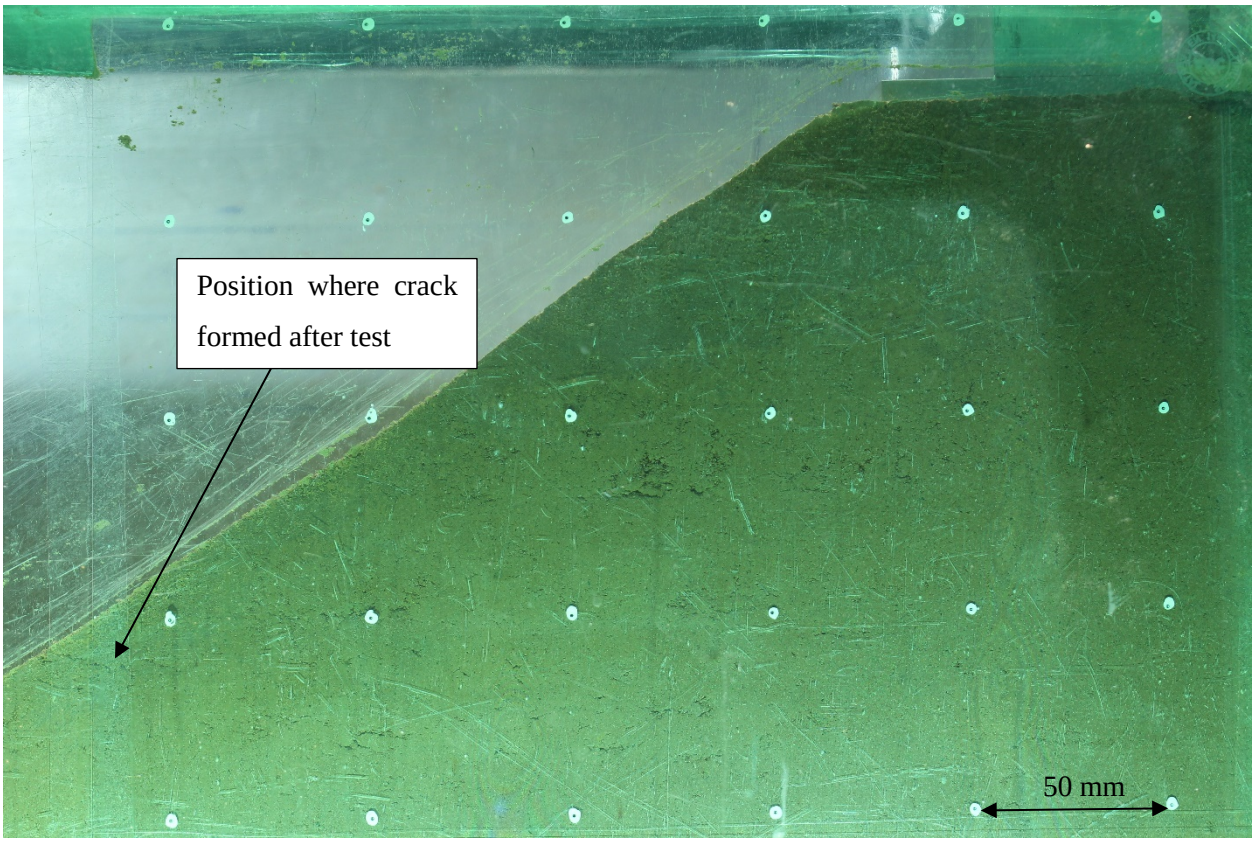

Figure 4.19: Photo taken during Test B3 to show where crack formed at the end of the test

4.2.4 Test B4: Moisture content at 22.0% (Cyclic Loading)

This test at 22% moisture content consisted of a stabilisation period of 1 hour and cyclic loading period of 12 hours. During the test a crack propagated inward from the face of the embankment towards the centre of the embankment. The propagating sequence can be seen in Figure 4.20. The dot spacing in Figure 4.20 is 50 mm.

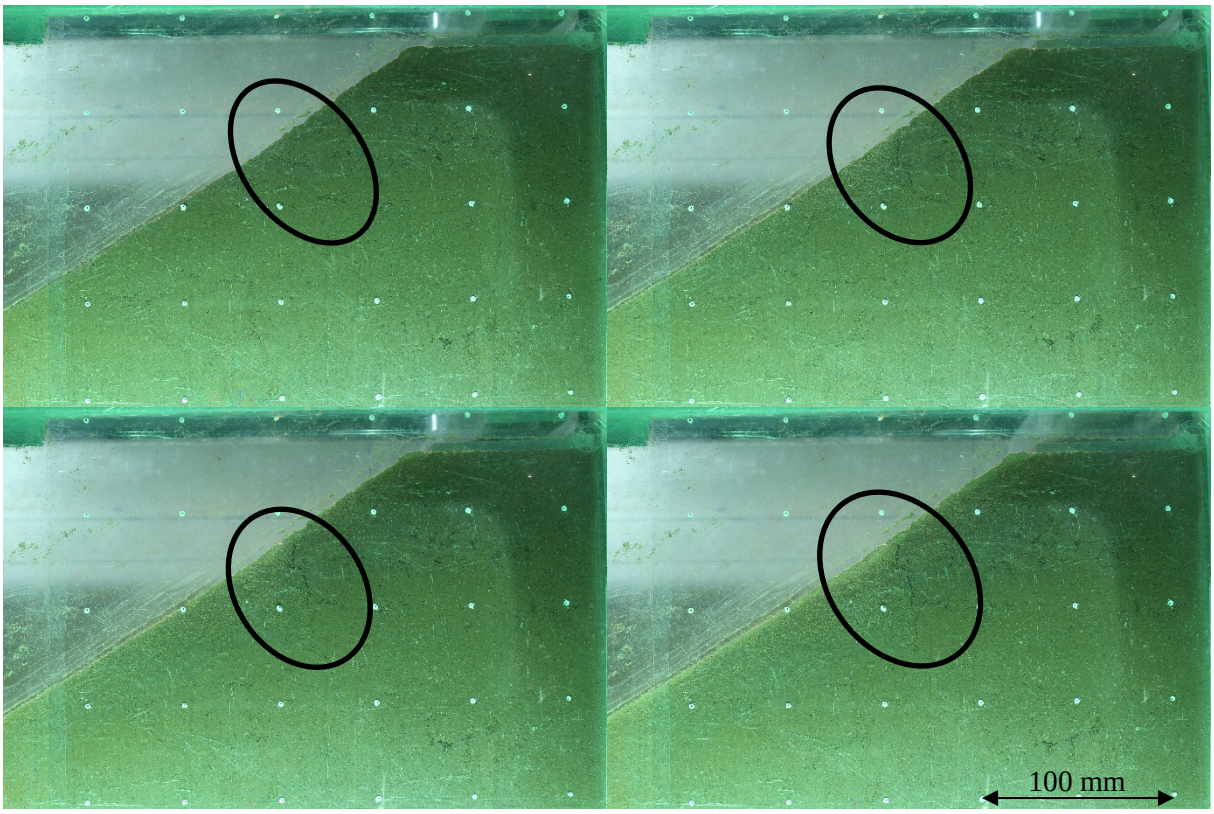

Figure 4.20: Propagation of the crack during Test B4 (22.0 % MC)

After the test was completed, the visual analysis showed that the crack that was visible through the strongbox window connected to the top of the embankment. There was an indication of a small crack on the further side of the embankment towards which this large crack points to. Taking into account the depth of the crack visible through the strongbox window, it suggests a significant amount of material shifted downward along the embankment slope. The cracks can be seen in Figure 4.21 . The photo in Figure 4.22 shows the connection of the front crack to the cracks visible from the top view of the embankment.

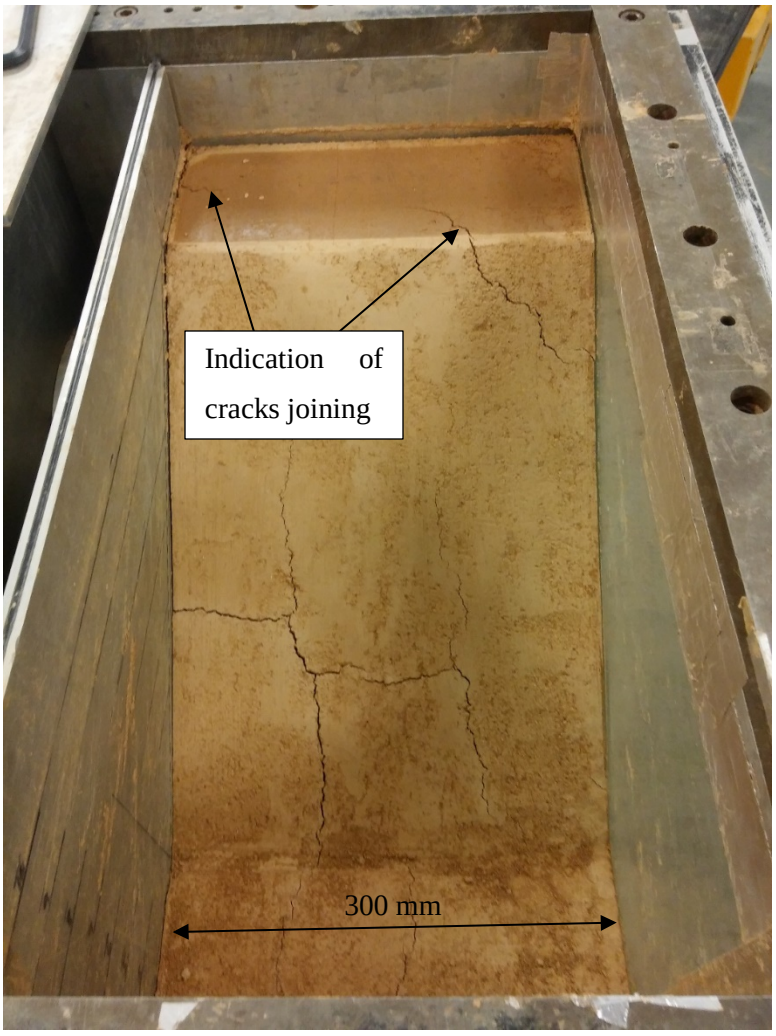

Figure 4.21: Top view of the cracks that formed during Test B4 (22.0 % MC)

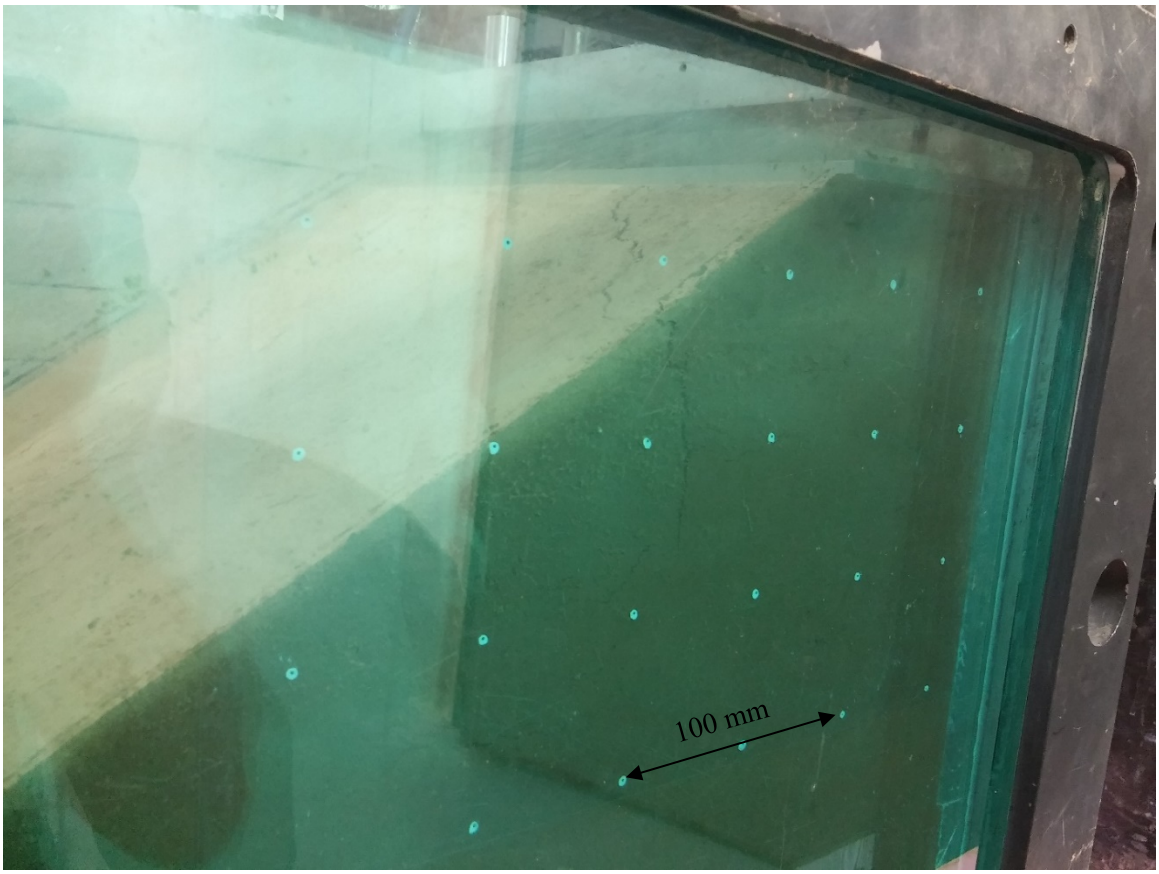

Figure 4.22: Front crack that moved to the top of the embankment with Test B4 (22.0 % MC)

4.2.5 Test B5: Moisture content at 23.0% (Static Loading)

This 23 % moisture content test consisted of a stabilisation period of 1 hour and static loading period of 3 hours. The cracks that formed during this test were similar to the cracks from both 22 % moisture content tests as shown in Figure 4.23. Figure 4.23 shows another crack that only became visible after the test had stopped and the acceleration decreased to 1 g. It is also visible from Figure 4.24 that the crack connects the major cracks shown in Figure 4.44. There is a large crack that runs horizontally along the face of the embankment and another that propagates to the top of the embankment. These two cracks are joined by the crack visible through the strongbox window which therefore indicate the formation and movement of a large wedge of material.

Figure 4.23: Cracks that formed during Test B5 (23.0 % MC)

Figure 4.24: Crack which expanded at the end of Test B5 (23.0 % MC)

In Figure 4.24 and Figure 4.25 there is a clear indication of upward lift along the crack across the face of the embankment. This could be as a result of a small amount of slippage of the large wedge down the embankment side which pushed it up along a slip plane.

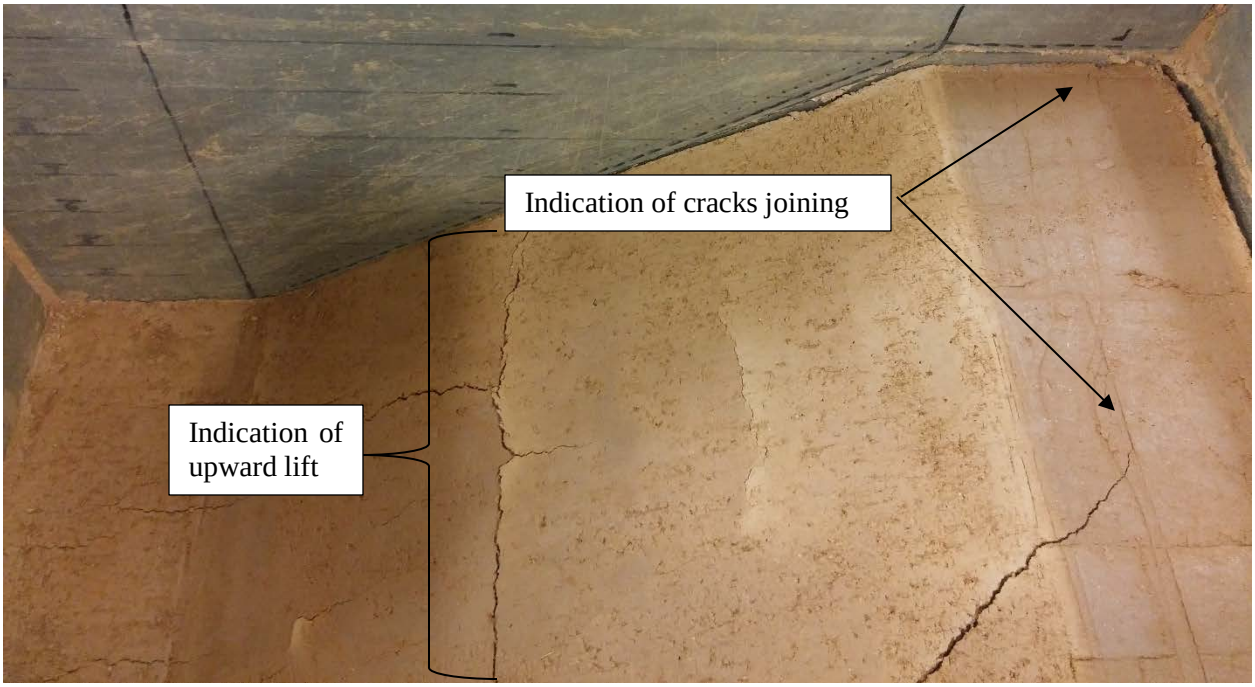

Figure 4.25: Indication of cracks created during Test B5 (23.0 % MC) joining at the top of the embankment

4.2.6 Test B6: Moisture content at 23.0 % (Cyclic Loading)

This test at 23 % moisture content consisted of a stabilisation period of 1 hour and cyclic loading period of 12 hours. The visual results from this test was once again similar to the tests conducted at 22% moisture content and the other test at 23% moisture content. A photo of the embankment before testing can be seen in Figure 4.26.

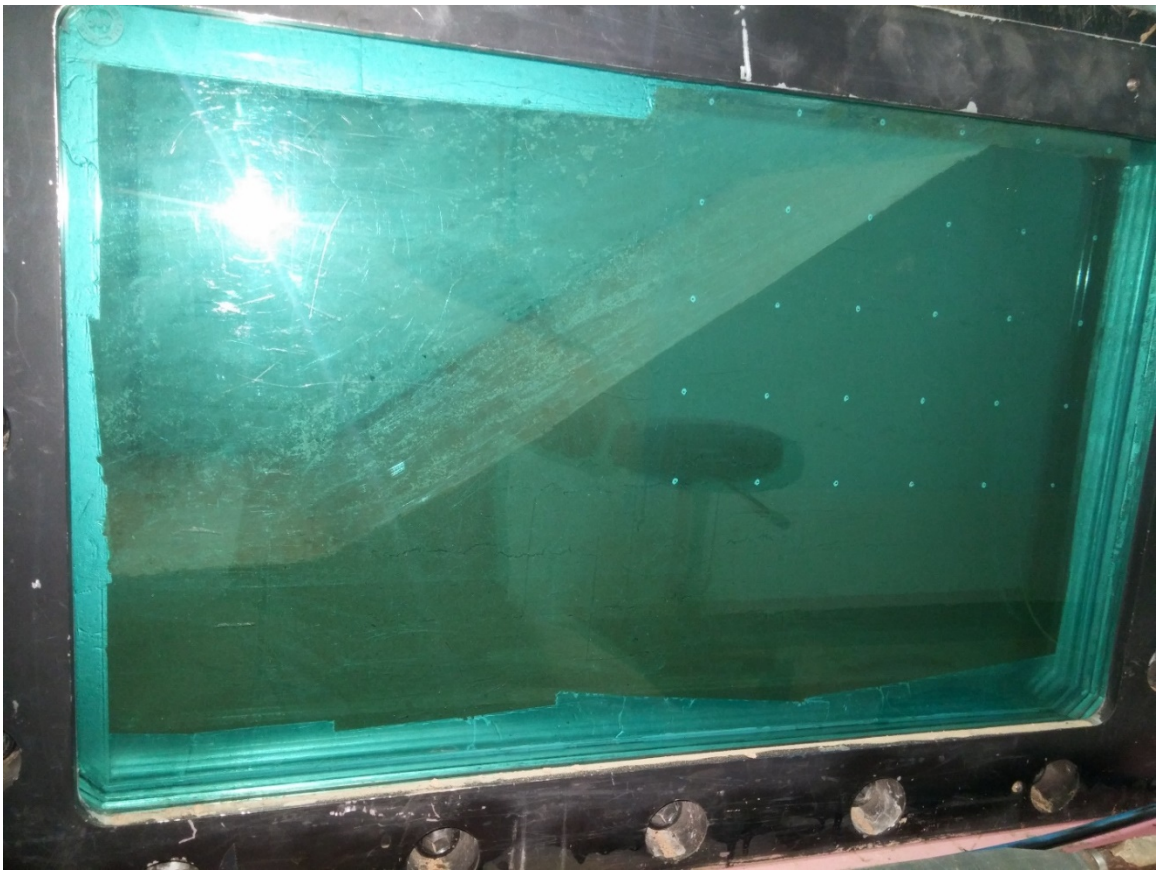

Figure 4.26: Embankment model for Test B6 (23.0 % MC)

A large crack formed during the test which was visible through the strongbox window. The final image of the test can be seen in Figure 4.27. A sequence of photos showing the crack propagation is shown in Figure 4.28. This crack was seen joining to a row of cracks across the length of the embankment shown in Figure 4.29.

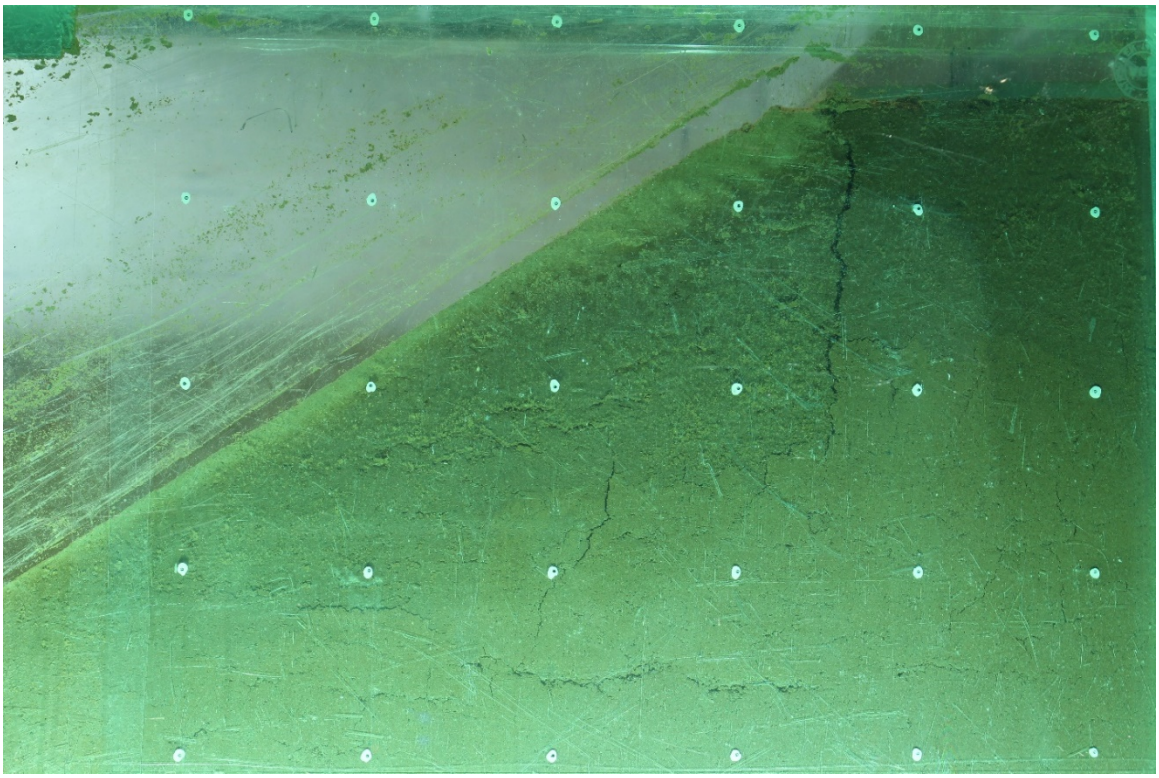

Figure 4.27: Final image of test showing a large crack that formed during Test B6 (23.0 % MC)

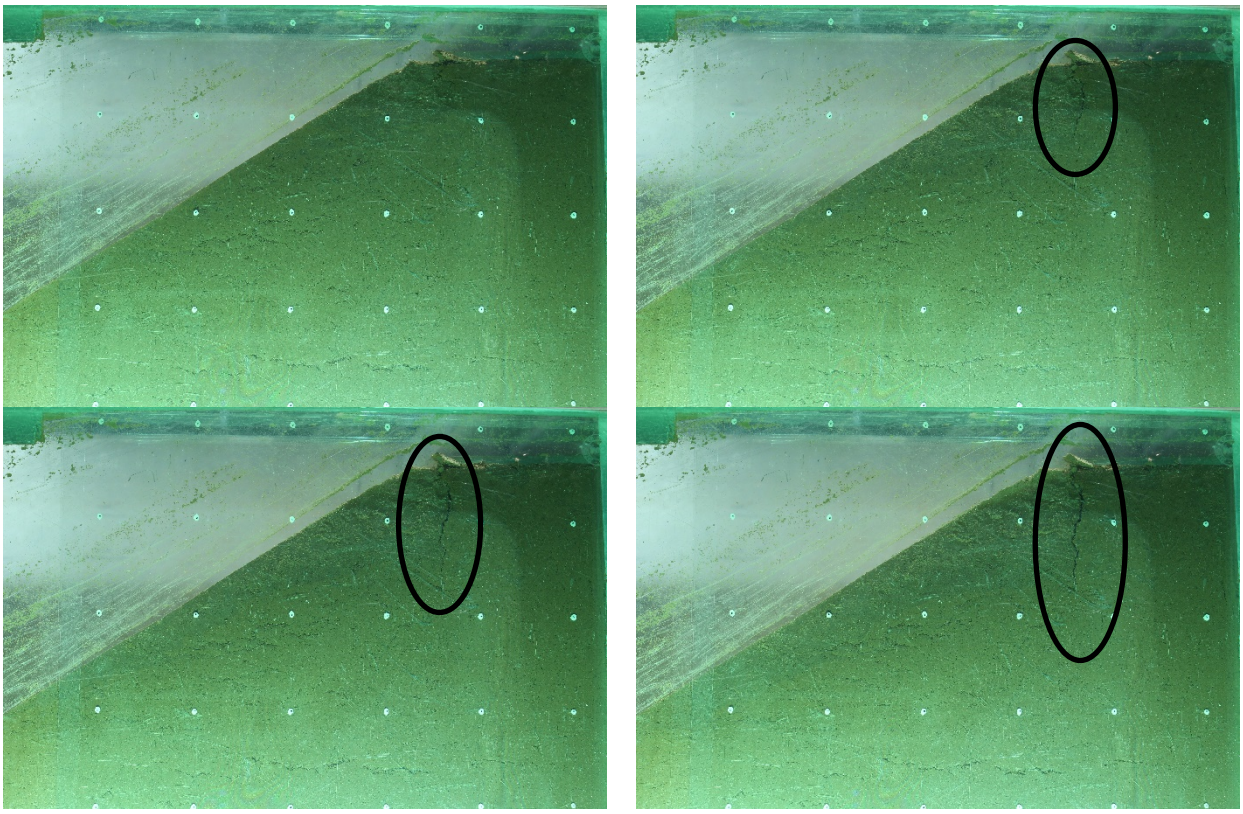

Figure 4.28: Image sequence showing crack propagation during Test B6 (23.0 % MC)

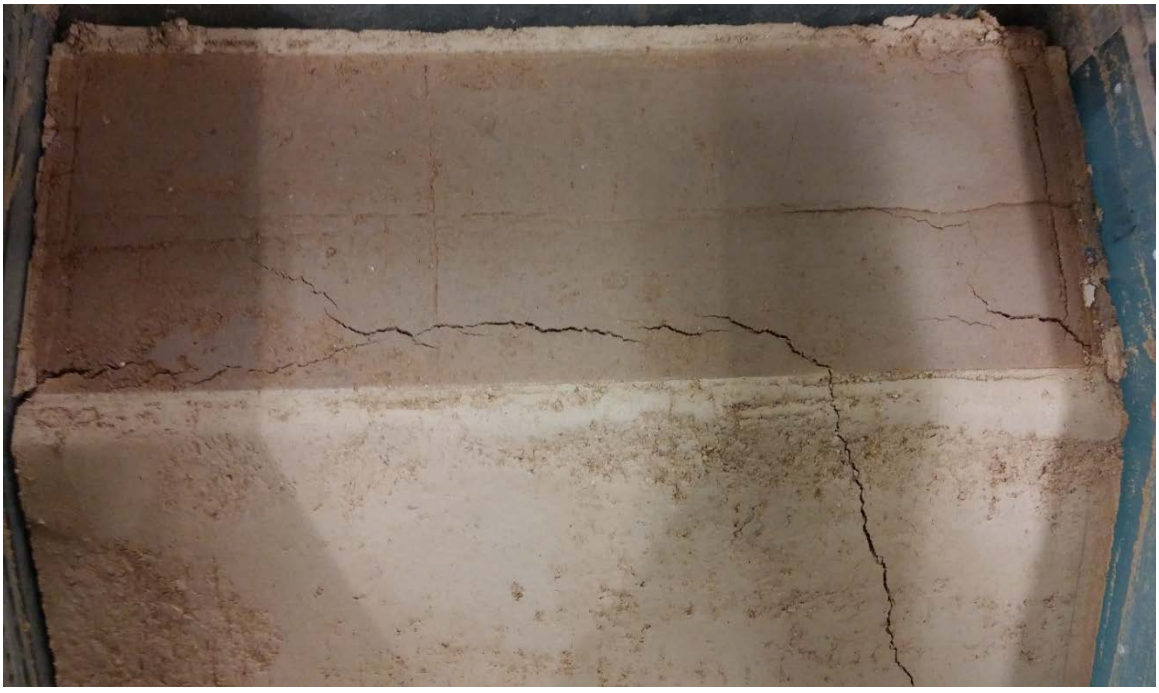

Figure 4.29: Cracks across the top length of the embankment formed during Test B6 (23.0 % MC)

The cracks that formed on the face of the embankment can be seen in Figure 4.30. A close-up of the horizontal crack in this photo shows material movement over the crack as shown in Figure 4.31. This once again indicates a minor slippage along a failure plane in the embankment. Numerous shrinkage cracks are also visible on the face of the embankment.

Figure 4.30: Cracks that formed on the face of the embankment with Test B6 (23.0 % MC)

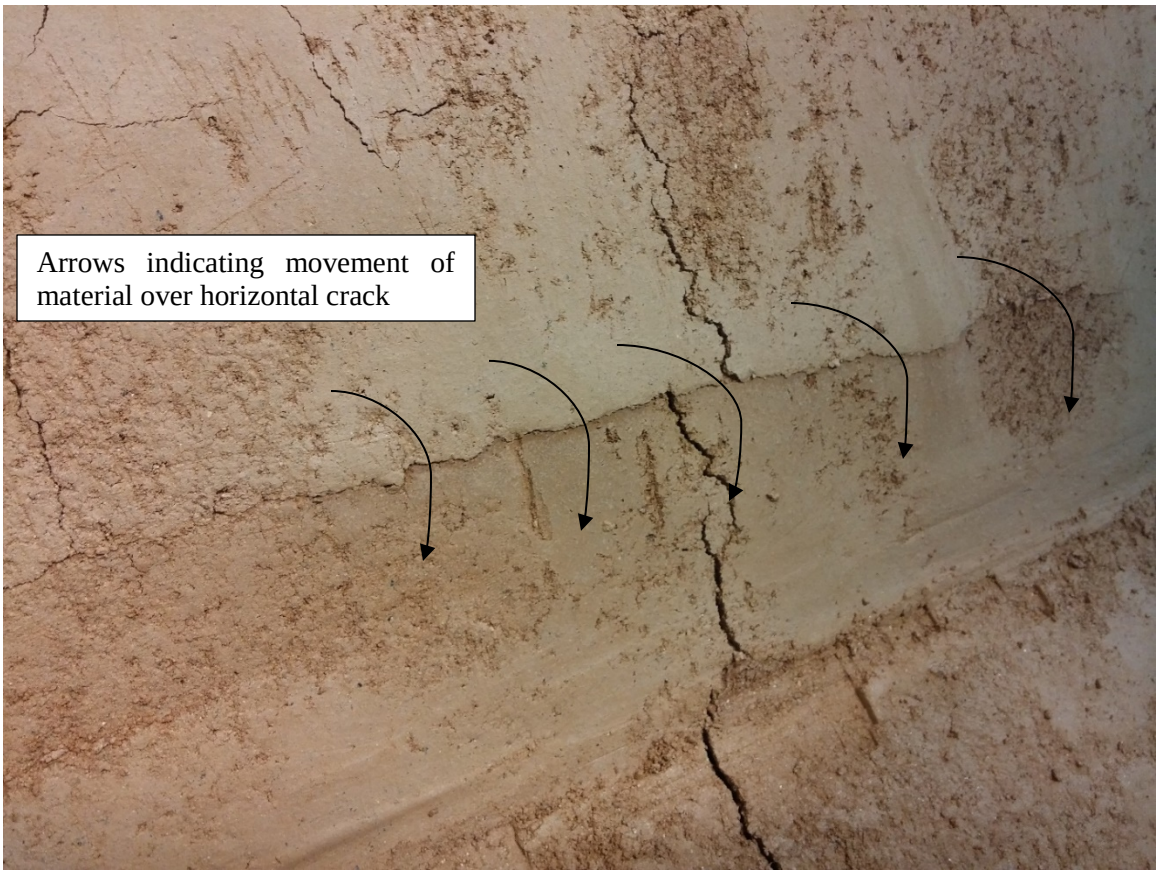

Figure 4.31: Movement of material over crack seen with Test B6 (23.0 % MC)

4.2.7 Settlement Results

Power function trendlines were applied to the settlement data from the LVDTs to define the settlement curves. The power function equation is shown below (Selig and Waters 1994):

$$S_N = S_1(N_L)^b \qquad \textbf{Eq. 4.1}$$

Where:

S_N = Settlement after N load cycles

S_1 =Settlement from first load cycle

N_L = Load cycles

b = Exponent

In this case the cycles are represented by the amount of time the loading was applied.

The settlement curves from the LVDT data of Test B1 to B6 are shown in Figure 4.32 to Figure 4.37 respectively. The settlement curves are the average between the readings obtained from the two LVDTs installed. The power function trend lines for the settlement curves are indicated in Figure 4.32 to Figure 4.37 . The LVDT data for test B2 was reworked to remove the stopping and acceleration readings when the test had to be stopped. This is evident in the slope changes visible on the settlement curve shown in Figure 4.33. The goodness of fit for the power function for Test B2 is therefore at a low quality. The power function however did not provide an exact match for the settlement curves. It only served as an indicative trend line. The comparisons between the settlement curves are shown in Section 4.4.

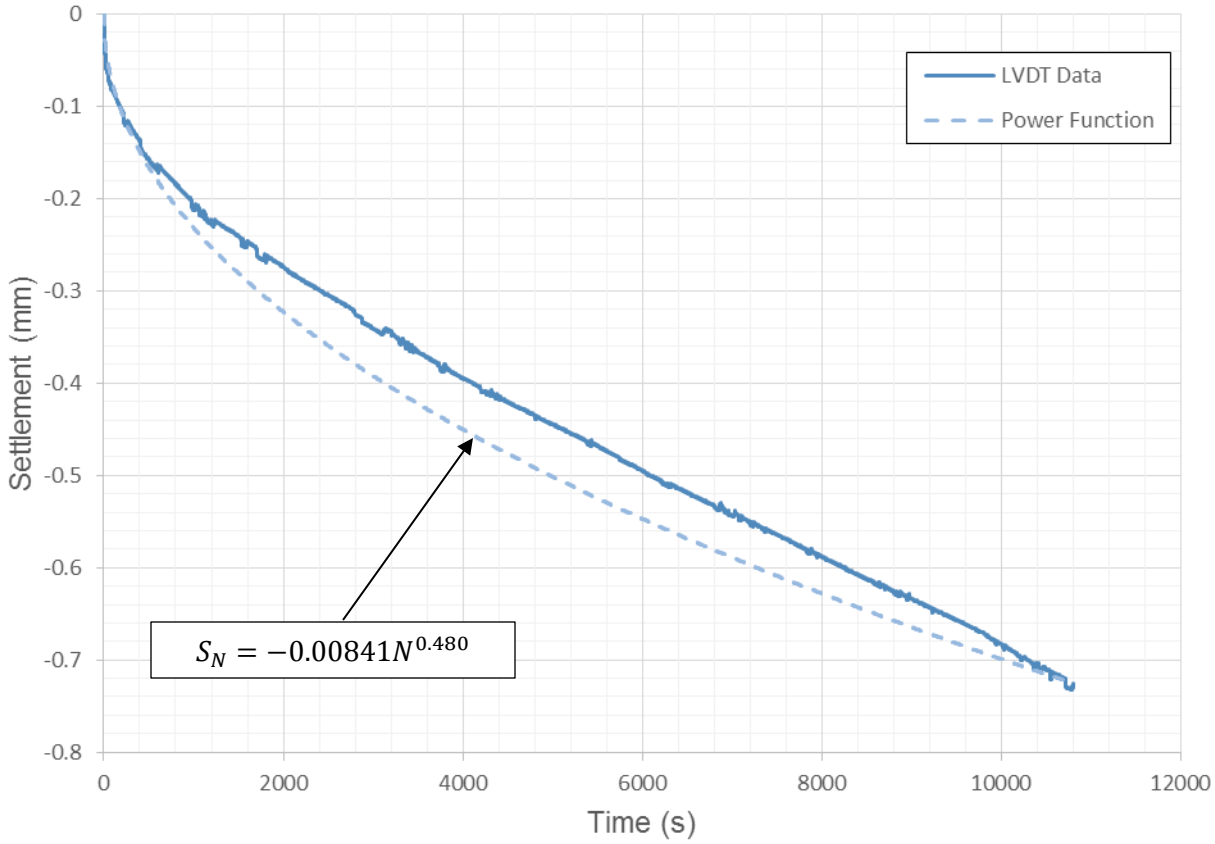

Figure 4.32: Settlement data for loading of Test B1 (21.0 % MC)

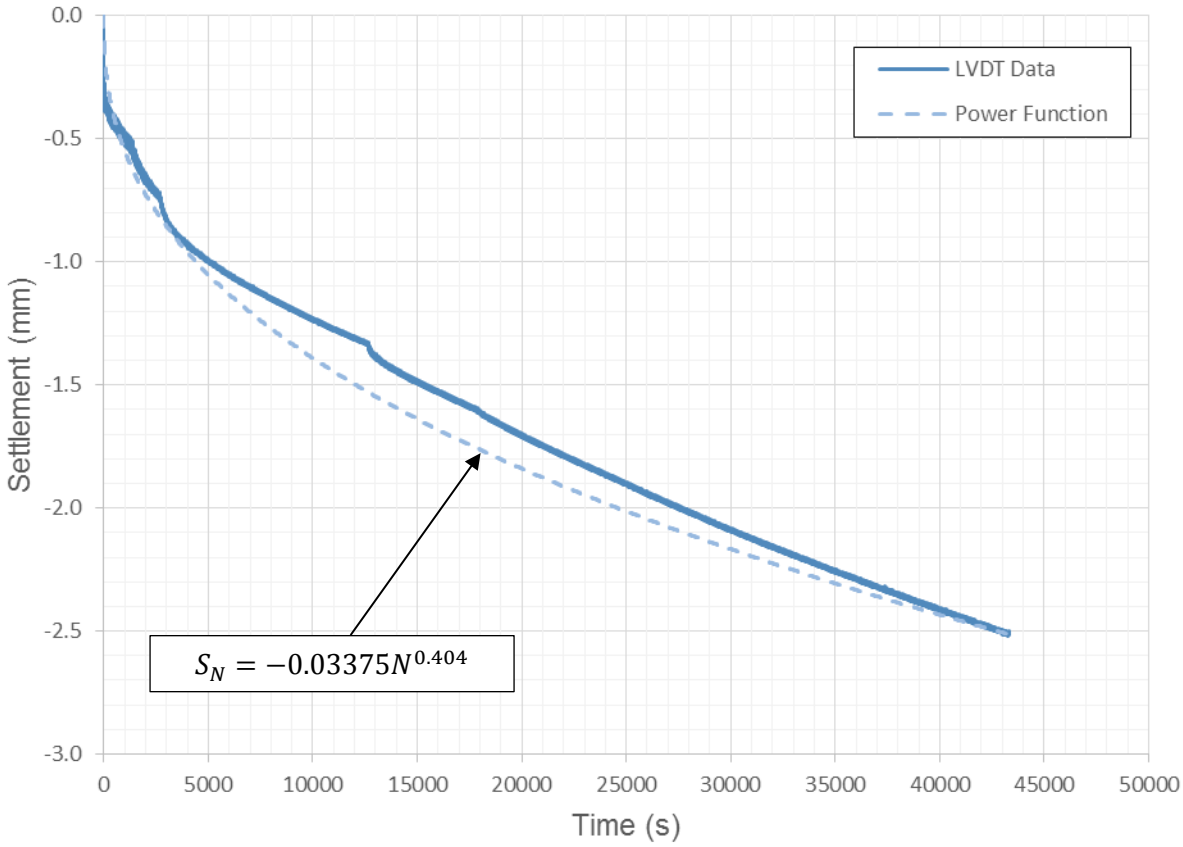

Figure 4.33: Loading settlement for Test B2 (21.0 % MC)

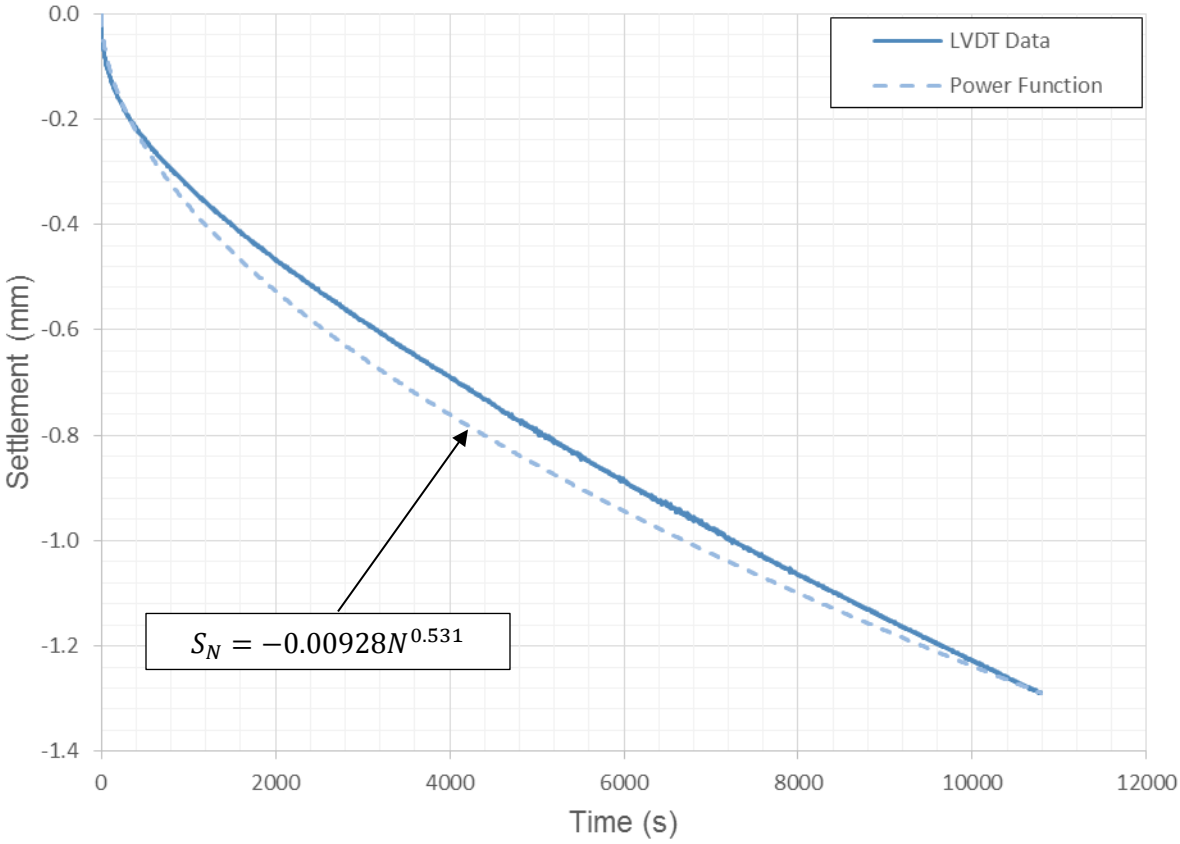

Figure 4.34: Settlement curve during loading in Test B3 (22.0 % MC)

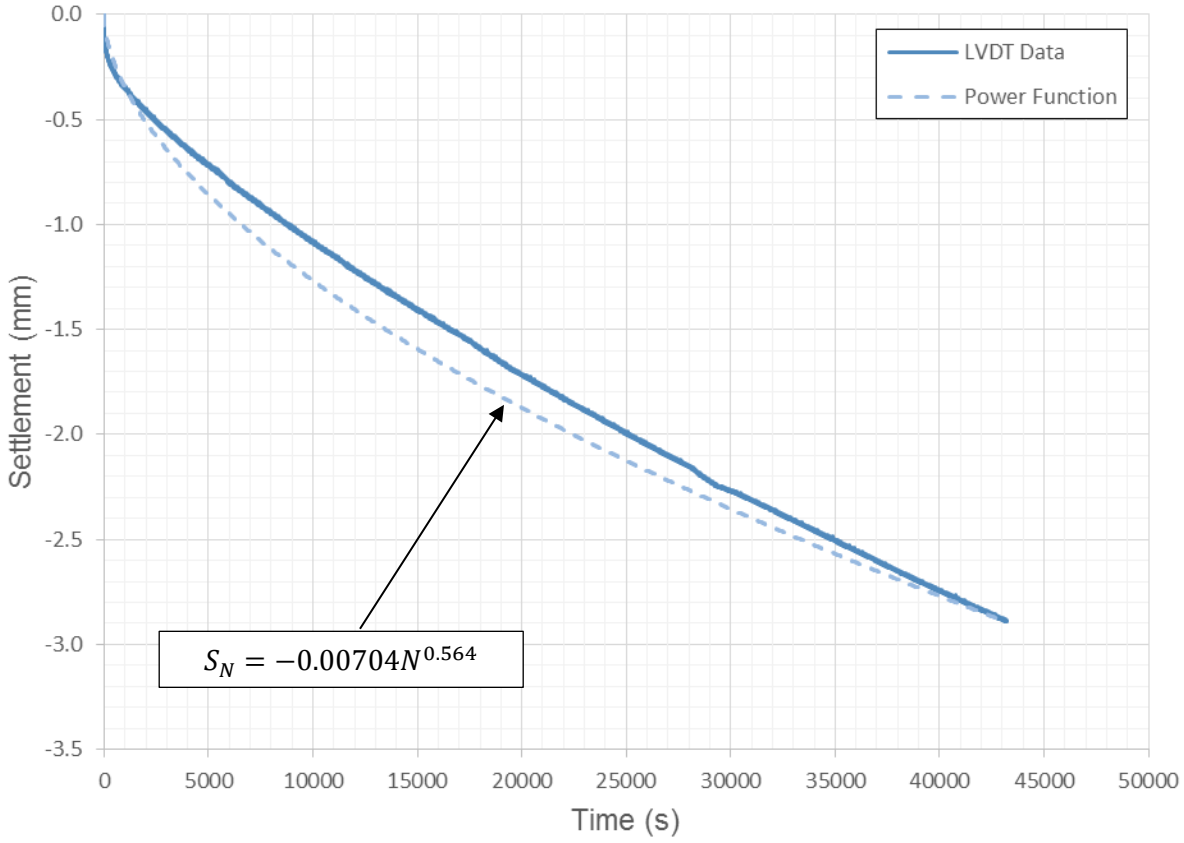

Figure 4.35: Settlement curve during the loading period for Test B4 (22.0% MC)

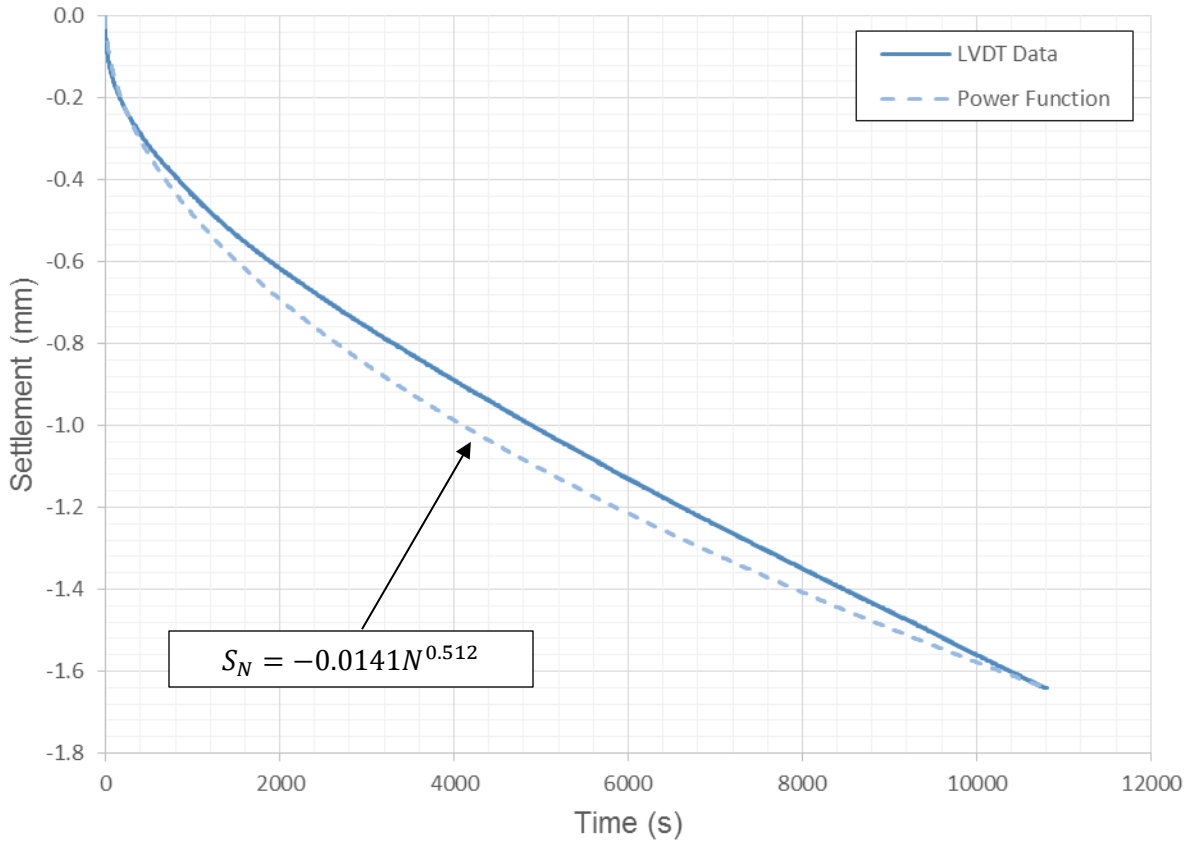

Figure 4.36: Settlement curve during the loading period for Test B5 (23.0 % MC)

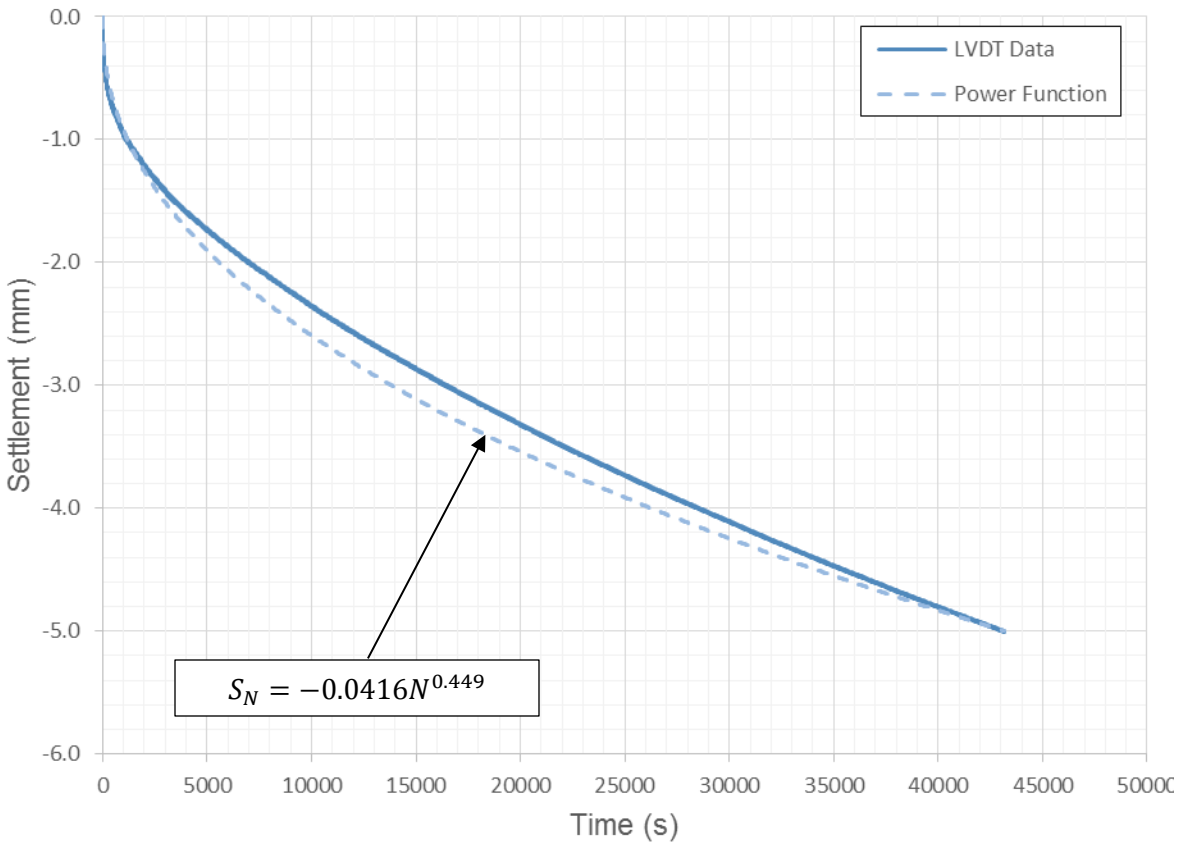

Figure 4.37: Settlement curve during loading period for Test B6 (23.0 % MC)

4.2.8 Moisture Readings

Moisture samples were taken at the end of Tests B1 to B6 in order to measure by what amount the material in the embankment model had dried out. The moisture contents were measured at certain positions in the embankment. The measured moisture contents are given in Table 4.2 and displayed in Figure 4.38. From the figure it is evident that the top of the embankment dried out significantly during the test. The moisture content readings showed that, with exception of the model surface, approximately 1 % to 2 % on average of the initial moisture was lost during model construction and testing. The drying of the material contributed to an increase in strength of the embankment as a result of an expected increase in suctions in the material. This was a contributing factor in the stability of the embankment models which showed no major slope failure. The static loading tests dried out significantly less than the cyclic loading tests as a result of the shorter time period for the static loading compared to the cyclic loading. Figure 4.39 shows the moisture content as a percentage of the optimum moisture content to be used as a reference.

Table 4.2: Moisture contents measured from samples after Test B1 to Test B6

Position in embankment	Test B1 Static Loading (MC 21%)	Test B2 Cyclic Loading (MC 21%)	Test B3 Static Loading (MC 22%)	Test B4 Cyclic Loading (MC 22%)	Test B5 Static Loading (MC 23%)	Test B6 Cyclic Loading (MC 23%)
Top	11.9%	9.3%	13.9%	11.3%	13.7%	9.6%
50 - 100 mm	19.1%	18.3%	20.7%	18.9%	20.3%	18.8%
100 - 150 mm	19.0%	20.0%	21.0%	20.7%	21.5%	20.6%
150 – 200 mm	19.8%	19.6%	20.8%	21.5%	21.8%	21.2%
Bottom (240 mm)	20.7%	18.7%	21.7%	20.9%	20.8%	21.9%

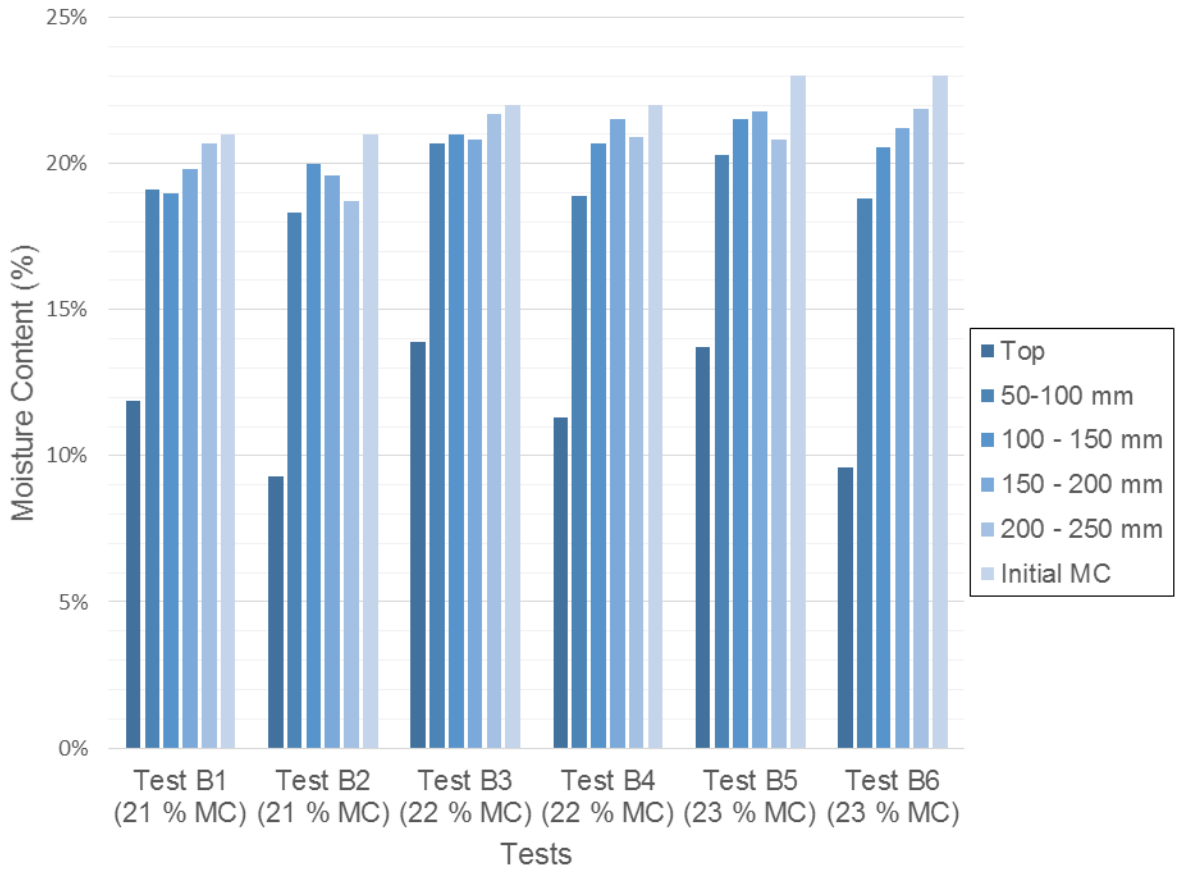

Figure 4.38: Moisture readings in embankment model after test

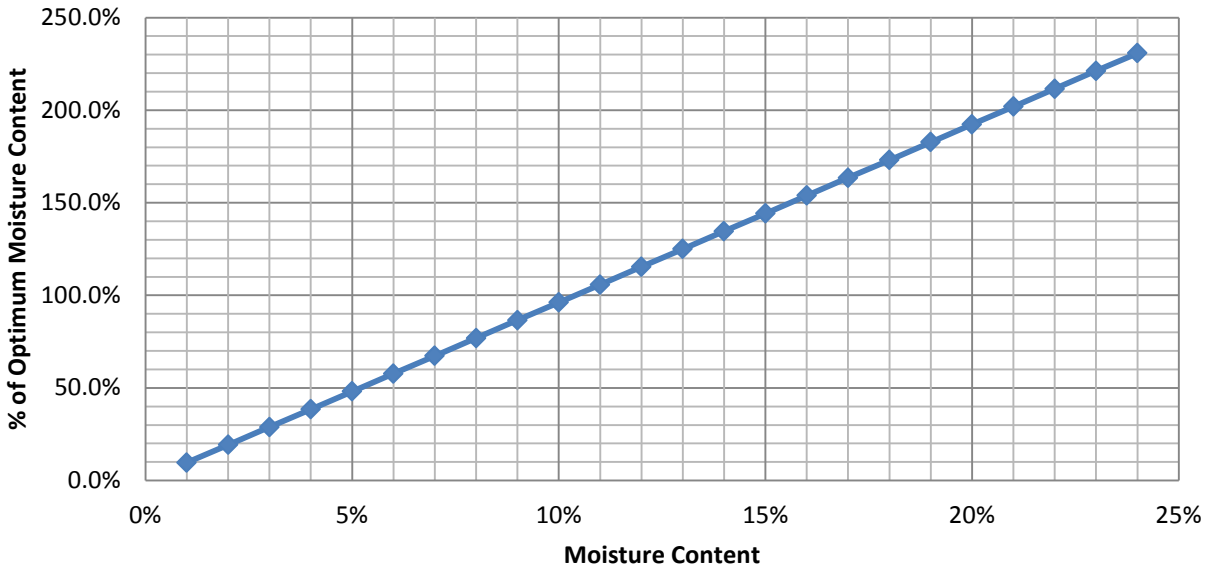

Figure 4.39: Moisture Content as a % of Optimum Moisture Content

4.3 LIMIT EQUILIBRIUM SLOPE STABILITY ANALYSIS

The slope stability analyses compared the Morgenstern-Price method of slices for a loaded embankment and unloaded embankment model. The dimensions of the embankment prototype (i.e. full scale) were used. An analysis was done comparing the factor of safety values for an increase in the suction intercept of the material. The material properties used in the analysis were obtained from the triaxial tests and the soil water characteristic curve. The triaxial test results produced a friction angle of 34º and a cohesion intercept value of 0 kPa. The bulk density obtained from 90 % Modified AASHTO compaction with a 22 % moisture content was used. The material properties used in the analyses are as follows:

- Unit Weight: 19.6 kN/m^3
- Friction angle: 34º
- Cohesion intercepts (Suction value) range: 0 kPa, 2 kPa, 5kPa, 10 kPa, 20 kPa, 40 kPa, 60 kPa and 80 kPa
- Loading = 38 kN/m^2

The same material properties were chosen for the embankment and its foundation. This was because the material used to build the embankments in the case studies were taken from borrow pits in the same area.

It was decided to do the analysis using cohesion values up to 80 kPa to model the expected suction based on the soil water characteristic curve. The matric suction at 22 % moisture content was 116 kPa. To convert this to additional shear strength given by cohesion, the following formula and calculation was used:

$\tau = (\sigma - u)tan34°$

The additional shear strength as a result of the suction is given by:

$-u * tan34°$

$-(-116) * tan34°$ = 78 kPa ≈ 80 kPa

The factor of safety values obtained from the analysis is given in Table 4.3. Comparing the factor of safety values obtained from the analysis using material properties from the triaxial test to the factor of safety value from the analysis using the cohesion value of 80 kPa, emphasis is put on the major effect that suction has on the embankment stability. Suctions are usually ignored in slope stability analysis. The comparison between the loaded and unloaded scenarios is plotted in Figure 4.40.

Table 4.3: Factor of Safety values obtained for the Limit Equilibrium slope stability analysis

Friction Angle (∅′)	Cohesion (c')	Factor of Safety (Loaded)	Factor of Safety (Unloaded)
34º	0 kPa	1.021	1.030
34º	2 kPa	1.178	1.219
34º	5 kPa	1.333	1.396
34º	10 kPa	1.531	1.636
34º	20 kPa	1.874	2.025
34º	40 kPa	2.436	2.687
34º	60 kPa	2.970	3.288
34º	80 kPa	3.481	3.863

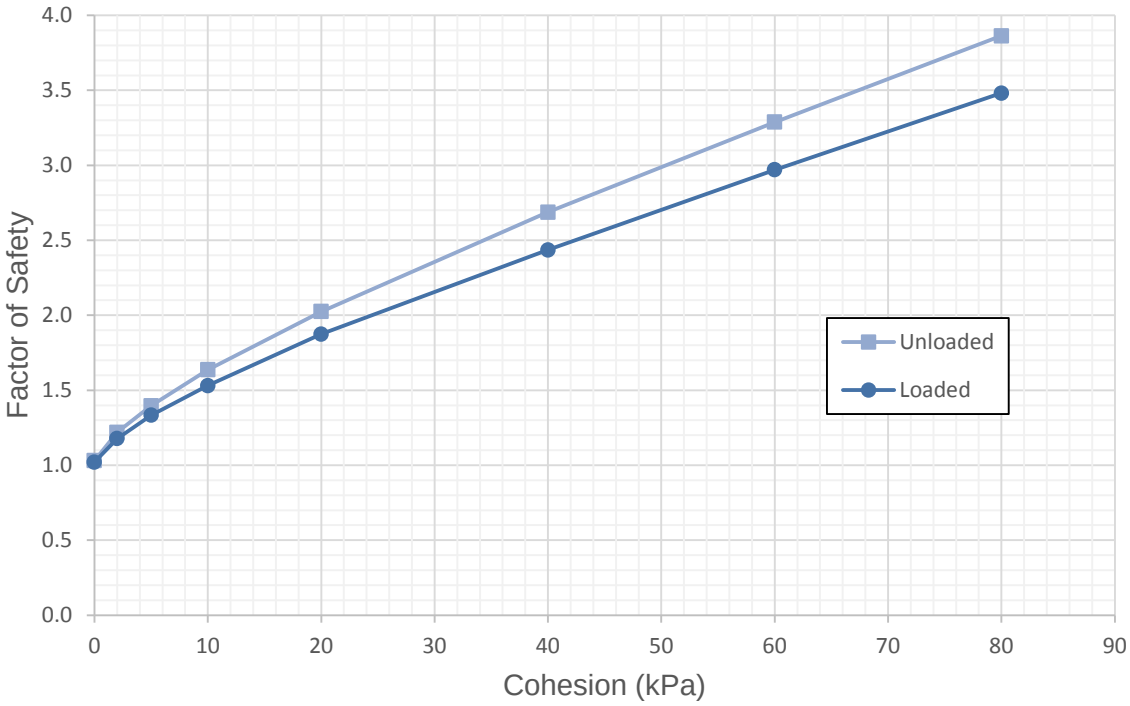

Figure 4.40: Factor of Safety values obtained for different suctions for loaded and unloaded scenarios

The slip surfaces obtained for 0 kPa and 80 kPa cohesion for the loaded and unloaded scenario analyses can be seen in Figures Figure 4.41 to Figure 4.44. The increase in cohesion changes the type of failure from a shallow slip surface to a deep seated failure.

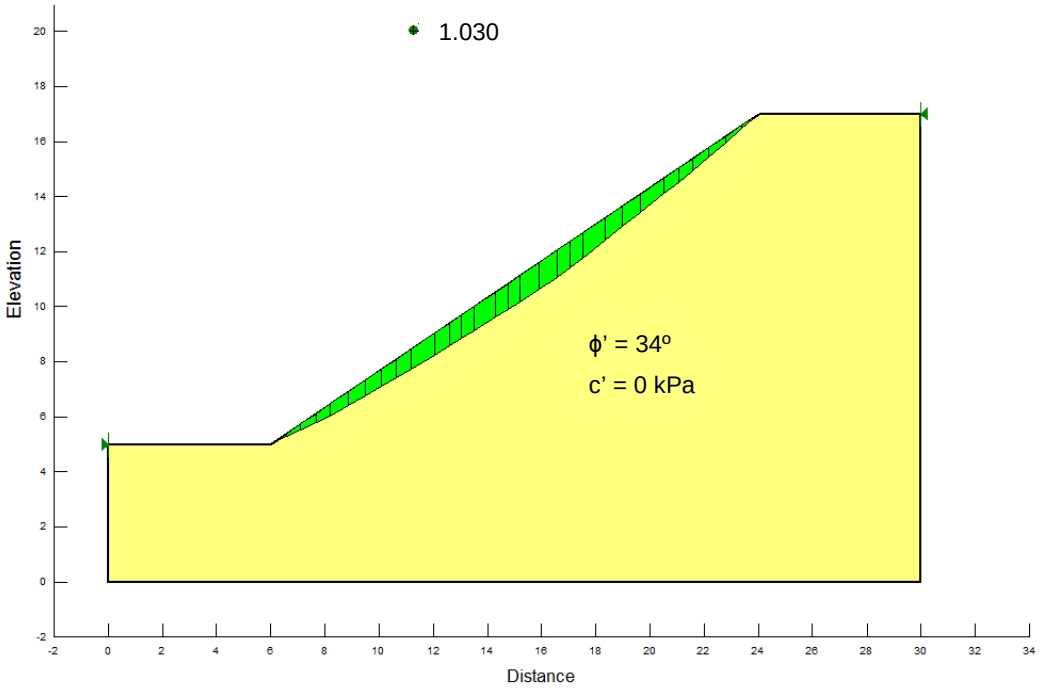

Figure 4.41: Slip surface for unloaded conditions at 0 kPa cohesion

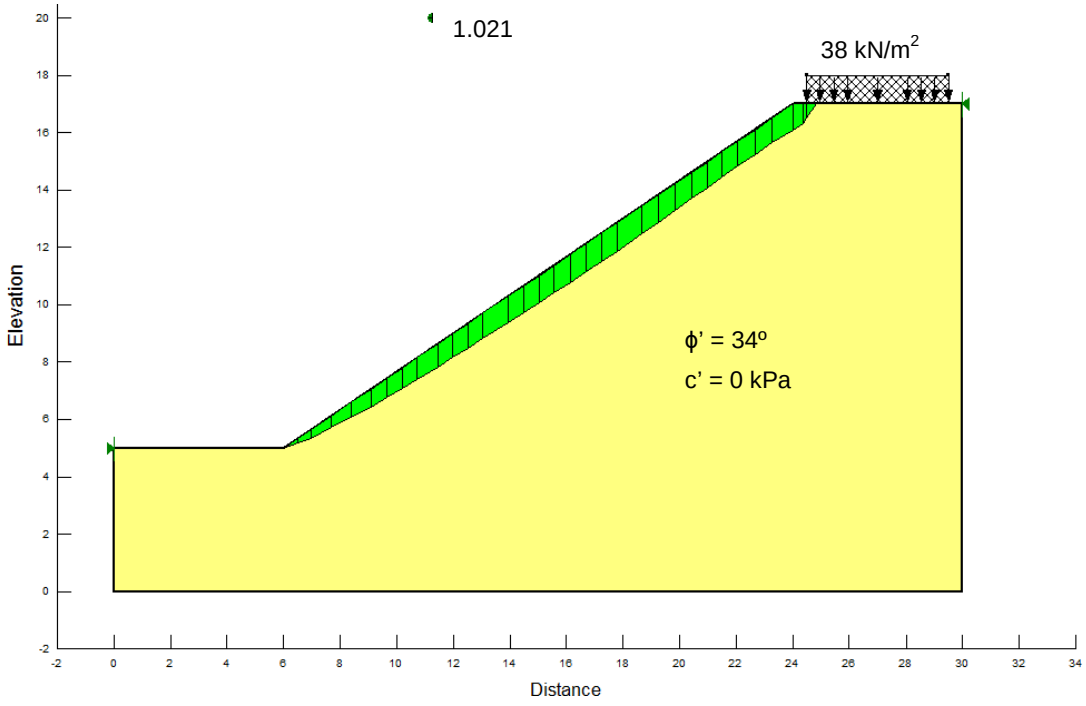

Figure 4.42: Slip surface for loaded conditions at 0 kPa cohesion

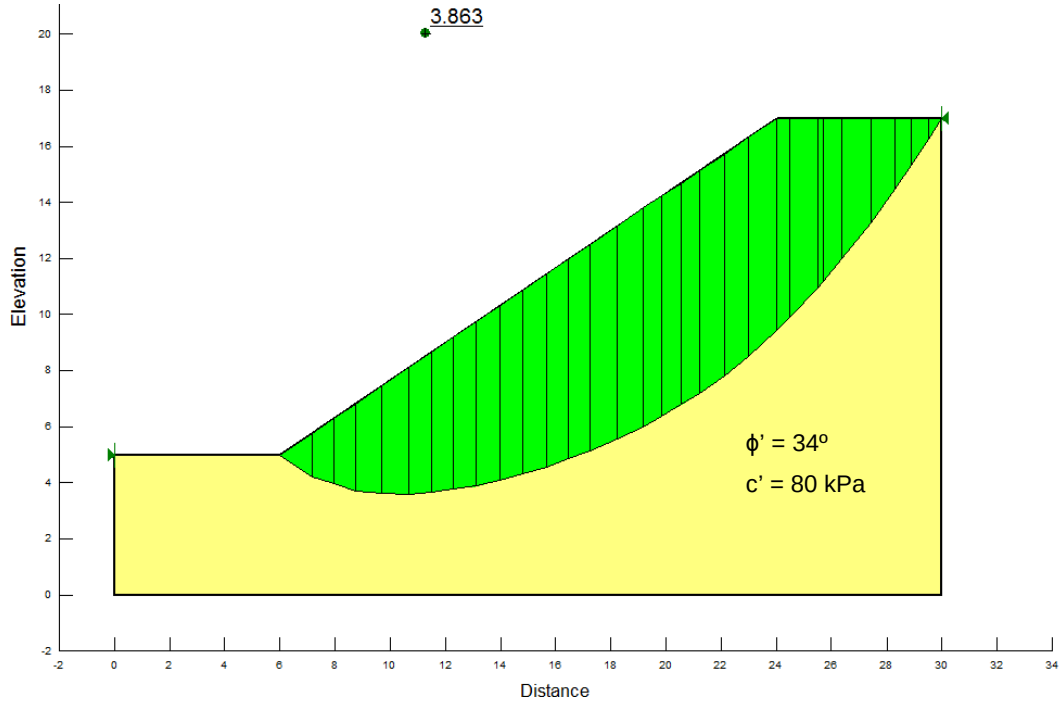

Figure 4.43: Slip surface for unloaded conditions at 80 kPa cohesion

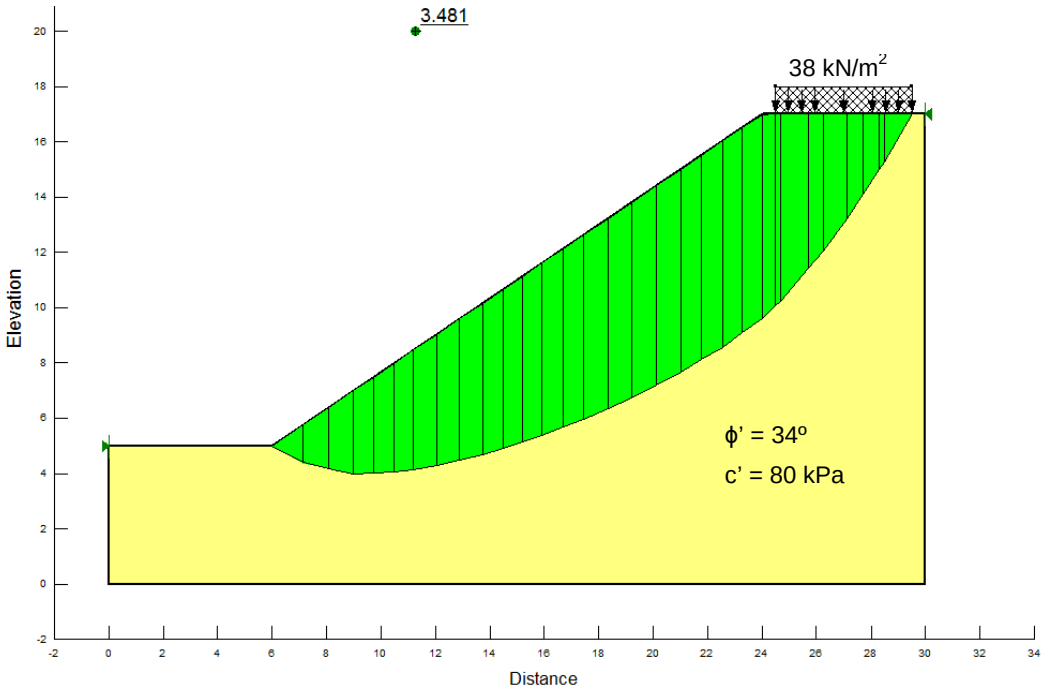

Figure 4.44: Slip surface for loaded conditions at 80 kPa cohesion

Comparing the factors of safety for all the analyses it is evident that the loaded conditions have lower factors of safety and a higher likelihood of failure. The failures observed in the case studies closely resemble the shallow slip surfaces obtained in the slope stability analysis. It should be noted that applying a certain cohesion value to the material properties, the assumption is made that the cohesion is constant throughout the entire model. This is however not the case on site where discontinuities can be expected in the embankment and the effect of cohesion on the embankment has a lower effect on the overall strength of and stability of the embankment and the likelihood of failure therefore increases.

4.4 COMPARISON OF SETTLEMENT RESULTS

The following comparisons were done in order to compare results and draw conclusions:

- Settlement during centrifuge acceleration
- Settlement during the stabilisation period of each test
- Settlement during the static loading periods of the tests
- Settlement during the cyclic loading periods of the tests.
- Comparisons between the static and cyclic loading settlement

4.4.1 Acceleration and Stabilisation Period Settlement

The settlement during the centrifuge acceleration for each test is shown in Figure 4.45. It is evident that for higher moisture contents there were higher settlement values, especially the difference between 23% and 24% moisture content. This can be seen as a turning point between a relatively stable slope and a slope collapse. It should also be noted that for the tests with the same moisture contents the settlements were not exactly the same. This could be due to variability in moisture throughout the embankment model or variability in the compacted density throughout the embankment model. The graph of the settlement during the stabilisation period follows the same pattern and is shown in Figure 4.46.

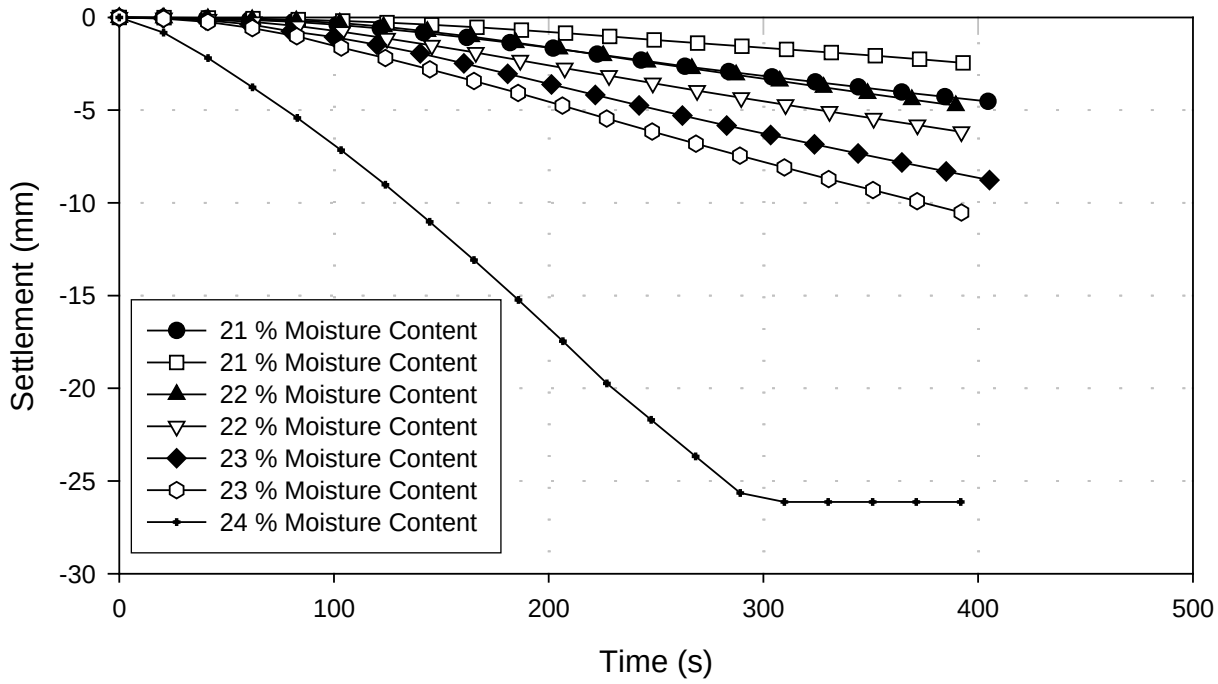

Figure 4.45: Settlement during centrifuge acceleration.

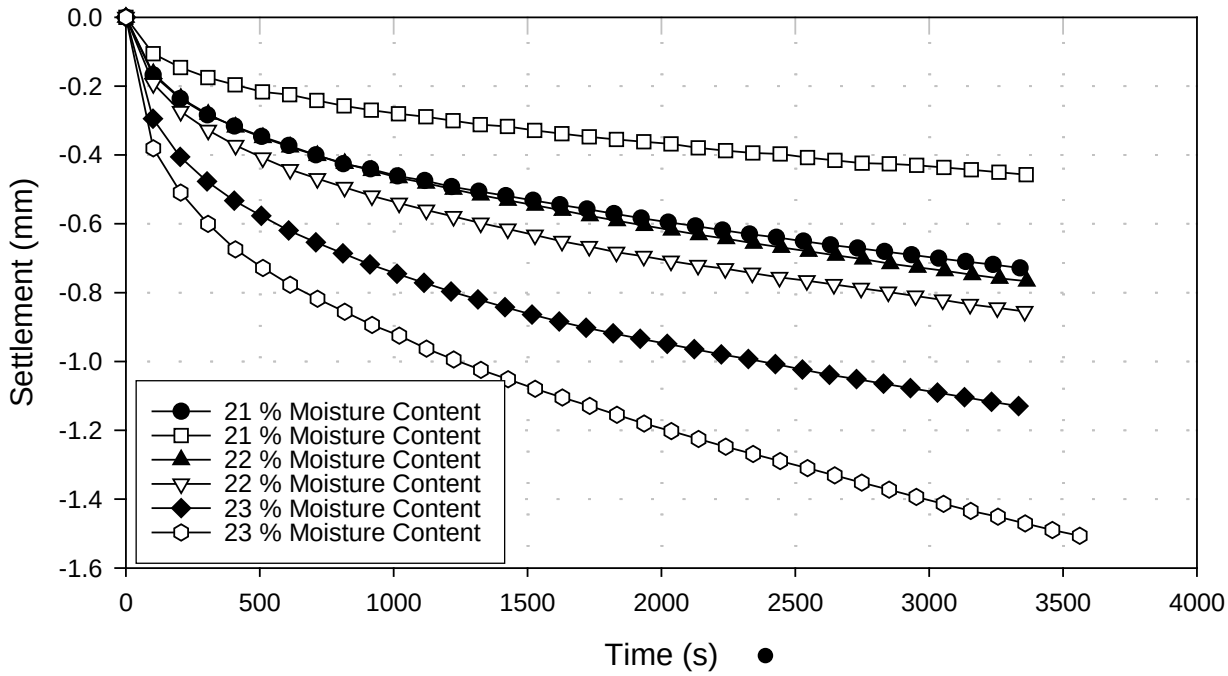

Figure 4.46: Settlement during the stabilisation period

4.4.2 Static Loading

The settlement of the different embankment models due to static loading is shown in Figure 4.47. The graph shows that for the tests with higher moisture contents larger settlements were obtained, which was to be expected.

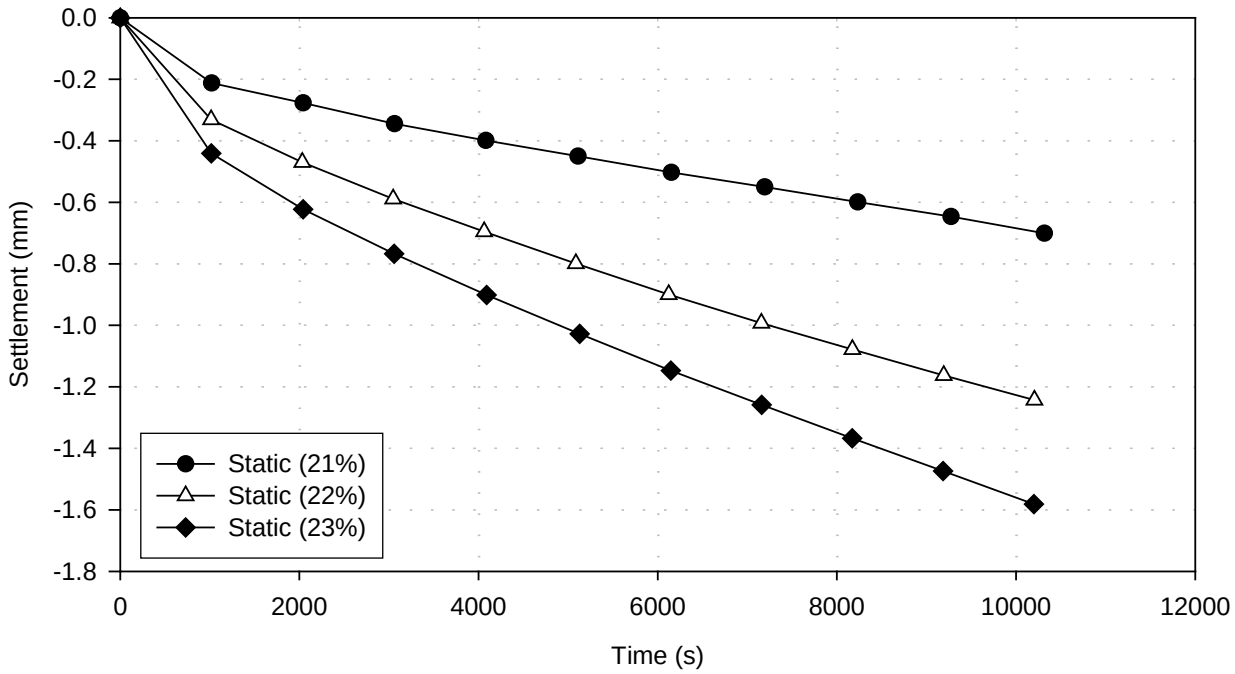

Figure 4.47: Comparison between settlements during static loading

4.4.3 Cyclic Loading

The cyclic loading pattern should follow the same pattern as the static loading, where the test with higher moisture content would have larger settlements. This was the case for two of the tests, namely the tests with 22% and 23% moisture content. As mentioned in Section 4.2.2 a few problems were experienced during the 21% moisture content test where cyclic loading was done. Once the problem was fixed the settlement rate of the curve decreased substantially and started behaving as expected with a lower rate of settlement compared to the 22% and 23 % moisture content tests. The settlement comparisons can be seen in Figure 4.48. The 23 % moisture content test's settlement curve shows a significant increase compared

to the 21 % and 22 % moisture content tests. This can be attributed to the significant effect cyclic loading has on a material when it passes a certain moisture content. The moisture content in question can be related to the air entry point when referring to the SWCC. In section 4.1.3 this was shown to be 22 % moisture. When the moisture content of a soil increases to above the moisture content corresponding to the air entry value, the soil would be expected to become saturated with a subsequent decrease in pore water suctions and hence a decrease in the shear strength of the material. A decrease in the shear strength of the material will in turn result in an expected increase in settlement under loading.

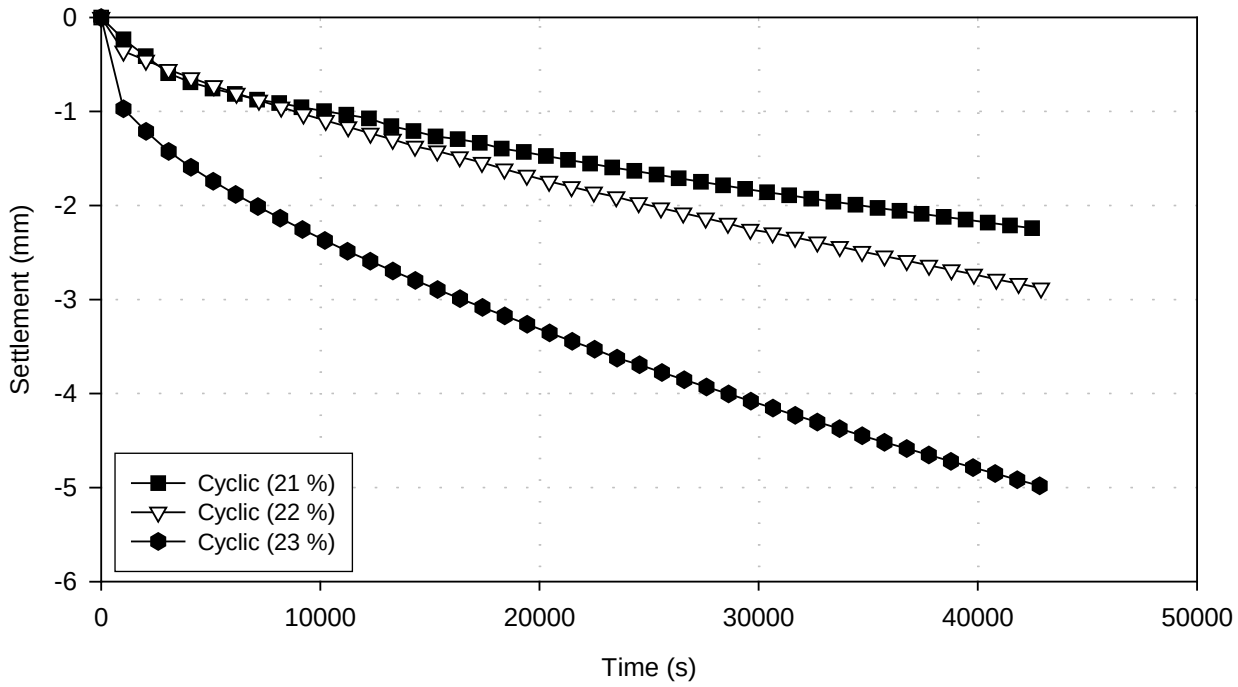

Figure 4.48: Settlement comparison during cyclic loading for different moisture contents

4.4.4 Static vs. Cyclic Loading

Graphs were drawn to compare the settlement curves between static and cyclic loading for the different moisture contents. A direct comparison was made between the static loading and cyclic loading tests at the complete static loading tests' time interval of 3 hours. The settlement comparison curves at this time interval from the static and cyclic loading test are shown in Figure 4.49. The tests at 21 % and 22 %

moisture contents show a close settlement grouping as well as the static loading test conducted at 23 % moisture content. The settlement curve for the cyclic loading test at 23 % moisture content shows a significant increase. This significant increase in settlement for the cyclic loading test at 23 % moisture content shows the large effect that cyclic loading has on a material with an increase in moisture content. As mentioned in the previous section this can be attributed to the significant effect cyclic loading has on a material when it passes the moisture content corresponding to the air entry point when referring to the SWCC.

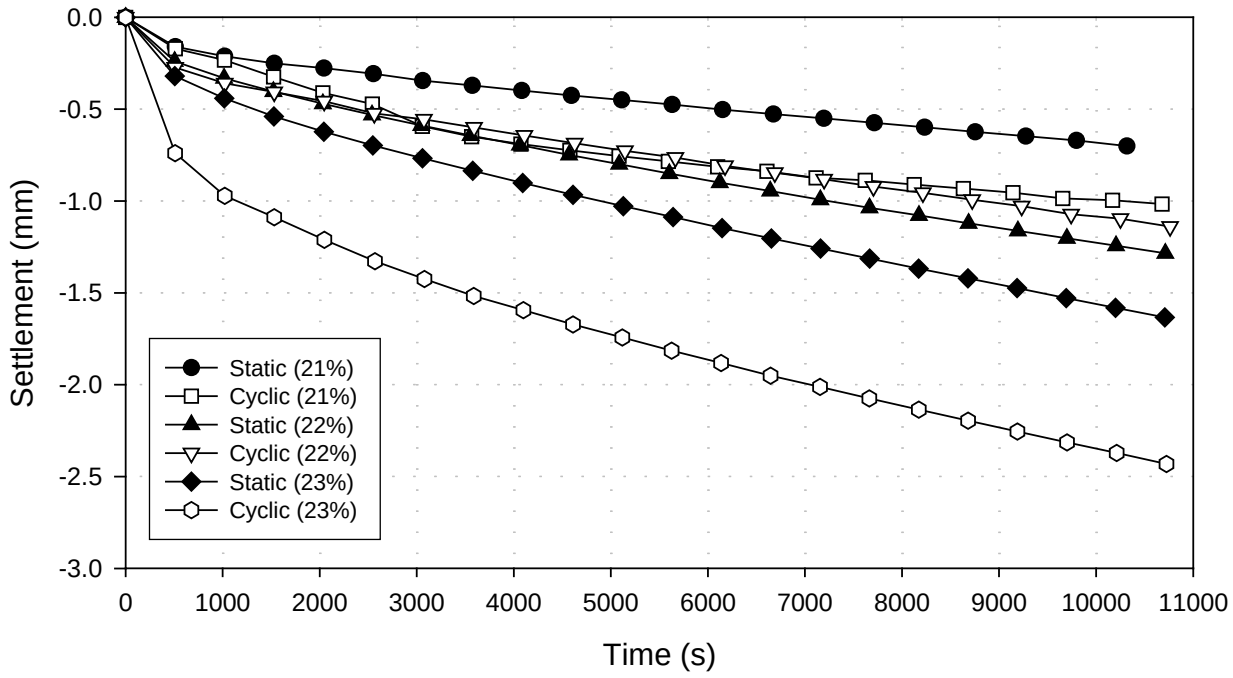

Figure 4.49: Settlement comparison curves between static and cyclic loading tests at 3 hours

The comparison between the static and cyclic loading was further made by taking into account only the actual time that the load was in contact with the embankment for the cyclic loading tests. During the 20 second loading and unloading cycle, the embankment is loaded for approximately 2.5 to 3.5 seconds. In order to compare the cyclic and static loading settlement amount for the duration the embankment was physically loaded, a conservative value of 4 seconds of loading per 20 second cycle was chosen, which is a fifth of 20 seconds. The settlement curves for the cyclic loading tests were therefore shortened by a factor of 5. Therefore, the 12 hour settlement of the cyclic loading is compared to the 2.4 hour point

during the static loading test. The full settlement curves for all the tests and the change in the cyclic settlement curve time axes to loaded time only is shown in Figure 4.50 to Figure 4.53.

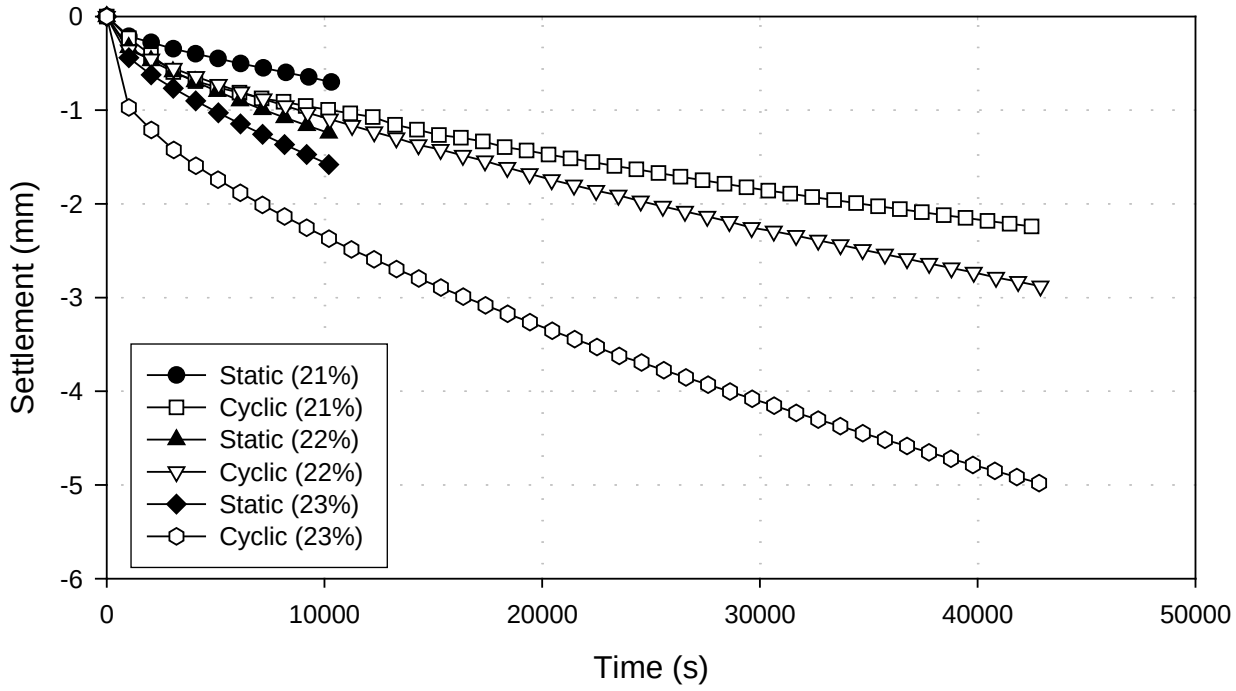

Figure 4.50: Complete settlement curves for all static and cyclic loading tests

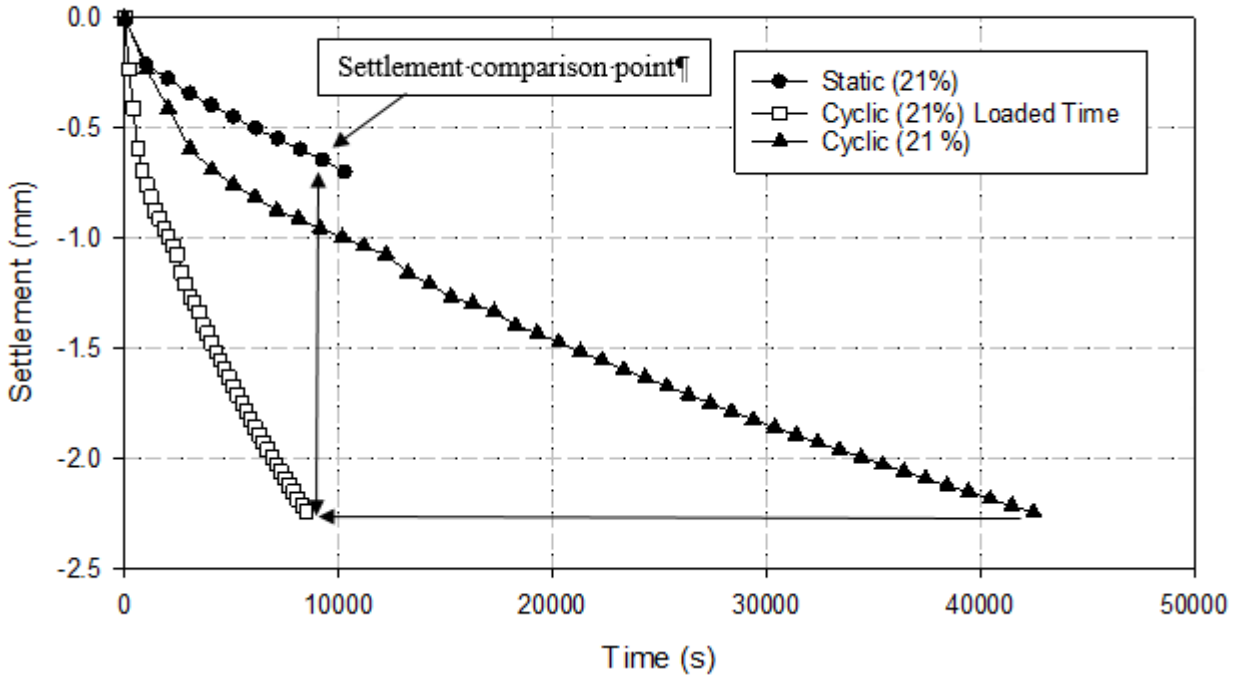

Figure 4.51: Changing the cyclic settlement curve time to loaded time (23% Moisture Content)

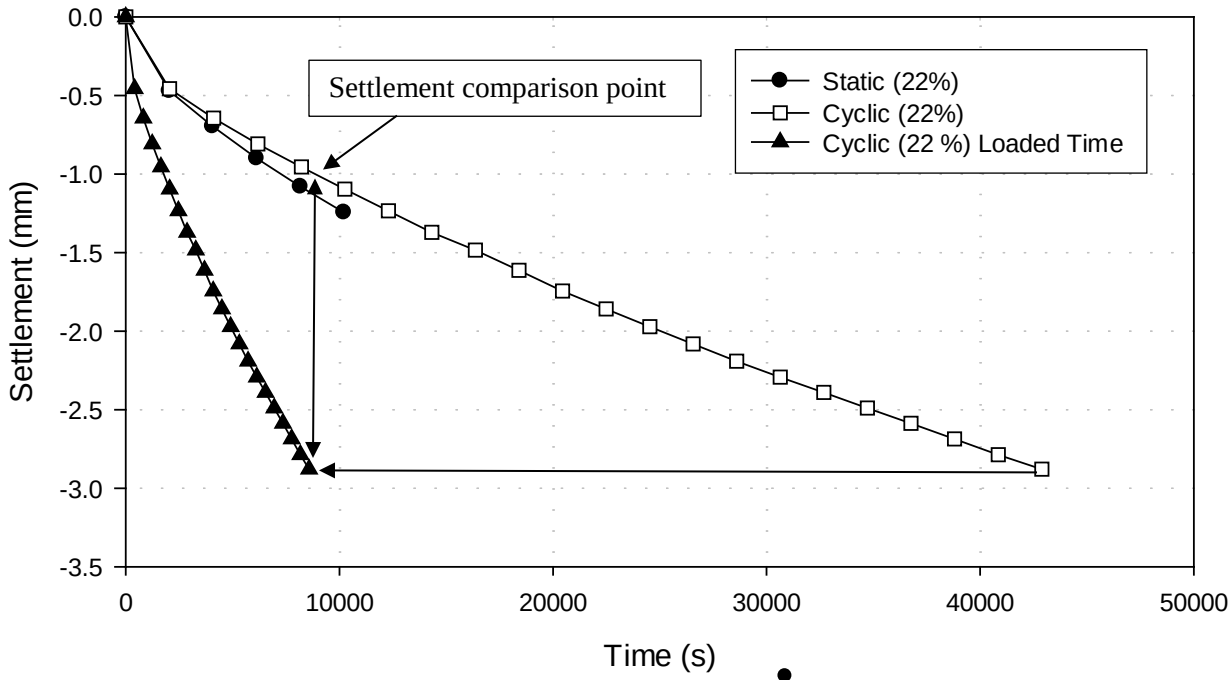

Figure 4.52: Changing the cyclic settlement curve time to loaded time (22% Moisture Content)

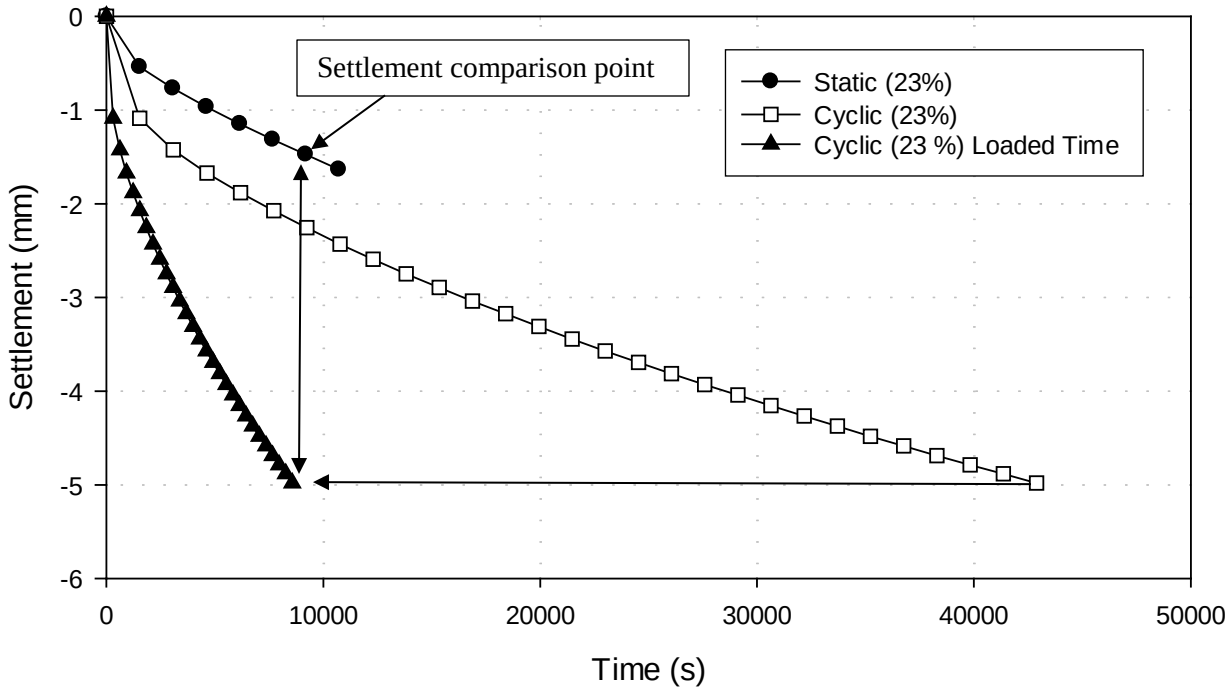

Figure 4.53: Changing the cyclic settlement curve time to loaded time (23% Moisture Content)

To obtain a more accurate representation of the difference in settlement between the static and cyclic loading when taking into account only the loaded time, the settlement that took place during the unloaded period of each cycle in the cyclic loading test was removed. This can be viewed as the settlement due to the self-weight of the embankment alone. The bar chart in Figure 4.54 shows the amount of accumulated settlement that took place during the loading period of each cycle and the amount of accumulated settlement that took place during the unloaded period of each cycle with the cyclic loading tests. The amount of settlement that took place during the unloaded period of the cyclic loading test was approximately 5 to 10 % of the total settlement, despite the loaded period being only 2.5 to 3.5 seconds of the 20 seconds loading cycle.

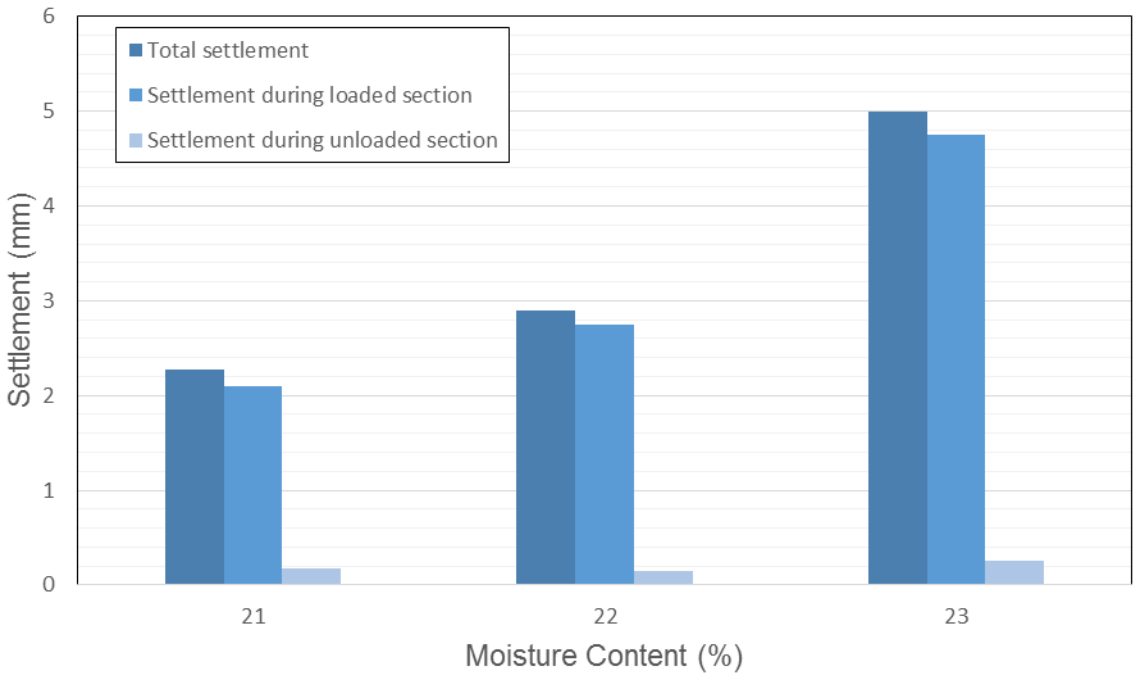

Figure 4.54: Total settlement during cyclic loading tests separated between self-weight and loading settlement.

The settlement curves from all the tests plotted against loaded time are shown in Figure 4.55. The final settlements for each testing phase in the geotechnical centrifuge are given in Figure 4.56. The graph shows a similar pattern for the different moisture contents and a clear increase in settlement is visible as the moisture content increases. It is clear that the most settlement occurs during the acceleration period of the centrifuge. This is to be expected as the stresses and forces on the embankment due to its self-weight increases substantially from 1 g to 50 g acceleration. The stabilisation period was added to the test procedure to reduce the effect of the initial settlement due to self-weight of the embankment at 50 g on the settlement created as a result of the loading. The settlement as a result of the cyclic loading was on average 67 % higher (70 % at 21 % moisture content; 60 % at 22 % moisture content and 70 % at 23 % moisture content) than that of the static loading when considering the loaded time only. This can be attributed to particle rearrangement during the cyclic loading process as well as changes in the pore water pressure or suction.

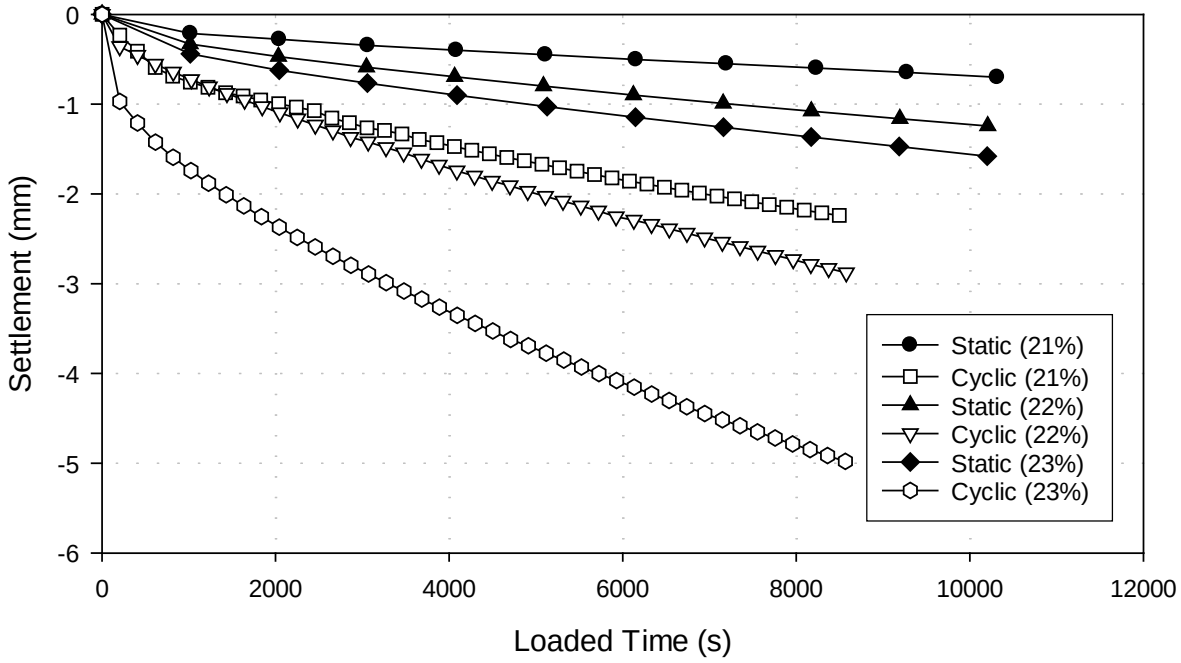

Figure 4.55: Settlement curves for all tests plotted against loaded time

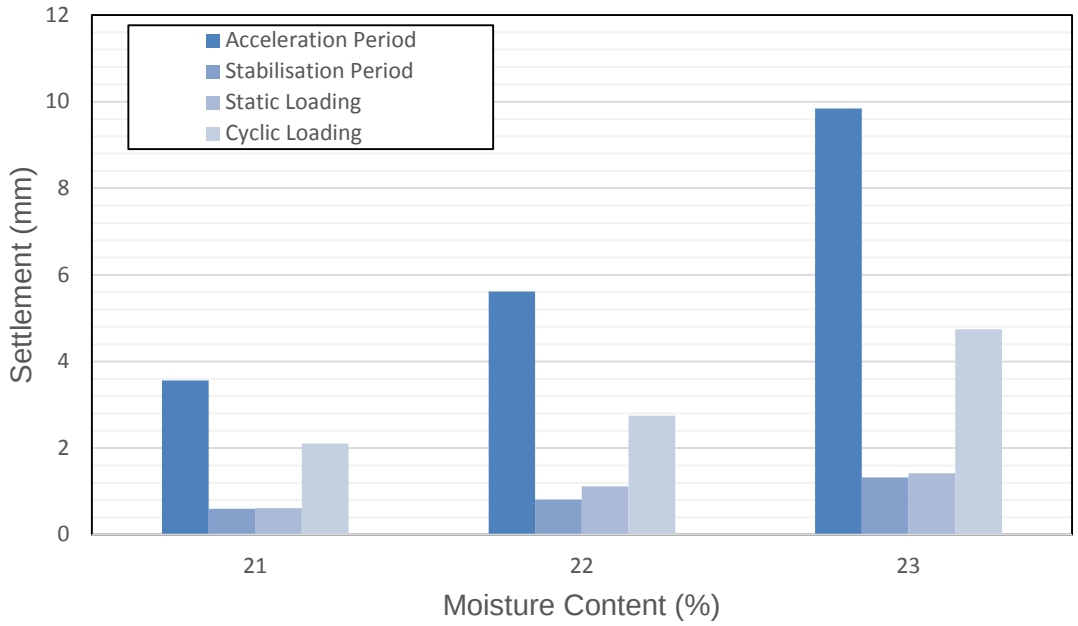

Figure 4.56: Final centrifuge testing settlement for each period during the tests for the same effective loaded time (2.4 hours)

The increase in the settlement difference between static and cyclic loading with regard to loaded time settlement only shows an increase of 8.7 % from 21 % to 22 % moisture content, however a large increase of 51.0 % settlement difference is seen from 22 % to 23 % moisture content. This emphasises the effect that the moisture content of a soil has on its shear strength when the moisture increases above the moisture content corresponding to the air entry value. At this level of saturation there is a definite decrease in pore water suctions and hence a decrease in the shear strength of the material. The material had a 93 % degree of saturation at 22 % moisture content with a corresponding suction value of 75 kPa obtained from the SWCC and at a 97 % degree of saturation at 23 % where the corresponding suction value decreases significantly to 49 kPa. The soil is expected to be in the capillary regime at this level of saturation.

4.4.5 Comparison between Visual Results, Slope Stability Analyses and SWCC

Visual results were recorded during and after each centrifuge test. The embankment models showed significant cracking as a result of shrinkage due to moisture loss which was substantiated by the moisture content samples taken after each test. There were however cracks which indicated shearing of the material as well as material movement. These cracks were in most cases across the length of the embankment at the crest of the embankment as shown in Figure 4.29 and formed at the test with 23 % moisture content. Although a completed slip surface failure was not created during the tests, these cracks could lead to a slope failure once more water enters cracks through precipitation. The cracks could be seen before the loading was applied and therefore indicates that they are not connected to static or cyclic loading but rather to the moisture content of the soil. The position of these cracks correlate well with the slope stability analysis conducted in GeoStudio. The shallow slip surface calculated with the slope stability analysis also started at the crest of the embankment for loaded and unloaded conditions and therefore substantiates the formation of cracks at the crest of the embankment in the centrifuge tests before the loading started. The analyses conducted with higher cohesion intercept values in GeoStudio showed deep seated failures with large Factor of Safety values. This shows that the amount of cohesion in the soil, which can be seen as the suction value, has a significant effect on the slope stability. There was a clear cohesive strength characteristic to the embankment model as a result of the compaction effort and moisture content in the soil and therefore the likelihood of seeing a complete slope failure during the centrifuge tests was low. The SWCC showed that for the moisture content range used in the centrifuge

tests with 21 – 23 % moisture, there is a significant amount of suction present in the soil. The effect of the soil drying during the tests significantly increased the soil suction strength on the surface of the embankment model, thereby reducing the likelihood of a slope failure of occurring.

5 CONCLUSION AND RECOMMENDATIONS

This chapter includes the final conclusions of the study as well as recommendations for further study in the field and for the testing method.

5.1 CONCLUSIONS

The conclusions to the research conducted are described below.

5.1.1 Centrifuge Tests

The centrifuge tests were conducted on clayey sand material sampled from a slope failure site on the South African heavy haul coal line. Iterative tests were conducted where the moisture content in the embankment models was changed to obtain the moisture content range where the embankment model changes from a stable to an unstable slope. The moisture content range obtained was between 20 % and 24 % moisture, where the embankment model showed significant stability at 20 % moisture content and completely collapsed at 24 % moisture content.

Centrifuge tests were then conducted on embankment models at 21 %, 22 % and 23 % moisture contents to investigate the effect of static and cyclic loading. The results from the tests conducted on the railway embankment models in the geotechnical centrifuge indicated that cyclic loading significantly increases the magnitude of the vertical settlement which could lead to slope failures. It was observed that the moisture content has a significant effect on the slope stability. A completed slip surface failure was not observed. However, significant cracks formed at the crest of the embankment along its length which could induce a failure once water enters those cracks. The static and cyclic loading tests at 21 % and 22 % moisture contents, as well as the static loading test at 23 % moisture content, showed similar settlement curves with only minor increases in settlement with an increase in moisture content. The settlement curve for the cyclic loading test at 23 % moisture content showed a significant increase in settlement. The substantial increase in settlement for the cyclic loading test at 23 % moisture content, emphasised the significant effect that cyclic loading has on a material as the moisture content is increased.

In order to compare the cyclic and static loading settlement amounts, the duration the embankment was physically loaded was considered. A conservative value of 4 seconds of loading per 20 second cycle was chosen for the cyclic loading tests. The settlement curves for the cyclic loading tests were therefore shortened by a factor of 5. The settlement as a result of the cyclic loading was on average 67 % higher than that of the static loading when considering the loaded time. This can be attributed to particle rearrangement during the cyclic loading process as well as changes in the pore water pressure or suction.

The settlement that took place during the unloaded period of each cycle in the cyclic loading test was removed from the total settlement for the cyclic loading tests. This can be viewed as the settlement due to the self-weight of the embankment alone. The amount of settlement that took place during the unloaded period of the cyclic loading test was approximately 5 to 10 % of the total settlement, despite the loaded period being only 2.5 to 3.5 seconds of the 20 seconds loading cycle.

The settlement difference between static and cyclic loading with regard to loaded time increased by 8.7 % for the 21 % and 22 % moisture content samples, however a 51.0 % increase in the settlement difference was observed for the 22 % and 23 % moisture content samples. This emphasises the effect that the moisture content of a soil has on its shear strength when the moisture increases above the moisture content corresponding to the air entry value and level of saturation. At this level of saturation there is a definite decrease in pore water suctions and hence a decrease in the shear strength of the material. A decrease in the shear strength of the material will in turn result in an expected increase in settlement under loading. The material had a 93 % degree of saturation at 22 % moisture content with a corresponding suction value of 75 kPa obtained from the SWCC and at a 97 % degree of saturation at 23 % MC where the corresponding suction value decreases significantly to 49 kPa. The soil is expected to be in the capillary regime at this level of saturation.

The effect that moisture content has on a problem material should be of utmost importance in the design of an embankment. Small differences in the moisture content value can make the difference between a stable embankment and an unstable embankment. This was evident by observing the stability of the embankment at moisture contents of between 23% and 24% where there was a complete collapse of the embankment during the centrifuge acceleration period for the test at a moisture content of 24%.

5.1.2 Development of a loading system

Two loading systems were considered for the cyclic and static loading of the tests. The initial loading condition considered would have modelled the loading at a point on the embankment and would have incorporated an electromagnetic shaker. The second loading system that was considered and chosen to be used, simulated the loading created by a heavy haul coal train with a 26 t per axle load along the length of an embankment. A loading block was machined to simulate the load generated by the train on the embankment and a pneumatic piston used to cycle the load on and off the embankment. The cycle time per load was calculated from the length of the train and the time it takes to pass a section on an embankment. The results from the settlement analysis between the static and cyclic loading demonstrated the effectiveness of the loading device and the ability to simulate the effect that cyclic loading has on embankment stability.

5.1.3 Material analysis

The study was based on reports and investigations on embankment failures that occurred on the Ermelo-Richards Bay heavy haul coal export line. For this reason a similar material to that found on the sites where the failures occurred had to be used for the centrifuge tests. The material was sampled from one of the sites from the slope failure investigation report where a failure occurred. The material was a clayey sand. Triaxial tests gave a friction angle of 34º and a cohesion value of 0 kPa which were used in the slope stability analysis.

The soil water characteristic curve showed the material had significant suction capabilities. The air entry suction point corresponded to a moisture content value of approximately 26 % and a degree of saturation of 93% for the test conducted to obtain the SWCC. The bulk density of the material at this point was 1938 kg/m^3. The corresponding 90 % modified AASHTO density at 93 % degree of saturation was 2009 kg/m^3 with a moisture content of 22 %. This moisture content could therefore be taken as the turning point where there was a significant increase in suctions and therefore strength during drying or loss in suctions during wetting. When the moisture content of a soil increases to above the moisture content corresponding to the air entry value, the soil would be expected to become saturated with a subsequent decrease in pore water suctions and hence a decrease in the shear strength of the material. A decrease in the shear strength of the material will in turn result in an expected increase in settlement under loading.

The minimum void ratio obtained from the soil water characteristic curve test was 75 %. This can be seen as representative of the true shrinkage limit and the minimum volume the soil can attain during drying to zero water content.

Further slope stability analyses were conducted using the soil suction results obtained from the SWCC. The slope stability analyses were conducted up to a cohesion value of 80 kPa and produced significantly higher factor of safety values from a factor of safety value of 1.02 for 0 kPa cohesion to a factor of safety value of 3.48 for 80 kPa cohesion and changed the mechanism of failure from a shallow slip surface to a deep seated failure.

5.1.4 Modelling Procedure

Two modelling procedures were followed to build, compact and instrument an embankment model for the geotechnical centrifuge tests. The first procedure involved compacting the material outside the centrifuge strongbox in a separate box with removable panels, then carving out the embankment model and placing it in the strongbox thereafter. The main disadvantages when the modelling and compaction was done outside the strongbox are summarised below:

- Swelling of the material.
- Soil sticking to compaction box panels when they are removed.
- Moisture loss during the carving process.
- Deformation and disturbance of model during placement in the strongbox.
- Small spaces and gaps between the model and strongbox after placement.

The second procedure involved compacting the material inside the centrifuge strongbox. The disadvantages of modelling inside of the strongbox were mainly the carving process and the risk of damaging the glass of the strongbox when compacting. This was however overcome or mitigated and proved to be the preferred modelling method.

5.2 RECOMMENDATIONS

The following recommendations should be noted for further studies:

- Conduct tests on a non-problematic embankment material in order to build a correlation between the static and cyclic loading methodologies on other materials.
- Different slope angles should be tested.
- Adding water to the embankment model at a certain time interval during the test when cracks have formed to test the effect of water ingress into cracks on the slope stability of an embankment.
- When conducting long duration centrifuge test where moisture content plays a large role in the outcome of the test, a cover should be put in place to prevent the model from drying out or, ideally, a climate chamber should be used.
- Piezometers/tensiometers should be placed in the embankment to measure the excess pore water pressure and suctions in the embankment model during the test as this greatly affects the effective stress in and hence response of the slope.
- Reduce the model scale in order to model a complete embankment to remove edge effects where symmetry is assumed.
- Use multiple cameras to capture the complete cross section of the embankment model in the photos for PIV analysis.

6 REFERENCES

Bishop, A. W. (1959). *The principle of effective stress*.'' Teknisk Ukeblad I Samarbeide Med Teknikk, Oslo, Norway, 106(39), 859–863.

Bishop, A. W., Bjerrum L. (1960). *The Relevance of the Triaxial Test to the Solution of Stability Problems*. In Proc., ASCE Research Conference on the Shear strength of Cohesive Siols, Boulder, Colorado, American Society of Civil Engineers, New York, pp. 437-501.

Bishop, A. W., and Henkel, D.J. (1962). *The Measurement of Soil Properties in The Triaxial Test*, Edward Arnold Ltd., London, second edition.

Briggs, K. M., Smethurst, J. A., Powrie,W. & O'Brien, A. S. (2013). *Wet winter pore pressures in railway embankments*. Proc. Instn Civ. Engrs – Geotech. Engng 166, No. 5, 451–465.

Craig, R.F. 2004. *Craig's Soil Mechanics*. 7th ed. New York: Spon Press.

Cilingir, U. Madabhushi,. S.P.G 2010. *Particle Image Velocimetry analysis in dynamic centrifuge tests*. Physical Modelling in Geotechnics – Springman, Laue & Seward (eds). Taylor & Francis Group, London

Collins B.D. and Znidarcic D. (2004) *Stability analyses of rainfall induced landslides*. Journal of Geotechnical and Geoenvironmental Engineering, ASCE 130(4): 362–372.

Fourie A.B., Rowe D. and Blight G.E. (1999). *The effect of infiltration on the stability of the slopes of a dry ash dump*. Ge´otechnique 49(1): 1–13.

Fredlund, D.G., (1964). C*omparison of soil suction and one-dimensional consolidation characteristics of a highly plastic clay*. National Research Council of Canada, Division of Building Research, Technical Report No. 245, Ottawa, Ontario, Canada.

Fredlund, D. G., Morgenstern, N. R., and Widger, R. A. (1978). *Shear strength of unsaturated soils*. Canadian Geotechnical Journal, 15, No. 3, 313–321.

Fredlund, D. G. & Rahardjo, H. (1993). *Soil mechanics for unsaturated soils*. New York: Wiley Interscience.

Fredlund, D.G. Stone, J. Stianson, J. and Sedgewick, A. (2011). *Determination of the water storage and permeability functions for oil sands tailings*. Tailings and Mine Waste 2011. Vancouver, Canada

Grabe, P.J. and Clayton C.R.I, (2009). *Effects of Principal Stress Rotation on Permanent Deformation in Rail Track Foundations* . Journal of Geotechnical and Geoenvironmental Engineering

Gunn D.A., Haslam E., Kirkham M., Chambers J.E., Lacinska A., Milodowski A., Reeves H., Ghataora G., Burrow M., Weston P., Thomas A., Dixon N., Sellers R., Dijkstra T.. (2009). *Moisture measurements in an end-tipped embankment*: Application for studying long term stability and ageing. In: Proc. 10th int. conf. railway engineering, London;

Hughes, P.N., Glendinning, S., Mendes, J., Parkin, G., Toll, D.G., Gallipoli, D. & Miller, P. (2009). *Full-scale testing to assess climate effects on embankments.* Engineering Sustainability: Proc. Institution of Civil Engineers 162(2): 67-79.

Jacobsz, S.W., Kearsley, E.P. and Kock, J.H.L. 2014. T*he geotechnical centrifuge facility at the University of Pretoria*. Proceedings of the 7th International Conference on Physical modelling in Geotechnics. Submitted for publication.

Kutter, B.L. (1992). *Dynamic Centrifuge Modeling of Geotechnical Structures*. Transportation Research Record 1336. TRB National Research Council, pp. 24-30

Lu, N and Likos, W.J. (2004). Unsaturated soil mechanics. John Wiley and Sons. New Jersey. USA.

Loveridge, F. A., Spink, T. W., O'Brien, A. S., Briggs, K. M. & Butcher, D. (2010). *The impact of climate and climate change on UK infrastructure slopes*. Q. J. Engng Geol. Hydrogeol. 43, No. 4, 461–472.

Malvern Instruments LTD. (2012). *Mastersizer 2000*. [Online] Available at: www.malvern.com.

McQueen, I. S., and Miller, R. F. (1974). *Approximating soil moisture characteristics from limited data: Empirical evidence and tentative model.* Water Resources Research, 10(3), 521–527.

O'Reilly, M. P., and Brown, S. F. (1991). *Cyclic loading of soils: From theory to design*. Blackie. Glasgow, U.K

O'Brien, A., Ellis, E. A. & Russell, D. (2004). Old railway embankment clay fill: laboratory experiments, numerical modelling and field behaviour. Advances in geotechnical engineering: Proceedings of the Skempton Conference, Imperial College, London, Vol. 2, pp. 911–921.

Rahardjo, H., Lim, T.T., Chang, M.F., and Fredlund, D.G. (1995). *Shear-strength characteristics of a residual soil*. Canadian Geotechnical Journal, 32(1): 60–77.

Rahardjo, H. Lee, T.T. Leong, E.C. and Rezaur, R.B. (2005). *Response of a residual soil slope to rainfall*, Canadian Geotechnical Journal, Vol. 42, No. 2

Richards Bay Coal Line - Wikiwand. 2015. Richards Bay Coal Line - Wikiwand. [ONLINE] Available at: http://www.wikiwand.com/de/Richards_Bay_Coal_Line. [Accessed November 2015].

Scott JM, Loveridge F and O'Brien AS (2007) *Influence of climate and vegetation on railway embankments*. In Proceedings of the 14th European Conference on Soil Mechanics and Geotechnical Engineering, Madrid (Cue´llar V, Dapena E, Alonso E et al. (eds)). Millpress, Amsterdam, the Netherlands, pp. 659–664.

Selig, E. T. and Waters, J. M. (1994). *Track Geotechnology and Substructure Management*. Thomas Telford, London.

Selig, E.T. (2013) Railway Substructure Engineering. Mediawiki [Online]. Available at: http://railwaysubstructure.org/railwiki/ (Accessed: 10th December 2015).

Smethurst JA, Clarke D and Powrie W (2006) *Seasonal changes in pore water pressure in a grass-covered cut slope in London Clay*. Ge´otechnique 56(8): 523–537.

Smethurst, J., Briggs, K., Powrie, W., Ridley, A. and Butcher, D., (2015). *Mechanical and hydrological impacts of tree removal on a clay fill railway embankment*. Geotechnique, 65 (11), pp. 869-882.

Take, W. A. & Bolton, M. D. (2004). *Identification of seasonal slope behaviour mechanisms from centrifuge case studies*. Proc. Skempton Memorial Conf. 2, 992–1004.

Taylor, R.N., (1995). *Geotechnical Centrifuge Technologies*. 1st ed. London: Blackie Academic & Professional. (s.l.): (s.n.).

Terzaghi, K., 1943, *Theoretical Soil Mechanics*, Wiley, New York.

Tubey, L W & Bulman, J N 1964. *Micaceous soils: Methods of determining mica content and the use of routine tests in the evaluation of such soils*. Proceedings of the Australian Road Research Board, 2: 880–901.

Turner, A. Keith, and Schuster, Robert L., (1996). *Landslides— Investigation and mitigation*: National Research Council, Transportation Research Board Special Report 247, National Academy Press, Washington

Vaughan P. R. (1994) Assumption, prediction and reality in geotechnical engineering (34th Rankine Lecture). Ge´otechnique, 44, No. 4, 573–609.

Vinogradov, V.V. Frolovsky Y.K. Zaitsev A.A. (2010). *Development of train loading device and testing on sandy and clay models. Physical Modelling in Geotechnics.* Springman, Laue & Seward (eds). Taylor & Francis Group, London.

Wang G and Sassa K (2001) *Factors affecting rainfall-induced flowslides in laboratory flume tests*. Ge´otechnique 51(7): 587–599.

Weinert, H H 1980. *The natural road construction materials of Southern Africa*. Cape Town: H&R Academica, pp 52–54, 239–242.

Zhang, L.L. Zhang, J. Zhang, L.M. and Tang, W.H. 2010. *Stability analysis of rainfall-induced slope failure: a review*. Geotechnical Engineering 164(5)

7 APPENDIX A

7.1.1 Test A1: Moisture Content at 11.4%

The first test was conducted at the optimum moisture content determined from a Mod. AASHTO compaction tests. This centrifuge test was used as an initial assessment of the stability of the material being used, as well as to test the loading methodology with the loading block and pneumatic piston. The front view of the embankment through the strongbox window can be seen in Figure 7.1 and the top view in Figure 7.2. Disturbance of the top of the embankment model as a result of the placement of the model in the strongbox can be seen on the right of Figure 7.2. This was due to the compaction process outside the strongbox and the model had to be placed in the stronbox using the cable system and forklift.

Figure 7.1: Test A1- Front view of embankment model

Figure 7.2: Test A1 - Top view of embankment model.

The compaction for this first test was done in the separate wooden box. At this stage the wooden box did not have reinforcing installed to prevent bulging of the model during compaction. As a result of minor differences in dimensions of the separate compaction box and the strongbox as well the bulging that resulted from the compaction in the wooden strongbox, the embankment model did not have a tight fit in the strongbox. This resulted in a piece of the embankment that broke off during the test due to the spaces between the model and the strongbox shown in Figure 7.3.

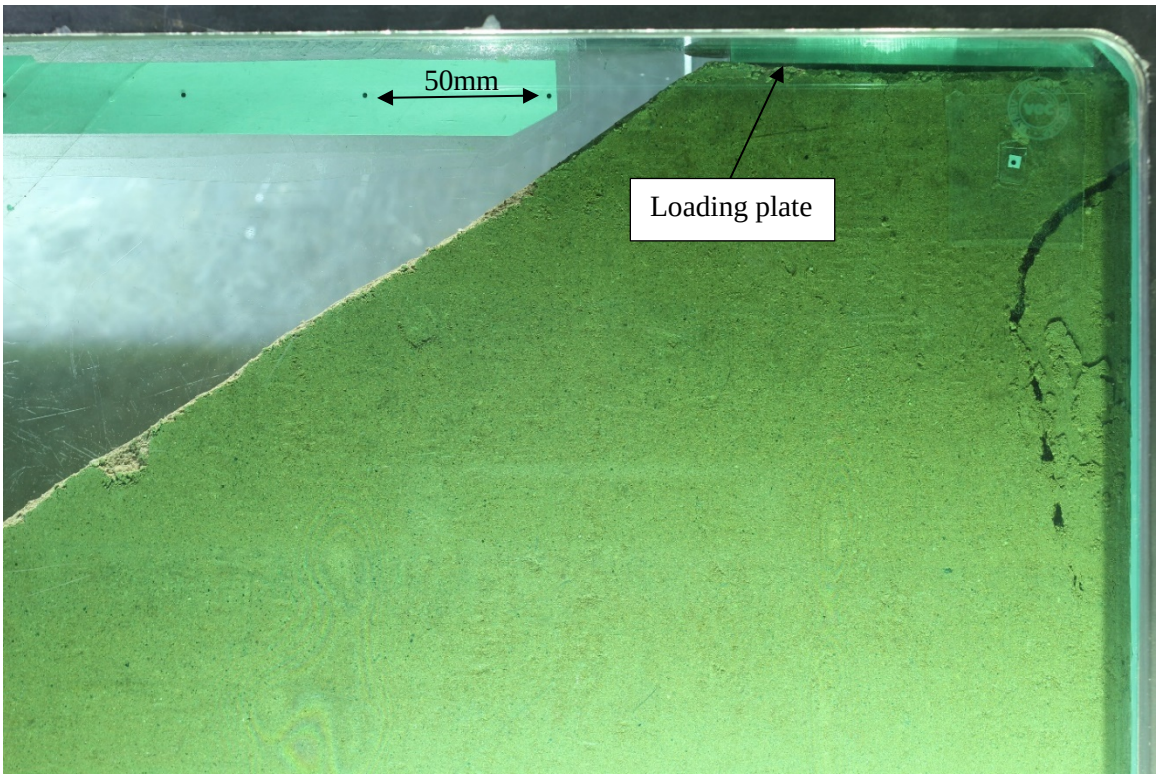

Figure 7.3: Broken wedge at the side of the embankment due to differences in dimensions of the compaction box and strongbox

The test was continued using the cyclic loading methodology. The stabilisation period was not yet used in this test and the loading was applied shortly after the centrifuge reached 50g acceleration. The test continued for approximately 1 hour and 45 minutes. Towards the end of the test when the rate of settlement decreased, a continuous supply of water was added to the top of the embankment as an attempt to induce an embankment failure. The flow of water was high and resulted in eroding the sides of the embankment running down and accumulating at the bottom of the embankment at the toe. The result of this erosion and accumulation of water can be seen in Figure 7.4. Due to the addition of water to the test and the variable flow down the side of the embankment, no moisture samples were taken at the end of the test.

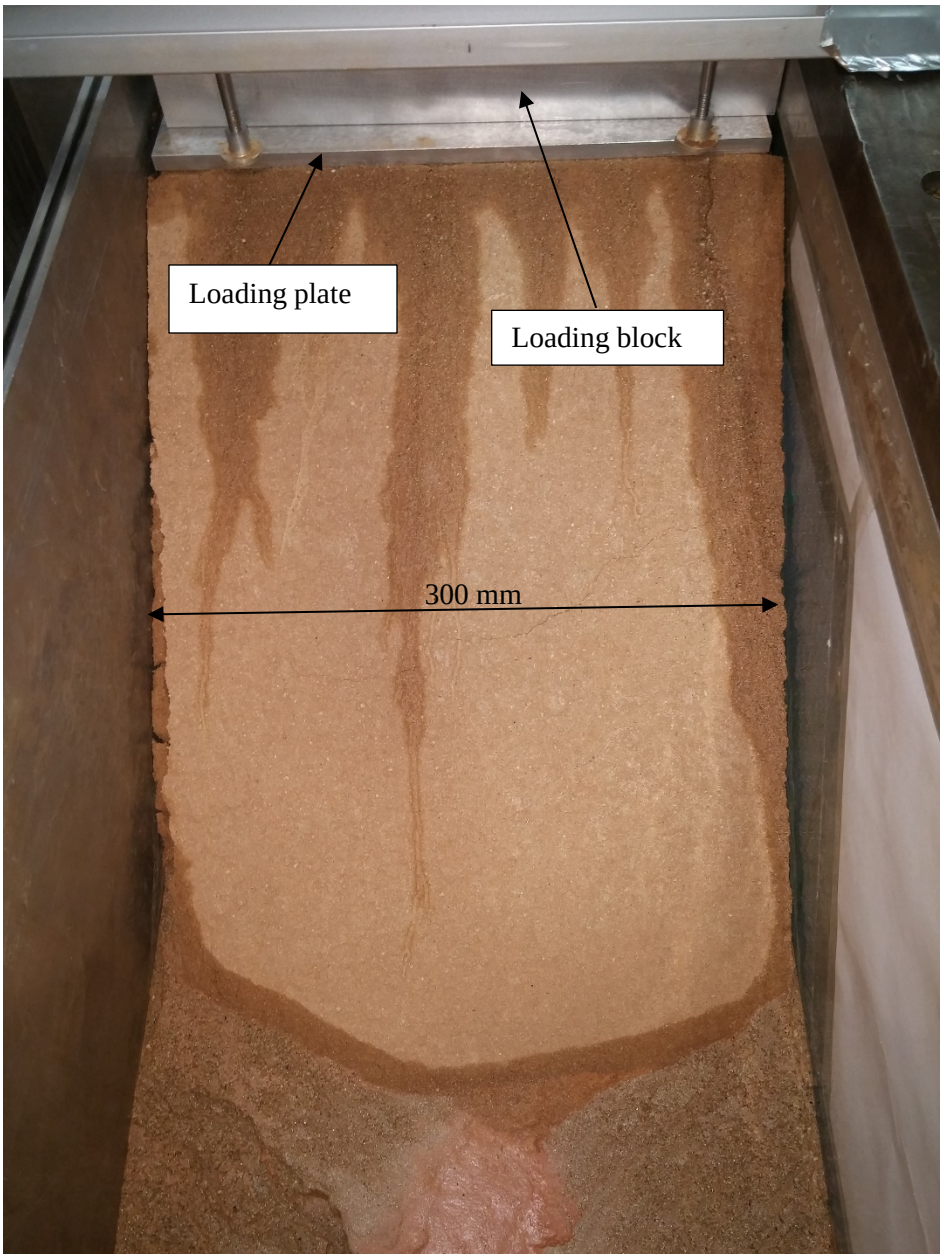

Figure 7.4: Erosion and water accumulation result from the addition of water to Test A1 (11.4% MC)

The recorded LVDT data from the different LVDTs were averaged to obtain the average settlement of the embankment model for the duration of the test. The result can be seen in Figure 7.5. On the figure it is indicated where the centrifuge is accelerating up to 50 g acceleration as well as the points where the loading is started, water is added and the end of the test. The settlement due to loading and the accompanying power function are shown in Figure 7.6.

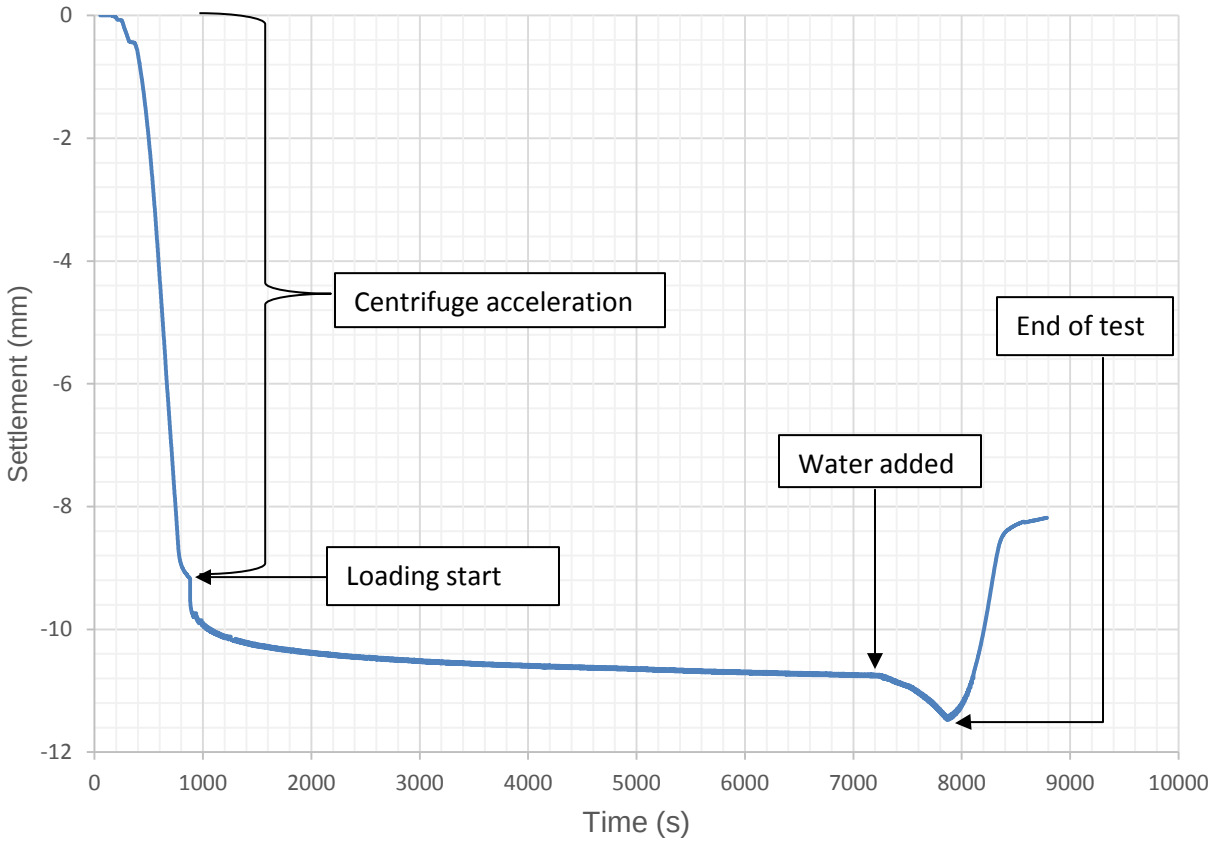

Figure 7.5: Settlement data for Test A1 (11.4% MC)

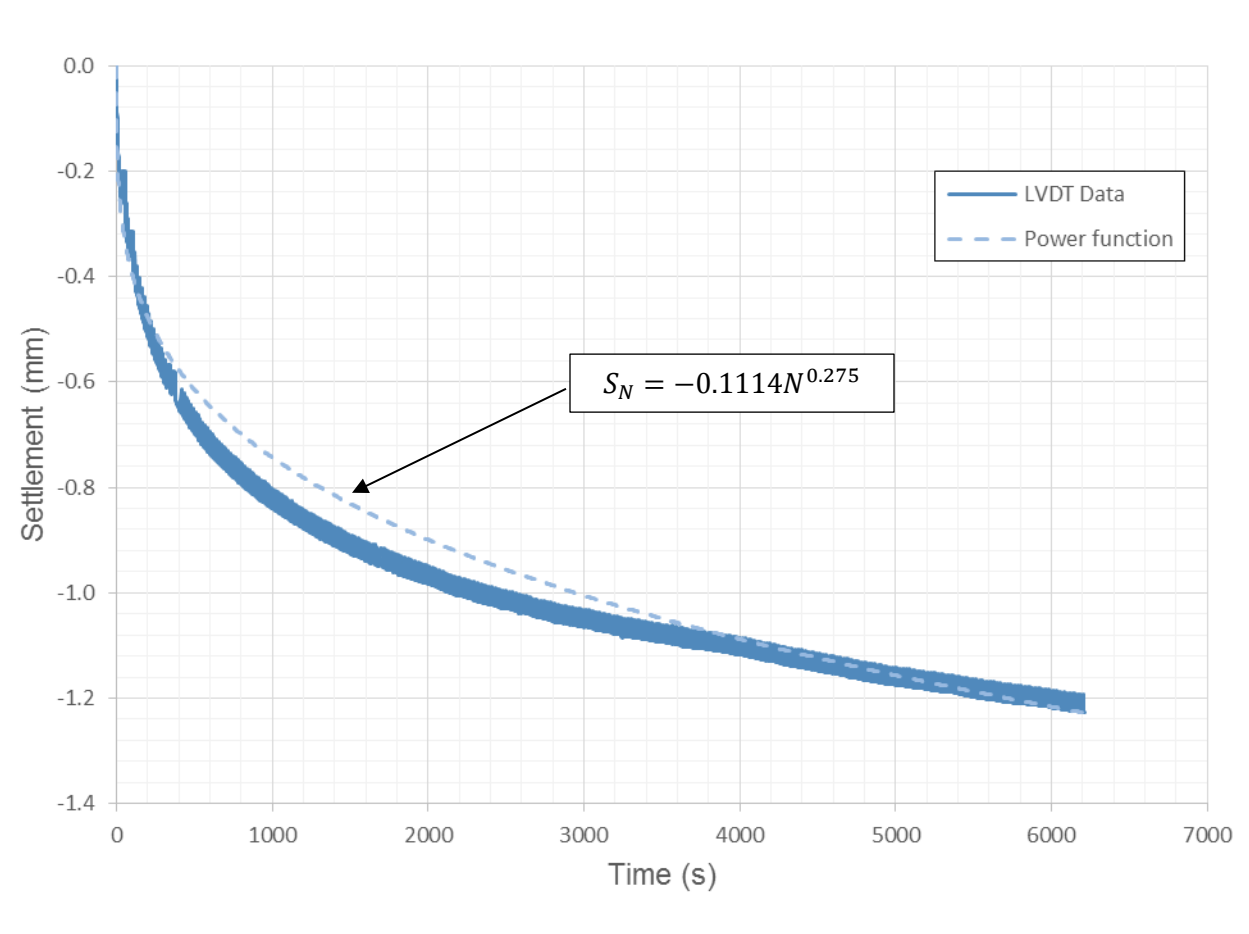

Figure 7.6: Loading settlement for Test A1 (11.4% MC)

7.1.2 Test A2: Moisture content at 20.0%

The second test involved a combination of a stabilisation period of an hour, static loading of three hours and cyclic loading of twelve hours. The model was compacted and constructed outside the strongbox in the separate wooden box which was reinforced to prevent bulging. The front of the embankment model can be seen in Figure 7.7. The model showed no signs of cracking or failure on the front of the embankment. The initial and final photos of the embankment can be seen in Figure 7.8 and Figure 7.9.

Figure 7.7: Test A2 (20.0% MC - Front of embankment model.

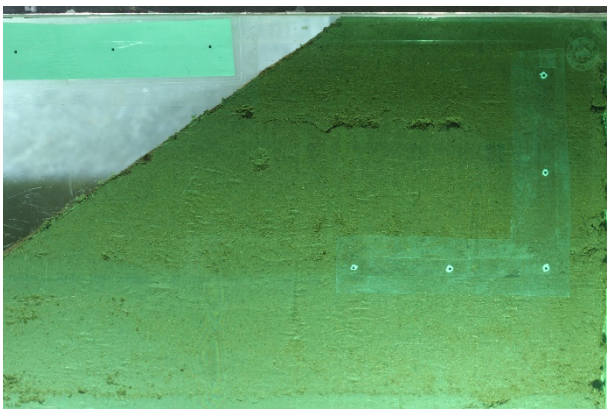

Figure 7.8: Photo at the start of Test A2 (20.0 % MC)

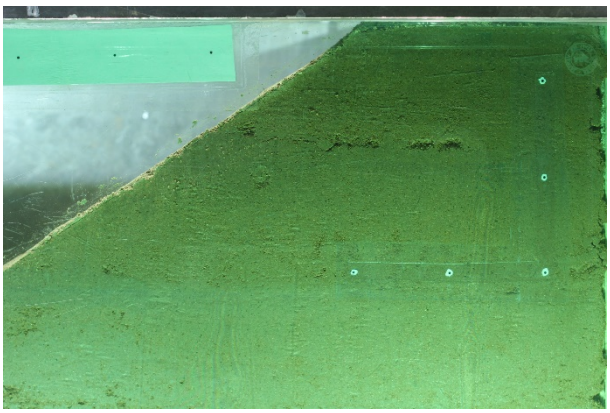

Figure 7.9: Photo at the end of Test A2 (20.0% MC)

The loading methodology at this stage was to conduct the static and cyclic loading on the same sample. The duration of the test was long and the test had to be stopped twice due to power outages. The LDVT data was reworked to remove the stopping and acceleration movements of the centrifuge. The reworked LDVT data can be seen in Figure 7.10.

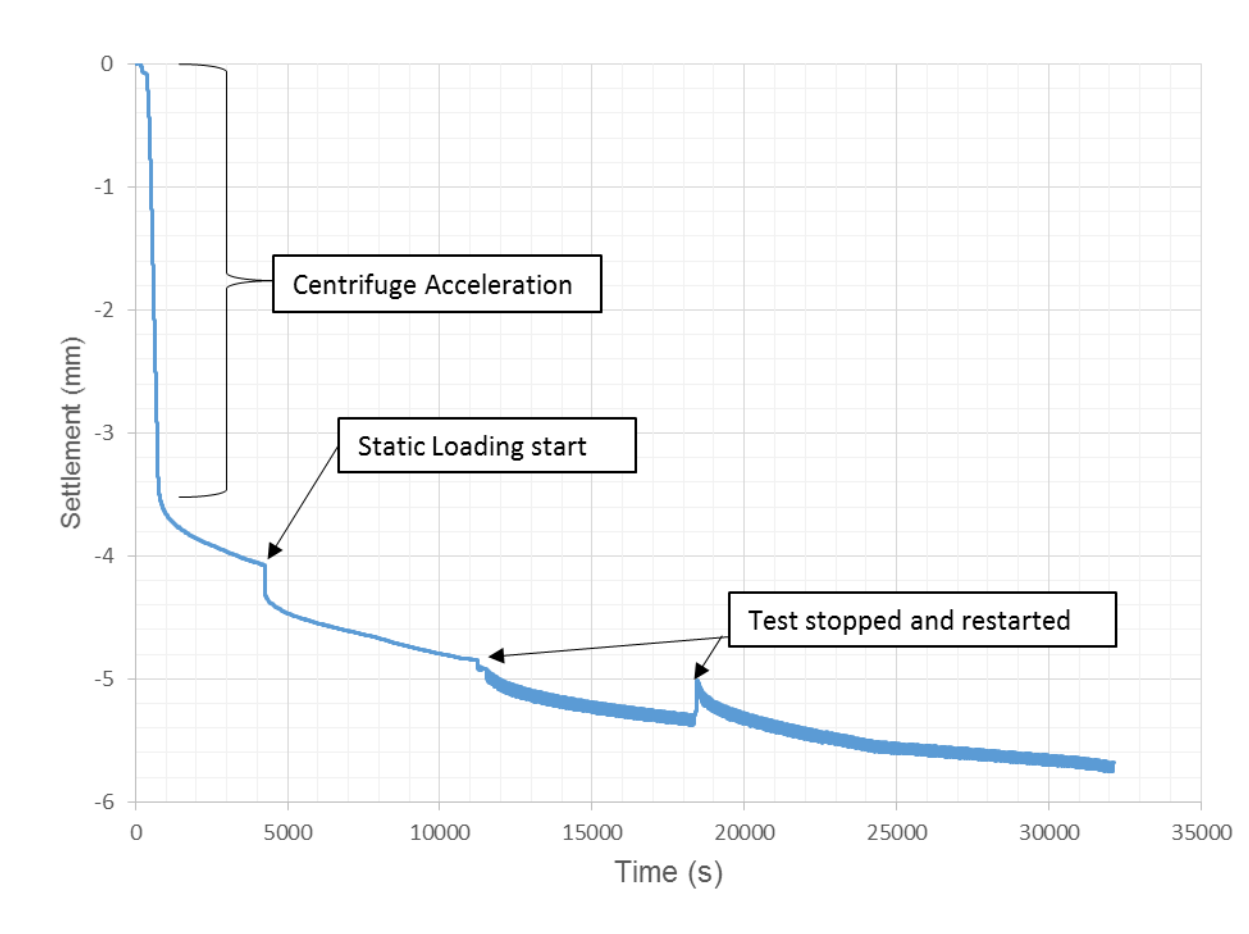

Figure 7.10: Settlement data for Test A2 (20.0 % MC)

The power function fitted to the adjacent settlement curve are shown in Figure 7.11. The results for the cyclic loading section of the test was not included as the results is affected by the static loading section of the test. For that reason the loading methodology was changed to what was discussed in Section 3.5.

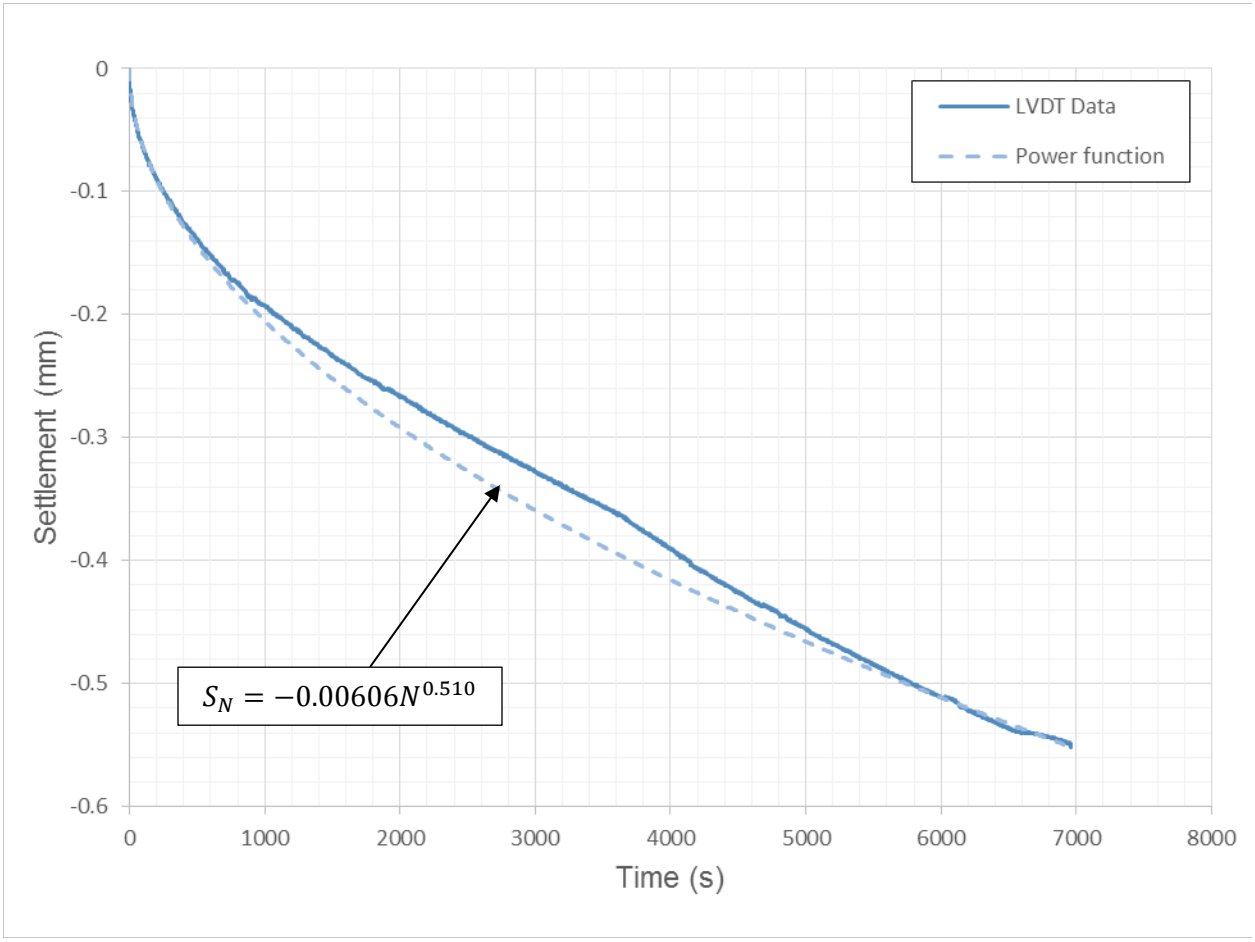

Figure 7.11: Settlement due to static loading for Test A2 (20.0 % MC)

7.1.3 Test A3: Moisture content at 28.0%

The third test was done at 28% moisture content to set an upper limit for the iterative process of the testing to find the turning point between a stable and unstable embankment. The compaction process was difficult with the high moisture content value and a 90% Modified AASHTO density could not be obtained. The dry density obtained was 87% Modified AASHTO.

During the acceleration of the centrifuge, the embankment collapsed under its own weight. A sequence of photos together with a PIV analysis showing the movement of the soil particles can be seen in Figure 7.12. Once a large amount of movement took place, the PIV analysis produced numerous wild vectors at the top of the embankment which had to be removed. This is visible on the third PIV image in Figure 7.12

and is carried through to the last PIV image. The grid used for the PIV analysis is also shown in Figure 7.12

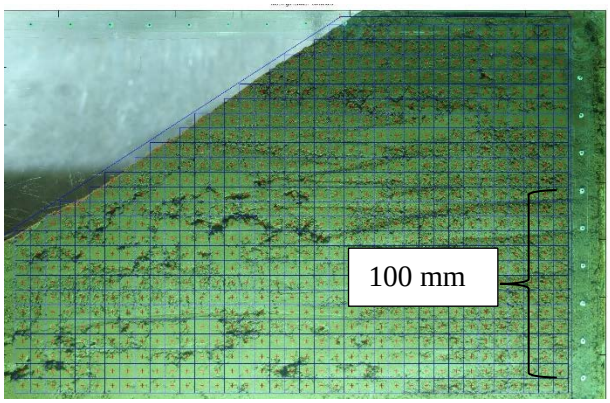

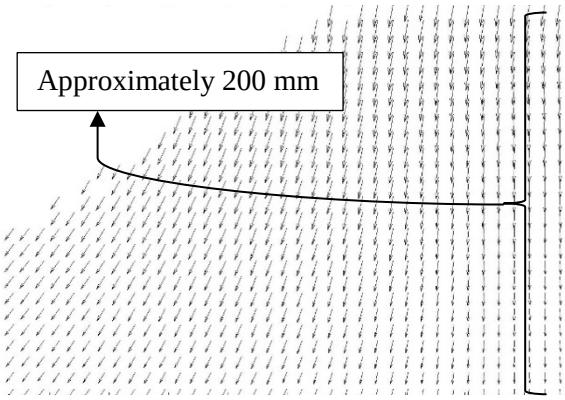

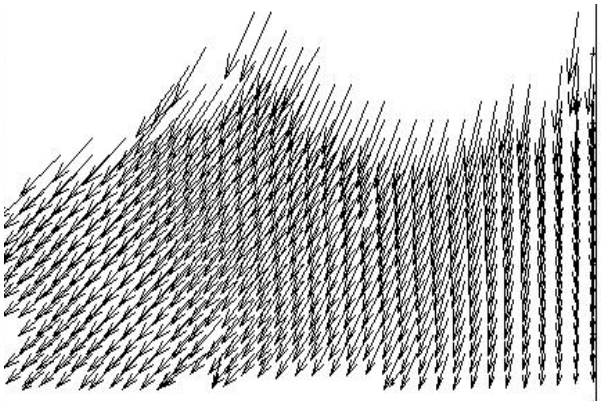

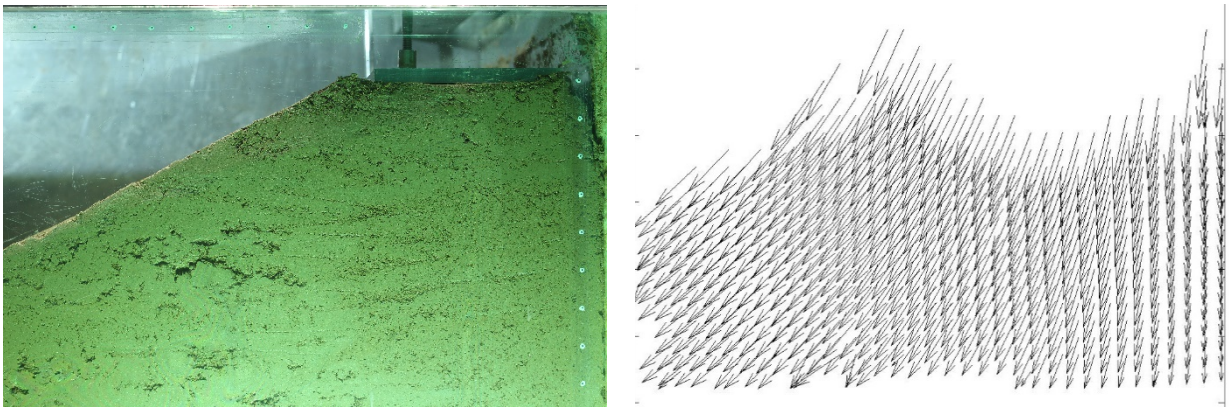

Figure 7.12: Sequence of images showing embankment collapse together with PIV results for Test A3 (28.0 % MC)

The PIV results produced a line trajectory of the particle movement through the collapse which can be seen in Figure 7.13. Once again the particles from the top of the embankment are missing due to the wild vectors which had to be removed.

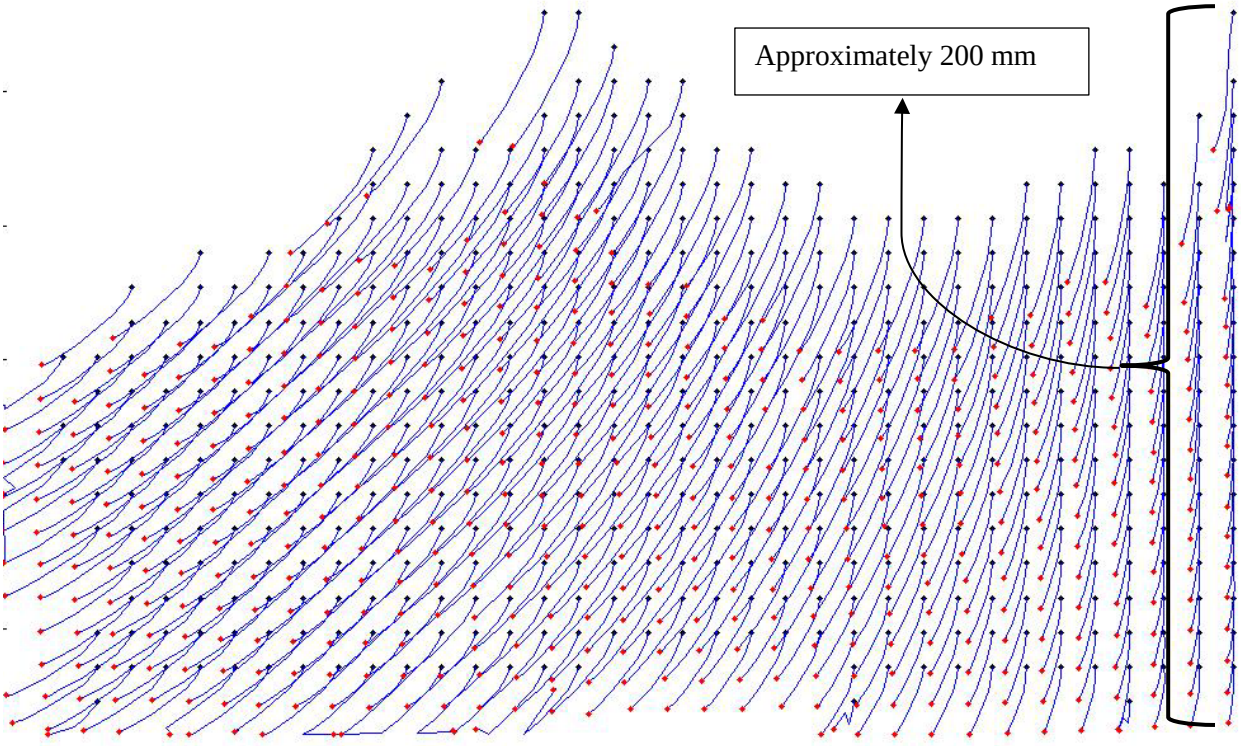

Figure 7.13: Line trajectory of particle movement for Test A3 (28.0 % MC)

The visual analysis after the test showed major bulging at the toe of the embankment. This can be seen in Figure 7.14.A significant crack formed at the top of the embankment which indicates a shearing failure occurring in the embankment, shown in Figure 7.15. The LVDT results showed large settlement during the acceleration of the centrifuge as shown in Figure 7.16.

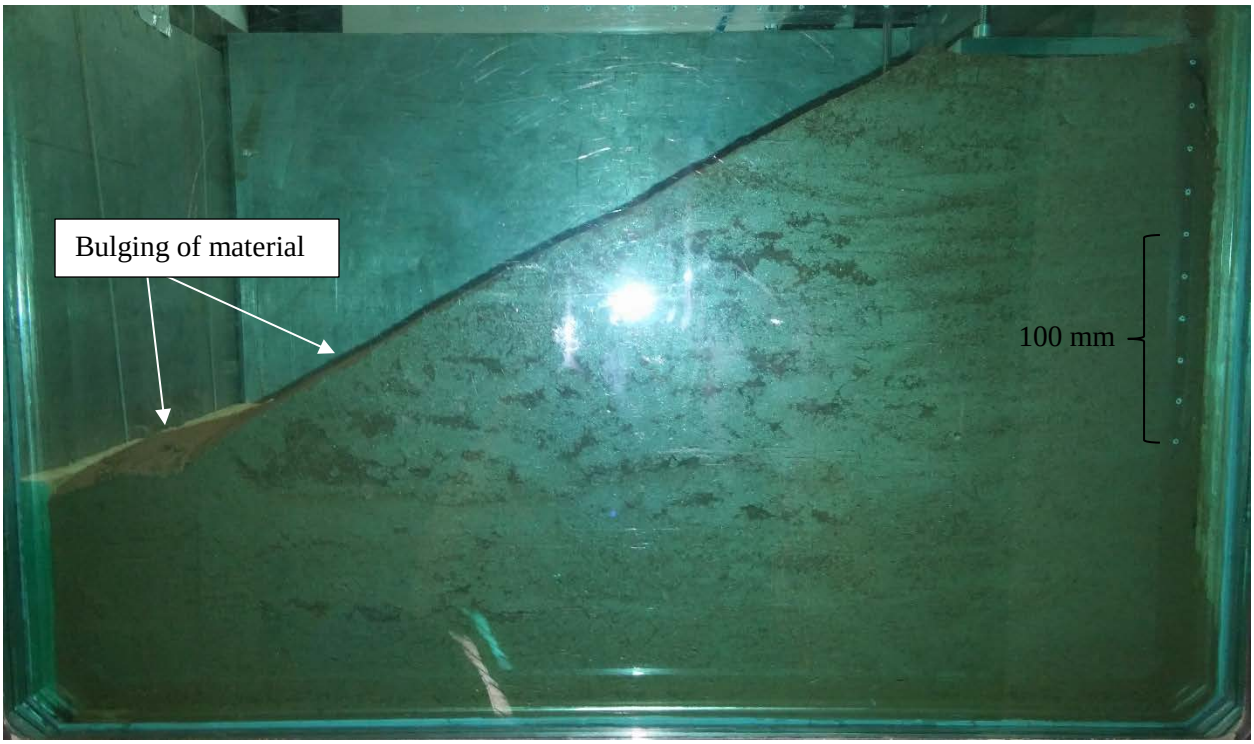

Figure 7.14: Visible bulging at the toe of the embankment for Test A3 (28.0 % MC)

Figure 7.15: Cracks that formed at the top of the embankment for Test A3 (28.0 % MC)

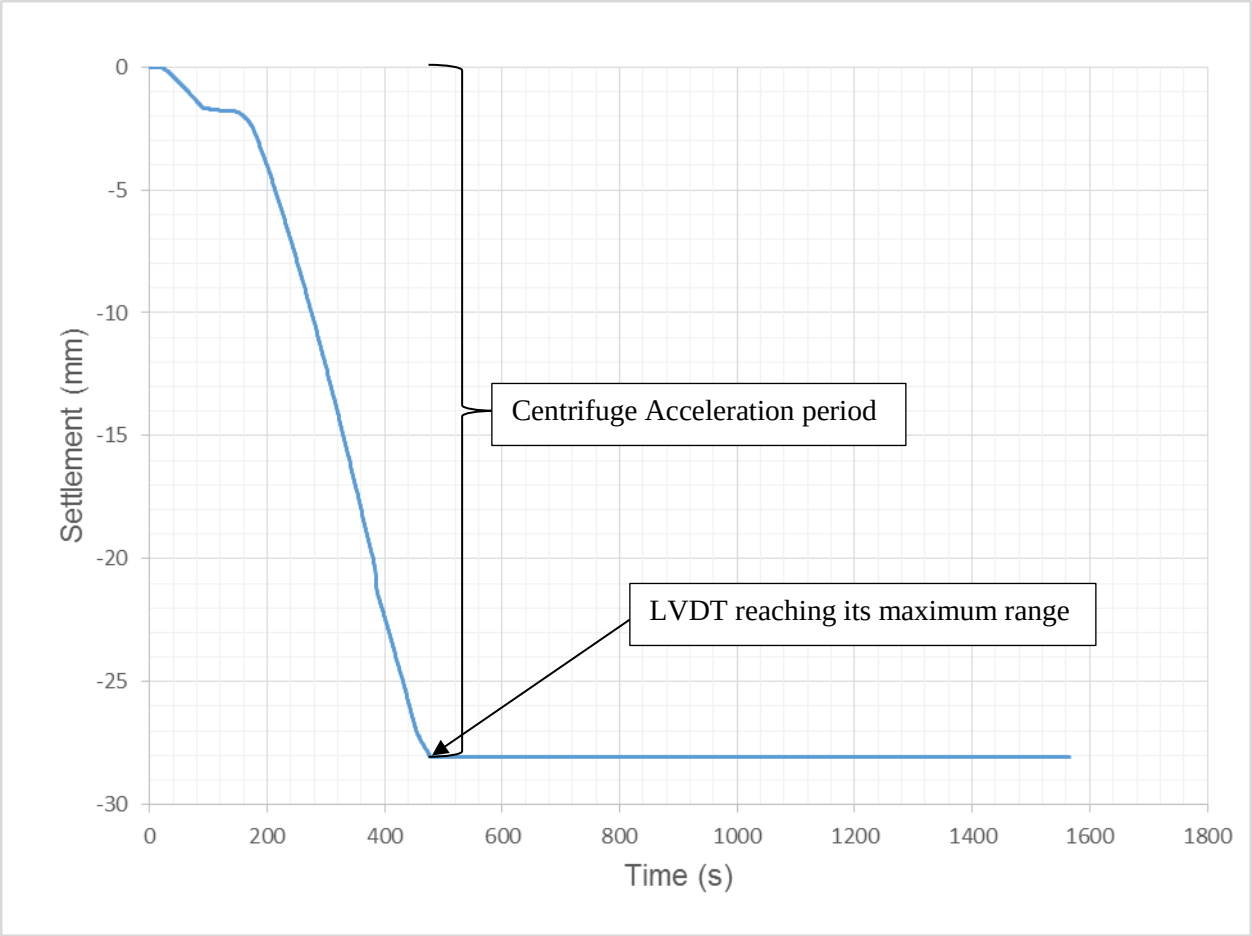

Figure 7.16: Settlement data for Test A3 (28% MC)

7.1.4 Test A4: Moisture content at 24.0%

The test at 24% moisture content performed very similar to the test at 28% moisture content. The embankment collapsed under its own weight during the acceleration of the centrifuge to 50 g. The sequence of the collapse together with the PIV results showing the particle vector movement is shown in Figure 7.17.

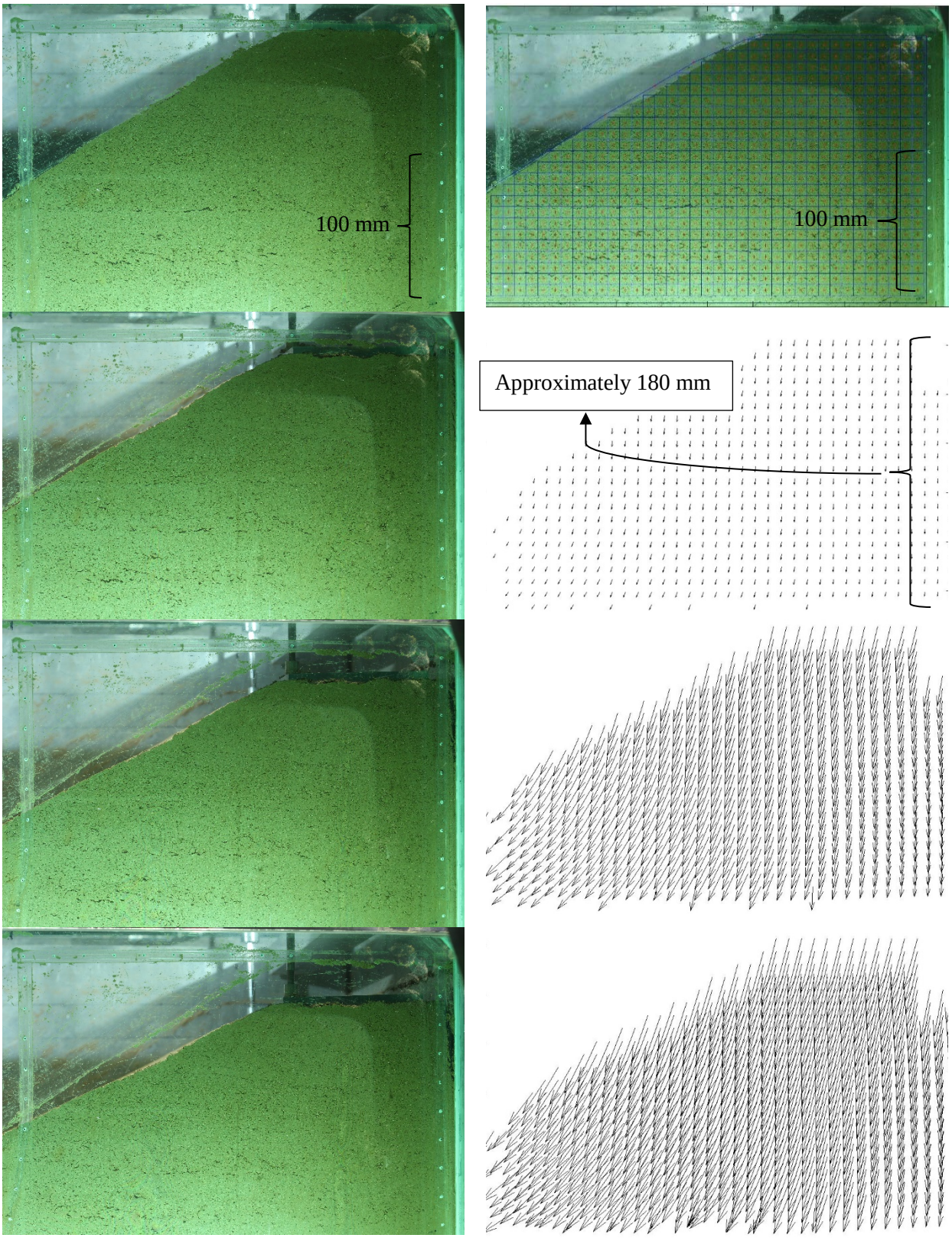

Figure 7.17: Sequence of images showing embankment collapse together with PIV results for Test A4

Figure 7.18 and Figure 7.19 show the front of the embankment before and after the test. The comparison of the photos shows the bulging at the toe of the embankment and the large amount of settlement that took place at the top of the embankment. No cracks formed during the test.

Figure 7.18: View of the front of the embankment before Test A4

Figure 7.19: View of the front of the embankment after Test A4

The settlement data for Test A4 is shown in Figure 7.20. One of the LVDTs reached its maximum range by the time the centrifuge reached 50 g acceleration. The test carried on to observe the continued settlement of the embankment up until the other LVDT reached its maximum range as well.

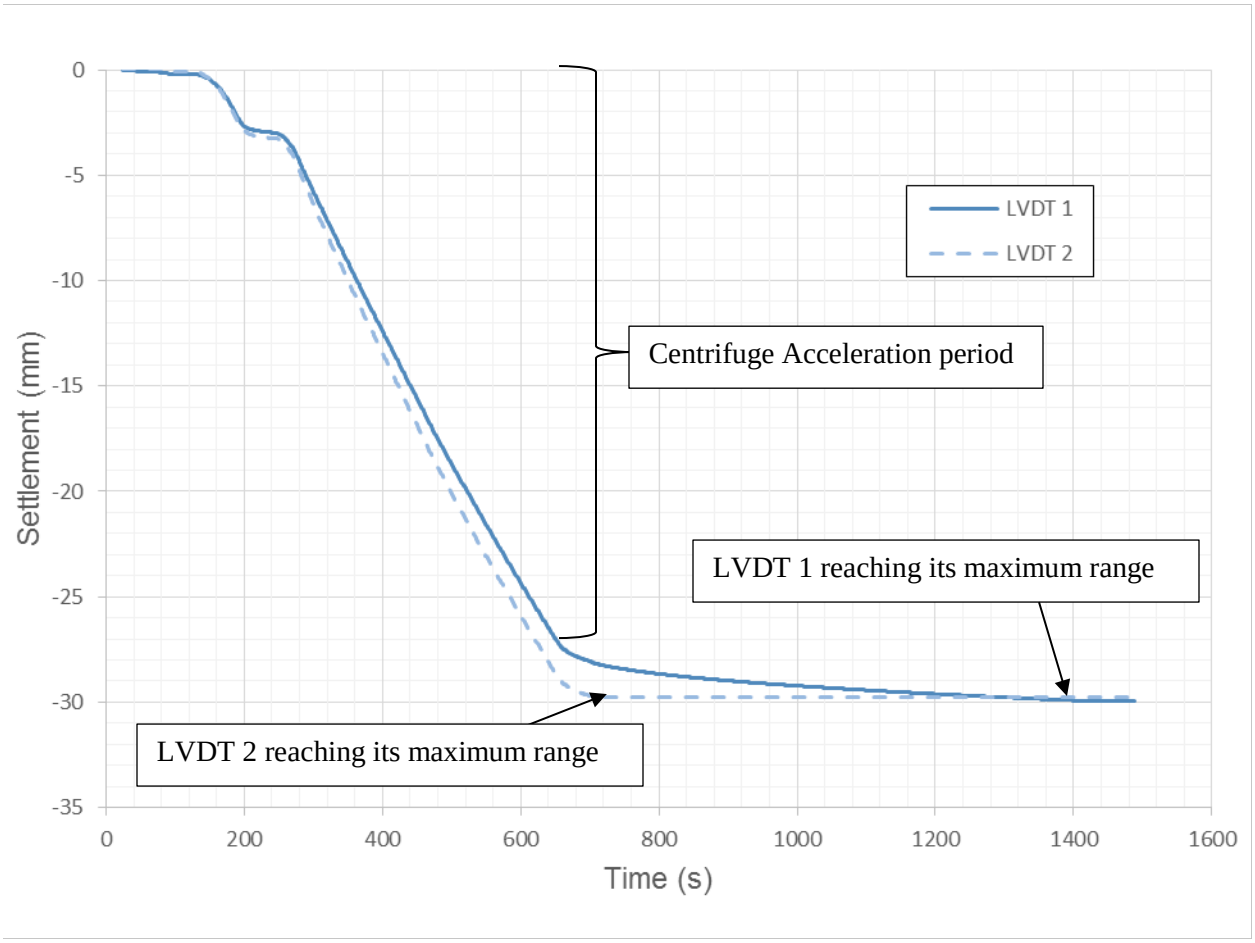

Figure 7.20: Settlement data for Test A4 (24.0 % MC)